

Electronic Thesis and Dissertation Repository

5-24-2017 12:00 AM

Thermal Kinetics of Helium Irradiation Hardening in Selected Alloys for the Canadian Gen. IV Nuclear Reactor Concept

Feifei Nie, *The University of Western Ontario*

Supervisor: Robert. J. Klassen, *The University of Western Ontario*

A thesis submitted in partial fulfillment of the requirements for the Master of Engineering Science degree in Mechanical and Materials Engineering

© Feifei Nie 2017

Follow this and additional works at: <https://ir.lib.uwo.ca/etd>



Part of the [Materials Science and Engineering Commons](#), [Nuclear Engineering Commons](#), and the [Operations Research, Systems Engineering and Industrial Engineering Commons](#)

Recommended Citation

Nie, Feifei, "Thermal Kinetics of Helium Irradiation Hardening in Selected Alloys for the Canadian Gen. IV Nuclear Reactor Concept" (2017). *Electronic Thesis and Dissertation Repository*. 4579.
<https://ir.lib.uwo.ca/etd/4579>

This Dissertation/Thesis is brought to you for free and open access by Scholarship@Western. It has been accepted for inclusion in Electronic Thesis and Dissertation Repository by an authorized administrator of Scholarship@Western. For more information, please contact wlsadmin@uwo.ca.

Abstract

In this thesis, we present nano-indentation measurements performed to quantify the increase in hardness as a result of He^+ and Fe^{4+} implantation in both Inconel 800H and AISI 310 alloys. After annealing, the softening rate of He^+ and Fe^{4+} implanted samples were compared, and it is found that Ni can slow the helium diffusion. Thermal activation energy Q characterizing this process was similar to the computed thermal activation energy Q_{He} for interstitial helium diffusion within pure nickel. Indentation hardness tests were also performed at various indentation strain rates, to further study the effect of implanted helium as an obstacle to plastic deformation. It was observed, for both AISI 310 and Inconel 800H, the strain rate sensitivity m decreases, and the activation volume V^* increases significantly after annealing. This suggests that helium defects (voids or bubbles) within the metal become more stable with annealing, as they tend to form bigger bubbles in the grain boundaries.

Keywords

Super-Critical Water Reactor (SCWR), helium implantation, ion irradiation, thermal recovery, nano-indentation, strain rate sensitivity

Acknowledgments

I could not have written this thesis without the invaluable insight, wisdom, guidance, and hard work of several people.

First and foremost, I'd like to thank, Professor Robert J. Klassen who give me the opportunity to do this research in graduate study at Western University. I also appreciate for his continuous guidance, advice, mentorship and confidence in me.

Besides, I'd like to thank Dr. Ariful Islam for his assistance in designing and running experiments. I sincerely thank my colleague Maisaa Nezar Tawfwwq and Aria Khalili for helping me study about the knowledge about the thesis and teaching me how to use the machine.

I'd like to thank NSERC for their financial support, and most importantly the opportunity to investigate the irradiation damage of the component material in CANDU reactor.

Table of Contents

Abstract.....	i
Acknowledgments.....	ii
Table of Contents.....	iii
List of Tables.....	vi
List of Figures.....	vii
List of Appendices.....	xii
List of Abbreviations.....	xiii
Chapter 1.....	1
1 Introduction.....	1
1.1 Background.....	1
1.2 Objective.....	3
1.3 Structure of thesis.....	3
Chapter 2.....	4
2 Review of relevant literature.....	4
2.1 The Canadian Gen. IV SCWR Concept.....	4
2.2 Neutron interactions in Ni-bearing alloys.....	9
2.3 The effect of neutron and ion irradiation.....	11
2.4 The effect of helium accumulation.....	13

2.5	Solid-state atomic diffusion	18
2.5.1	Mechanisms of diffusion.....	18
2.5.2	Role of diffusion in the deformation recovery process.....	20
2.6	Strain rate sensitivity of indentation hardness.....	21
2.7	Summary	23
3	Experimental procedure	24
3.1	Sample preparation.....	24
3.2	Ion implantation	26
3.3	Thermal annealing.....	30
3.4	Nano indentation tests	31
3.5	Strain rate sensitivity of the indentation hardness.....	33
Chapter 4	35
4	Experimental Results	35
4.1	Indentation hardness of He ⁺ and Fe ⁴⁺ implanted samples.....	35
4.2	Indentation hardness after annealing.....	36
4.3	The effect of helium atoms on strain rate sensitivity	41
Chapter 5	45
5	Discussion.....	45
5.1	Effect of implanted He ⁺ and Fe ⁴⁺ ions on the hardness	45
5.1.1	Effect of ion damage on the He ⁺ implanted samples.....	47

5.2	High temperature softening of ion implanted alloys	50
5.3	Strain rate sensitivity of the indentation hardness.....	58
5.4	Testing issues and their effects.....	63
Chapter 6	65
6	Conclusion, Contribution and Future Works	65
6.1	Conclusion and Contribution	65
6.2	Future Work	67
Reference	68
Appendix A	74
Appendix B	75
Curriculum Vitae	77

List of Tables

Table 2.1 Preliminary specifications for the Canadian Concept Gen. IV SCWR [10].....	6
Table 2.2 Implantation conditions and measured mechanical properties[28]	15
Table 3.1 Chemical composition, in weight percent, of AISI310 and Inconel 800H [42], [43] ..	25
Table 3.2 The experiment procedure in this thesis	31
Table 4.1 The strain rate sensitivity m of the indentation hardness of the AISI310 and Inconel 800H samples subjected to various implanted helium levels with no subsequent annealing	44
Table 4.2 The strain rate sensitivity m of the indentation hardness of the AISI310 and Inconel 800H samples subjected to various implanted helium levels and subsequent 10 minute annealing at 400°C.....	44
Table 5.1 Activation energy of the thermal recovery of indentation hardness in the AISI 310 and Inconel 800H alloys implanted with various levels of helium	58
Table 5.2 Measured activation energies for the thermal recovery of indentation hardness (from Table 5.1) listed along with calculated activation energies for the interstitial diffusion of helium within crystalline nickel.....	58
Table 5.3 The m and V^* and of Inconel 800H	59
Table 5.4 the m and V^* of AISI 310.....	61
Table 5.5 Comparison of this work to the research before.....	63

List of Figures

Figure 2.1 The overall layout of the core of the Canadian Concept Gen. IV SCWR[9] 5

Figure 2.2 Cross section and cutaway diagrams of a fuel channel in the Canadian Concept Gen. IV SCWR core 6

Figure 2.3 Temperature-pressure conditions for the coolant of the Canadian Concept Gen. IV SCWR (CANDU SCWR) in comparison to the coolant conditions of other existing nuclear reactors; namely, the light water moderated pressurized water reactor (PWR), the light water moderated boiling water reactor (BWR), and the pressurized heavy water moderated reactor (CANDU PHWR) [2], [12]..... 7

Figure 2.4 The concept of super-critical water-cooled reactor[13] 7

Figure 2.5 Calculated increase in neutron-induced atom displacements, in units of Displacements Per Atom (DPA), as a function of time, in units of Effective Full Power Years (EFPY), for an Inconel X750 alloy located in a CANDU nuclear reactor [6] 10

Figure 2.6 Calculated increase in accumulated hydrogen and helium, in units of Accumulated Parts Per Million (APPM), as a function of time, in units of Effective Full Power Years (EFPY), for an Inconel X750 alloy located in a CANDU nuclear reactor [6] 10

Figure 2.7 Irradiation effects on crystal structure. a) Before irradiation: high energy particle moving towards a lattice of low energy atoms. b) At collision: high energy particle impacts and dislocates a lattice atom. c) Cascade collisions: the PKA collides with and dislocates another atom. The radiation particle continues moving into the lattice, transferring more of its energy to other atoms. d) After collision: lattice now has high concentration of stress concentrations, vacancies, interstitials, and may have substitutional defects and is in a higher energy state. e) the dislocations collected on close-packed planes leaving vacancy-type dislocation loops. f) the atoms collapsed to form interstitial-type and vacancy-type dislocation loops [21]..... 12

Figure 2.8 Transverse UTS and Total Elongation (TE) at 240°C versus fast neutron fluence ($E > 1$ MeV) for Erable I and II specimens irradiated in the OSIRIS test reactor [18].	13
Figure 2.9 TEM image showing He bubble configuration in 70 nm Cu/Nb multilayer film after ~7 at.% He ion implantation at ~500 nm below [27].	14
Figure 2.10 TEM micrograph in the under-focused condition (~500 nm) showing bubble alignment on grain boundaries and matrix–precipitate interface after irradiated at 300–330C to ~55 dpa and 18,000 appm He [4].	15
Figure 2.11 Comparison of percent hardening in SA Inconel 718 and SA 316LN stainless steel as a function of (a) displacement damage from 3500 keV Fe-irradiation and (b) helium concentration from 370 keV He-injection (360 keV for the 316LN).	17
Figure 2.12 Percent hardening at 150 nm contact depth, relative to the unirradiated material, for SA Inconel as a function of displacement damage from 3500 keV Fe-ions and 370 keV He-ions. Upper axis shows the associated helium concentration for the He-irradiation (SA Inconel 718).	18
Figure 2.13 Schematic illustration of an interstitial atom, similar to helium in nickel, overcoming the energy barrier necessary to move from low energy, stable location to another location. The energy barrier is referred to at the activation energy Q .	19
Figure 2.14 Schematic illustration of three mechanism for He diffusion without irradiation (a) interstitial migration, (b) vacancy mechanism, (c) dissociation mechanism	20
Figure 2.15 Recovery of the yield strength of single crystal zinc at 253 K and 283 K[37]	21
Figure 3.1 The microstructure of (a) AISI310 and (b) Inconel 800 H after annealing at 1000°C for 15 minutes.	25
Figure 3.2 Schematic illustration of the Tandetron ion accelerator located at Western University Ontario.	26
Figure 3.3 SRIM simulation of the penetration of 1200keV He^+ ions into AISI310 alloy (a) the simulated ion trajectories (b) the He ion range at around 2 μm depth	27

Figure 3.4 SRIM calculation of He ⁺ and Fe ⁴⁺ with multiple energies implanted into (a) Inconel 800H alloy (b) AISI 310 alloy	28
Figure 3.5 Figure 3.5 Schematic illustration of the regions of helium ion implantation : (a) top view (b) side view	28
Figure 3.6 Schematic illustration of typical regions of ion exposure for samples used in the experiment (a) AISI 310 (b) Inconel 800H.....	29
Figure 3.7 Schematic illustration of the annealing furnace	30
Figure 3.8 Schematic illustration of the NanoTest indentation hardness testing platform.	32
Figure 3.9 The indentation force versus depth.....	33
Figure 3.10 The indentation point on the surface of the sample.....	33
Figure 3.11 The indentation load versus indentation depth curves under $\epsilon = 0.05, 0.25, 0.5, 1 \text{ s}^{-1}$ on Inconel 800H with no annealing and no helium implantation.	34
Figure 4.1 Indentation hardness versus helium concentration for the AISI 310 and the Inconel 800H alloys.	35
Figure 4.2 Indentation hardness versus Fe ⁴⁺ induced irradiation damage for the AISI 310 and the Inconel 800H alloys.	36
Figure 4.3 Indentation hardness as a function of annealing time (400°C) for (a) AISI 310 samples and (b) Inconel 800H samples with different appm levels of implanted helium.....	37
Figure 4.4 Indentation hardness as a function of annealing time (600°C) for (a) AISI 310 samples and (b) Inconel 800H samples with different appm levels of implanted helium.....	38
Figure 4.5 Indentation hardness as a function of annealing time (400°C) for (a) AISI 310 samples and (b) Inconel 800H samples with different dpa levels of Fe ⁴⁺ implanted irradiation damage. .	39
Figure 4.6 Microstructure of the AISI 310 alloy after annealing at 600C for: (a) 0 min, (b) 10 min, and (c) 40 min.	40

Figure 4.7 Microstructure of the Inconel 800H alloy after annealing at 600C for: (a) 0 min, (b) 10 min, and (c) 40 min.....	41
Figure 4.8 The indentation hardness versus indentation strain rate ($P/P = 0.05, 0.25, 0.5, 1 s - 1$) on (a) AISI 310 and (b) Inconel 800H with no annealing and with different helium implantation content.....	42
Figure 4.9 The indentation hardness versus indentation strain rate ($P/P = 0.05, 0.25, 0.5, 1 s - 1$) on (a) AISI 310 and (b) Inconel 800H with 10 min annealing at 400°C with different helium implantation content.....	43
Figure 5.1 Comparison of percent hardening in Inconel 800H, AISI310, Inconel 718 and SA 316LN as a function of (a) helium concentration (b) Fe ⁴⁺ ion irradiation.....	47
Figure 5.2 Comparison of percent hardening relative to unirradiated material for (a) Inconel 800H and the (b) AISI310as a function of helium concentration and Fe ion irradiation.....	49
Figure 5.3 The change of hardness of Inconel 800H when exposed to different dpa levels of ion implantation damage. The dpa level of damage was achieved by Fe ⁴⁺ implantation (red triangles) and He ⁺ implantation (blue circles). The individual graphs show data for various dpa levels: (a) 2.7 dpa & 10000 appm (b) 0.8 dpa & 3160 appm (c) 0.2 dpa & 1000 appm (d) 0.08 dpa & 320 appm (e) 0.02 dpa & 100 appm.....	51
Figure 5.4 The change of hardness of AISI 310 when exposed to different dpa levels of ion implantation damage. The dpa level of damage was achieved by Fe ⁴⁺ implantation (red triangles) and He ⁺ implantation (blue circles). The individual graphs show data for various dpa levels: (a) 2.7 dpa & 10000 appm (b) 0.8 dpa & 3160 appm (c) 0.2 dpa & 1000 appm (d) 0.08 dpa & 320 appm (e) 0.02 dpa & 100 appm.....	52
Figure 5.5 comparison of the rate, d(ΔH)/dt, of the softening that occurs over the first 10 minutes exposure to 400°C of (a) Inconel 800H and (b) AISI 310	53
Figure 5.6 The change of indentation hardness with time, over a 10-minute period, at temperature of 400°C and 600°C for the (a) AISI 310 and the (b) Inconel 800H alloys.....	56

Figure 5.7 Activation energy Q describing the rate of softening as a function of the implanted helium concentration for the (a) AISI 310 and (b) Inconel 800H alloys	57
Figure 5.8 Comparison of the m and V^* of Inconel 800H before- and after- annealing at 400°C for 10 min.....	60
Figure 5.9 Comparison of the m and V^* of AISI 310 before- and after- annealing at 400°C for 10 min	62

List of Appendices

Appendix A.....	74
Appendix B.....	75

List of Abbreviations

CANDU	CANada Deuterium Uranium
SCWR	Super Critical Water coolant Reactor
PKA	Primary Knock-on Atom
EFPY	Effective Full Power Years
UTS	Ultimate Tensile Strength
dpa	Displacement per atom
appm	Atom part per million
$C_{(He)}$	Concentration of helium
$\rho_{(He)}$	Helium ion implantation induced displacement damage
Q	Thermal activation energy
\dot{P}	Loading rate
$\dot{\epsilon}$	Strain rate
H	hardness
σ_{ind}	Indentation stress
m	Strain rate sensitivity
V^*	Activation volume

Chapter 1

1 Introduction

1.1 Background

During the early 20th century significant discoveries were made in the field of nuclear physics and chemistry and this led to the development of technologies that allowed electrical energy to be generated from the nuclear fission of atoms. Canada became an important player in this technology by developing the CANDU reactor in the 1960s. This was the first large-scale commercial reactor to use heavy-water neutron moderation, thus allowing it to generate power from the fission of unenriched, natural, uranium.

There are nineteen CANDU reactors currently operating in the province of Ontario and they provide approximately 60% of Ontario's electrical generating capacity [1]. These CANDU reactors use a liquid heavy water (D_2O) coolant operating at a temperature of between $250^\circ C$ and $310^\circ C$ and a pressure of about 15 MPa. Their thermal efficiency is rather low, typically around 33%. There is thus an interest from the Canadian nuclear industry to move to a more thermally efficient nuclear reactor design that would involve the use of higher temperature, supercritical water cooling system ($T > 374^\circ C$ and $P > 22$ MPa). Such SuperCritical Water cooled Reactors (SCWRs) give a thermal efficiency of about 48% which is about one third higher than current CANDU reactors [2].

The increased coolant temperature of a SCWR requires the in-core use of a metal other than the currently used zirconium alloys. Nickel-bearing alloys are being considered for this application because of their excellent corrosion resistance in supercritical water and their superior, strength and creep resistance at temperature typical of that in the core of a SCWR. The primary liability of Ni-bearing alloys for use within a nuclear reactor is their high tendency to absorb (capture) neutrons ($\sigma_{cap_{Ni}} = 4.43b$ compared $\sigma_{cap_{Zr}} = 0.19b$ [3]). This results in decreased reactivity of the core and also very high levels of irradiation damage resulting from both direct neutron-atom displacement events and accumulation of helium and hydrogen as a result of α and β decay processes within the alloy. Helium accumulation is of particular concern since clear evidence exists showing its effect on promoting intergranular fracture and excessive

hardening/embrittlement of a wide variety of metals including Ni[4]–[8]. The elevated temperature of the Ni-bearing components within a SCWR may, however, reduce the tendency for He-induced embrittlement by providing increased thermal diffusivity to occur concurrent with neutron irradiation. To date, the effect of temperature and time on the He-induced hardening of candidate Ni-bearing alloys for the Canadian (Gen IV) SCWR has not been studied. This is the research topic of this thesis.

This thesis presents the results of a study of two Ni-bearing alloys, AISI 310 and Inconel 800H. We perform He^+ and Fe^{4+} implantation on samples of these alloys to simulate neutron induced hardening and He accumulation. Isothermal annealing tests were then performed on the ion-implanted samples to assess the effect of temperature and time on the recovery, and strain rate sensitivity, of the indentation hardness. By so doing, we deduce the characteristics of the rate controlling deformation mechanisms in these alloys. The hypotheses upon which this study is based are the following:

1. Self-similar heavy ion Fe^{4+} implantation within these Fe-base, but nickel bearing alloys will induce the same type of crystal damage as neutron irradiation.
2. Helium ion implantation will create the same distribution of helium within the test material as helium produced in-reactor by α -decay processes.
3. The evolution of crystal damage and He accumulation within a Ni-bearing alloy when in a SCWR core will be a function of the temperature, time, neutron flux, and neutron fluence. While these factors will be occurring concurrently, we will assume that their effect is independent of each other. Thus, we can study the effect of each factor separately.
4. We also assume that the factors mentioned above will result in microstructural changes that will affect the mechanical hardness of the Ni-bearing alloys in a way that can be detected by monitoring the strain rate sensitivity of the hardness.

1.2 Objective

The objectives of this study are

1. To assess the extent to which irradiation- and helium-induced hardening will accumulate in components made of these alloys in the Canadian Gen. IV SCWR core.
2. To study the effect of implanted He^+ and Fe^{4+} (self-similar) ions on the thermal stability and the strain rate sensitivity of the indentation hardness of these alloys when they are exposed to high temperature conditions.

1.3 Structure of thesis

This thesis has six chapters. Chapter 2 contains a review of the literature dealing with the key concepts relevant to this study. Chapter 3 describes the experimental procedures used in this study. Chapter 4 presents the results obtained from the experiments. Chapter 5 presents a discussion of the results, a comparison with other previously published research. Chapter 6 presents the conclusions of this study.

Chapter 2

2 Review of relevant literature

In this thesis, the effect of accumulated helium and temperature on the indentation hardness of two Ni-bearing candidate alloys for in-core use in the Canadian concept Gen. IV SCWR will be studied. This chapter presents a review of relevant published literature pertaining to this subject.

Section 2.1 provides a brief introduction of the layout and operation of the Canadian concept Gen. IV Super Critical Water Reactor core. Section 2.2 describes the neutron interaction mechanisms that are operative within in-reactor Ni-bearing alloys. Section 2.3 describes the effect of neutron and self-similar high-energy ion irradiation on the mechanical properties of metal alloys. Section 2.4 introduces the effect of helium accumulation on the Ni-containing material and compares their effect to that of accumulated self-similar ions. Section 2.5 reviews the mechanisms by which solid state diffusion and microstructural recovery occur in metals at elevated temperature. Section 2.6 reviews indentation-based micromechanical testing techniques that can be used to deduce the apparent activation volume associated with the deformation process within a metal. These techniques are used in the studies described in the subsequent chapters.

2.1 The Canadian Gen. IV SCWR Concept

A consortium of Canadian organizations, led by the Canadian Nuclear Laboratory (CNL) and Minister of Natural Resources Canada (NRCAN), has been working over the last five years to develop a viable concept for a heavy water moderated thermal neutron fission reactor that would incorporate use super critical water cooling to operate at significantly elevated core temperature and thus attain significantly higher thermal efficiency than current nuclear reactors [9]. The proposed Gen. IV SCWR core is shown in Figure 2.1. The four-meter diameter calandria vessel contains the liquid heavy water (D_2O) neutron moderator which surrounds three hundred vertical fuel channels. Each fuel channel contains a vertical string of annular fuel bundles surrounded by a thin metal liner and then a thicker ceramic (ZrO_2) insulator. This assembly is housed within a zirconium alloy pressure tube (Figure 2.2) The primary coolant in this reactor is light water (H_2O) which enters each pressure tube from the top, travels down via the central flow tube, reverses

direction at the bottom of the pressure tube and returns back up the pressure tube by flowing around the fuel bundles. The heat removed from the fissioning fuel will convert the pressurized coolant into a super critical state water. The supercritical coolant is then collected in the outlet plenum and directed to a turbine to produce electricity.

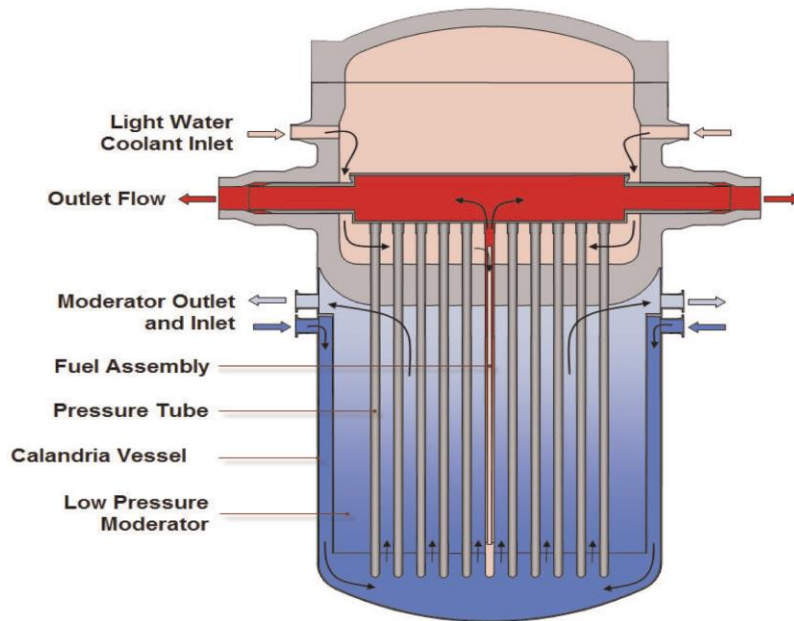


Figure 2.1 The overall layout of the core of the Canadian Concept Gen. IV SCWR[9]

Many of the components within the fuel channel of the Canadian Concept SCWR will be subjected to very high levels of neutron flux at elevated temperature, up to about 850°C, (Table 2.1). This is particularly the case for the: i) central coolant flow tube, ii) fuel cladding, and iii) inner metal liner located between the fuel bundles and the ceramic insulator (Figure 2.2).

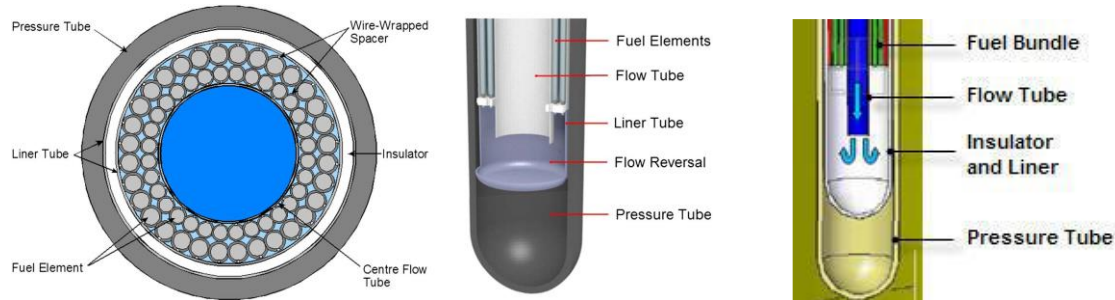


Figure 2.2 Cross section and cutaway diagrams of a fuel channel in the Canadian Concept Gen. IV SCWR core

Table 2.1 Preliminary specifications for the Canadian Concept Gen. IV SCWR [10]

Thermal Power (MW)	Electrical Power (MW)	Thermal Efficiency	H ₂ O Coolant Temperature (°C) and Pressure (MPa)		Maximum cladding temperature (°C)	Calandria Vessel Diameter (m)	Number of fuel channels	Fuel (enrichment)
			Inlet	Outlet				
2540	1220	48 %	350	625	850	4	300	UO ₂ /Th (4% ²³⁵ U)
			26	25				

When the pressure and temperature of water exceed 22.1 MPa and 374°C, the water enters the “supercritical” state where the distinction between liquid and gaseous phases vanishes (Figure 2.3) [11]. In this state, the water exists as small, liquid-like, hydrogen-bonded H₂O clusters dispersed within a gas-like, unclustered, H₂O phase. The physical properties of this supercritical water vary with temperature and pressure [12].

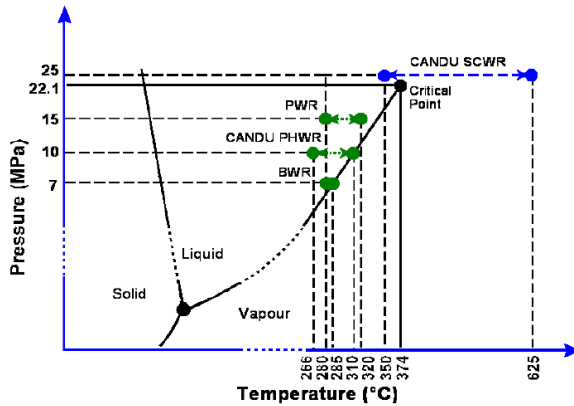


Figure 2.3 Temperature-pressure conditions for the coolant of the Canadian Concept Gen. IV SCWR (CANDU SCWR) in comparison to the coolant conditions of other existing nuclear reactors; namely, the light water moderated pressurized water reactor (PWR), the light water moderated boiling water reactor (BWR), and the pressurized heavy water moderated reactor (CANDU PHWR) [2], [12].

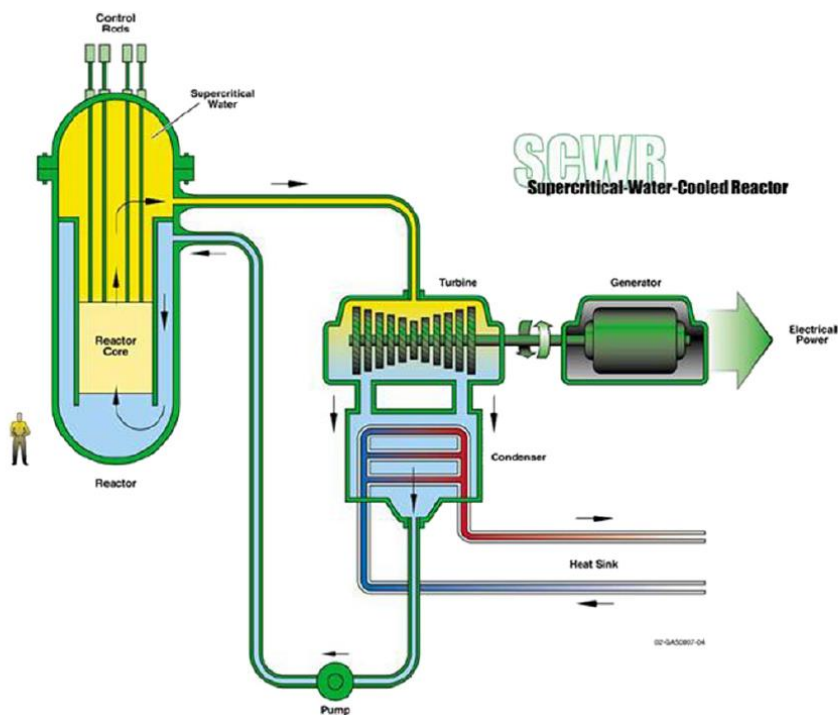


Figure 2.4 The concept of super-critical water-cooled reactor[13]

Supercritical water configuration allows significantly greater heat transfer per unit volume conventional lower temperature liquid or gaseous water state. Besides, the steam generators and/or steam dryers used in existing PWR and BWR reactors can be omitted since the supercritical coolant can be sent directly to the steam turbines (Figure 2.4) [14]. Therefore, this high temperature, supercritical, water cycle offers significantly improved electrical generation efficiency.

The conditions within the fuel channel of the Canadian concept Gen IV SCWR will be severe: the coolant temperature will range from 350°C to 625°C, with localized areas reaching up to 850°C and the coolant pressure will be above 22.1 MPa [6]. Supercritical water is significantly more corrosive than traditional light water coolant and this could present structural problems related to high general corrosion rates and localized stress corrosion cracking. In addition, high levels of neutron flux within the fuel channels could increase the likelihood of material swelling, creep, and embrittlement [13], [15].

The critical metal components in the reactor core are the liner tube and the fuel cladding since they are exposed to the highest temperature and neutron flux (Figure 2.2). The metal liner tube is designed to minimizing potential mechanical damage to the insulator by the fuel bundle assembly and provides a hard surface for the fuel bundles to slide and rest on [16]. It remains in the core throughout the reactor's lifetime (30-40 years). The fuel cladding around the fuel bundle is also exposed to high temperature and neutron flux, similar to the liner tube, but its residency time within the core is much shorter (less than 5 years) as it will be replaced during every refueling.

Two candidate alloys, Inconel 800H and AISI 310 (Table 3.1), have been suggested for the liner tube and fuel cladding [6], [7]. While the strength and creep resistance of these materials in their non-irradiated form is well studied and their service temperature extends up to 800° C [2], the effect of neutron irradiation and helium accumulation on the high temperature strength of these alloys is still largely unstudied and is the subject of this thesis.

2.2 Neutron interactions in Ni-bearing alloys

While both the Inconel 800H and AISI 310 alloys are iron -based alloys, nickel is their principal alloy addition. While these alloys have exceptionally good strength, creep resistance, and corrosion resistance at high temperature, up to about 800°C, their high concentration of Ni results in relatively high interactions with neutrons. Nickel has a very high thermal neutron absorption cross-section of 4.43b compared to 0.19b for zirconium [3]. This results in a high tendency for neutron collision induced microstructural changes occurring within these alloys. While in a typical nuclear reactor core, direct impacts with fast neutrons ($E > 1$ MeV) result in every ^{58}Ni atom being displaced from its equilibrium crystal lattice position about once per year (i.e. one displacement per atom (dpa) per year). Thus, approximately 25 dpas result from direct neutron- ^{58}Ni interactions and 35 dpas result from ^{59}Ni reaction over the course of a 25-year lifetime of a Ni-based alloy component (Figure 2.5). This movement of atoms results in tremendous nucleation of crystal defects, particularly vacancy and interstitial point defects and small dislocation loops (Section 2.3). In addition, slow moving “thermal” neutrons tend to become absorbed in the nucleus of ^{58}Ni atoms causing them to transmute to the unstable ^{59}Ni isotope. This isotope then decays by emitting a ^4He atom through an α -decay process [4]–[8]. The calculated amount of ^4He produced as a result of the decay of ^{59}Ni is close to 20000 ppm over the 25-year life time of a Ni-based alloy located in an existing CANDU reactor (Figure 2.6). The accumulation of He in a metal imparts hardening and embrittlement [17].

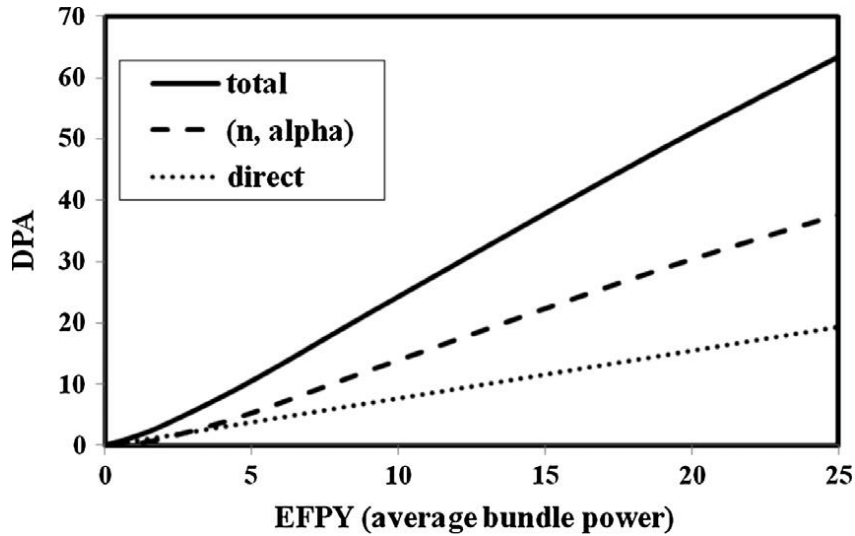


Figure 2.5 Calculated increase in neutron-induced atom displacements, in units of Displacements Per Atom (DPA), as a function of time, in units of Effective Full Power Years (EFPY), for an Inconel X750 alloy located in a CANDU nuclear reactor [6]

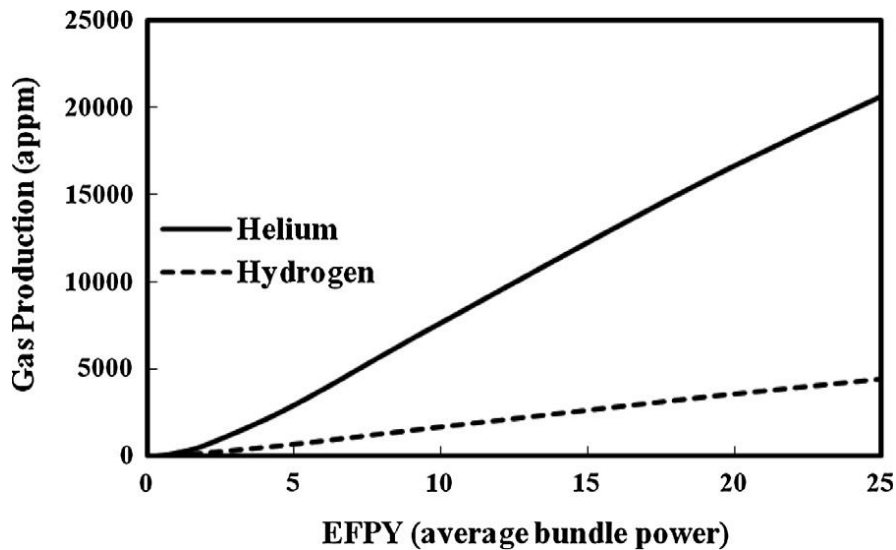


Figure 2.6 Calculated increase in accumulated hydrogen and helium, in units of Accumulated Parts Per Million (APPM), as a function of time, in units of Effective Full Power Years (EFPY), for an Inconel X750 alloy located in a CANDU nuclear reactor [6]

2.3 The effect of neutron and ion irradiation

The crystal damage resulting from exposure to high energy neutrons or high energy heavy ions is shown schematically in Figure 2.7. The atoms that are displaced from their equilibrium periodic locations with the crystal are referred to as primary knock-on atoms (PKA) and, in turn, often dislocate more atoms through secondary and tertiary collisions. For example [6], the minimum neutron energy needed to create a PKA is about 580 eV in Ni alloys. The resulting PKA Ni atom will have an average recoil energy about 40 eV and this energy is transfer to nearby Ni atoms. In practice, one collision of a high energy neutron or ion with a Ni atom can generate hundreds of displace atoms via secondary and tertiary collisions. While the vast majority of the displaced atoms fall back into equilibrium crystal positions, a significant number end up in non-equilibrium interstitial sites leaving behind vacancies within the crystal. Clustering of these collision-induced vacancies and interstitials result in the formation of vacancy and interstitial type dislocation loops which appear as small, less than about 10 nm diameter, dislocation loops throughout the irradiated material. These defects are very effective at impeding the movement of dislocations through the material and therefore increasing the hardness of the material.

Research has confirmed that the Ultimate Tensile Strength (UTS) of neutron irradiated Zr alloys in the OSIRIS test reactor shows a linear relationship with neutron flux, as shown in Figure 2.8[18]. The indentation hardness results in Chapter 4 of this thesis present similar trend of indentation hardness upon various ion fluences. Previous studies also show that the dislocation damage resulting from the ion bombardment, is similar in size and character with the crystal damage produced by neutron irradiation [19]. Therefore, in this study, we use He⁺ and Fe⁴⁺ implantation to simulate the effect of neutron irradiation.

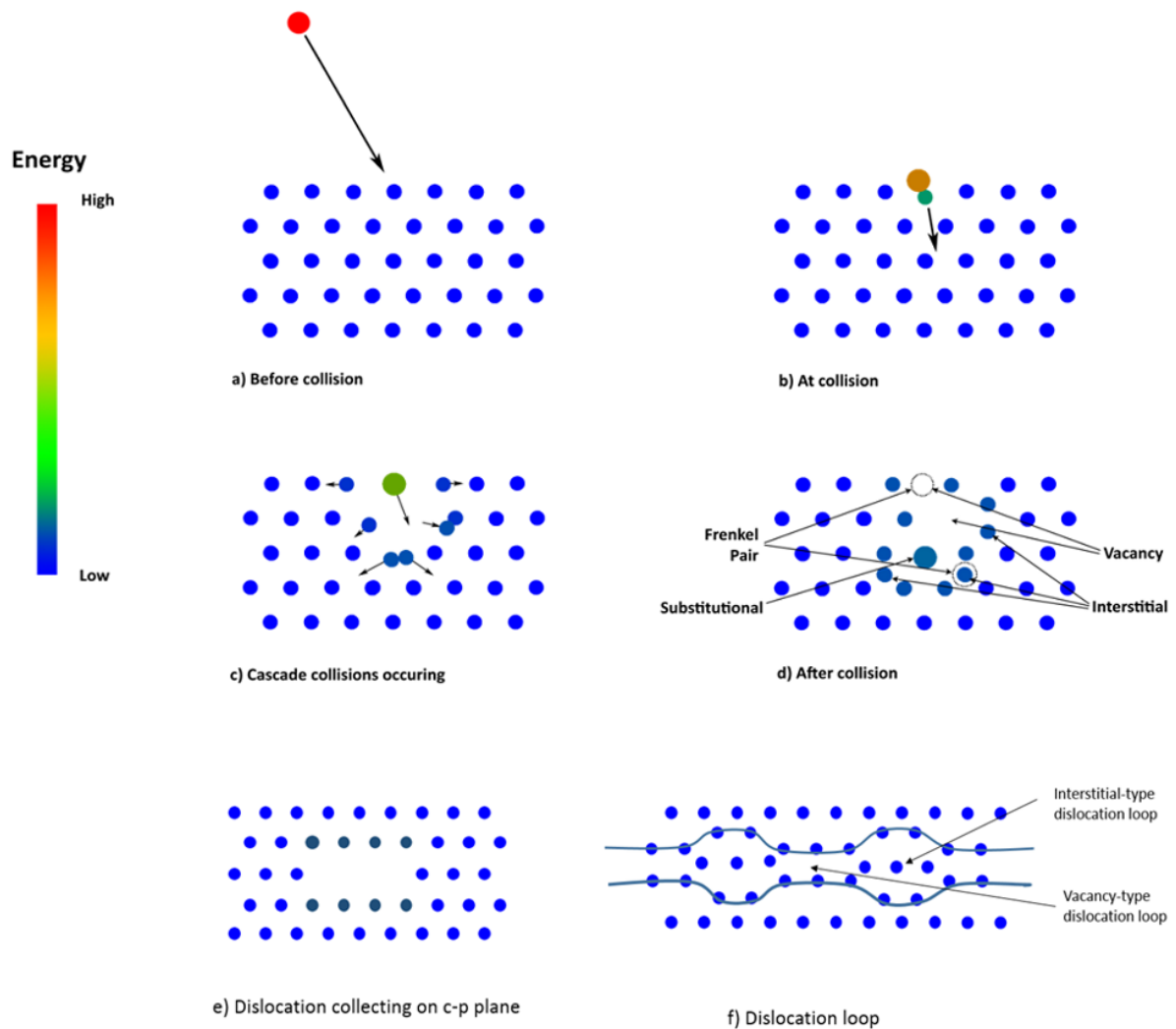


Figure 2.7 Irradiation effects on crystal structure. a) Before irradiation: high energy particle moving towards a lattice of low energy atoms. b) At collision: high energy particle impacts and dislocates a lattice atom. c) Cascade collisions: the PKA collides with and dislocates another atom. The radiation particle continues moving into the lattice, transferring more of its energy to other atoms. d) After collision: lattice now has high concentration of stress concentrations, vacancies, interstitials, and may have substitutional defects and is in a higher energy state. e) the dislocations collected on close-packed planes leaving vacancy-type dislocation loops. f) the atoms collapsed to form interstitial-type and vacancy-type dislocation loops [21].

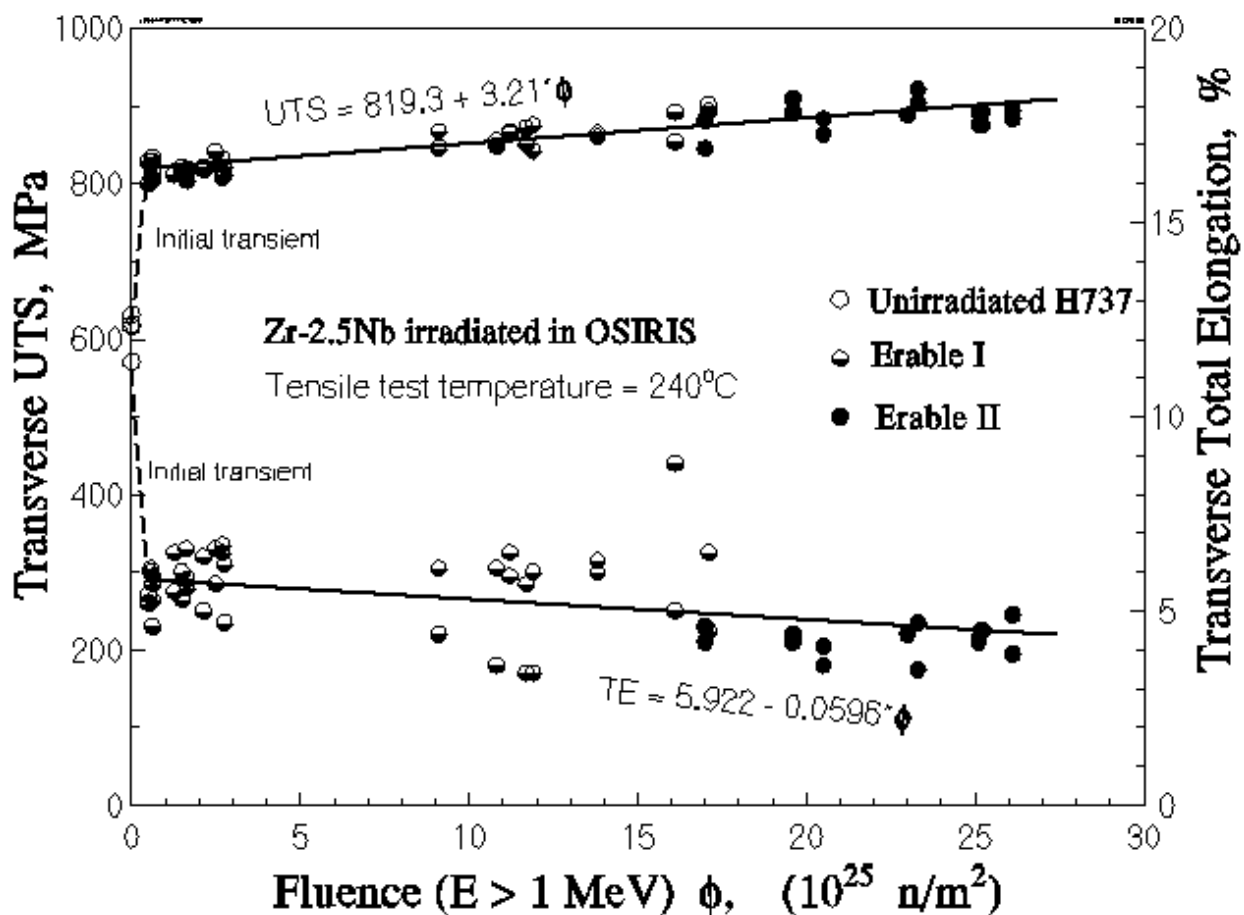


Figure 2.8 Transverse UTS and Total Elongation (TE) at 240°C versus fast neutron fluence ($E > 1$ MeV) for Erable I and II specimens irradiated in the OSIRIS test reactor [18].

2.4 The effect of helium accumulation

As was previously described, interaction of slow moving thermal neutrons with ^{58}Ni atoms results in an absorption/transmutation/decay process which releases helium atoms into the ^{58}Ni crystal. The small sized helium atoms occupy interstitial sites in the alloy but the solubility of helium within the nickel is quite low. Thus, the helium rapidly precipitates out at locations of crystal defects such as vacancies, vacancy complexes, dislocation loops, and grain boundaries [22], [23]. This eventually results in the formation of significant helium micro-bubbles within the metal's crystal structure (Fig. 2.8). These micro-bubbles cause the alloy to swell and become brittle [24]–[26].

Recent TEM studies were carried out on 7 at.% He implanted Cu/ Nb multilayer material to investigate the distribution of He bubbles [27]. Their studies indicated that the helium bubble size is relatively larger along grain boundaries than within the grains (Figure 2.8). Similarly, Judge et al [4] studied helium bubble formation in neutron-irradiated nickel-based Inconel X750 and confirmed that the helium bubbles accumulated at boundaries and precipitate interfaces (Figure 2.9) and may have resulted in the intergranular failure, decreased ductility and embrittlement of these alloys.

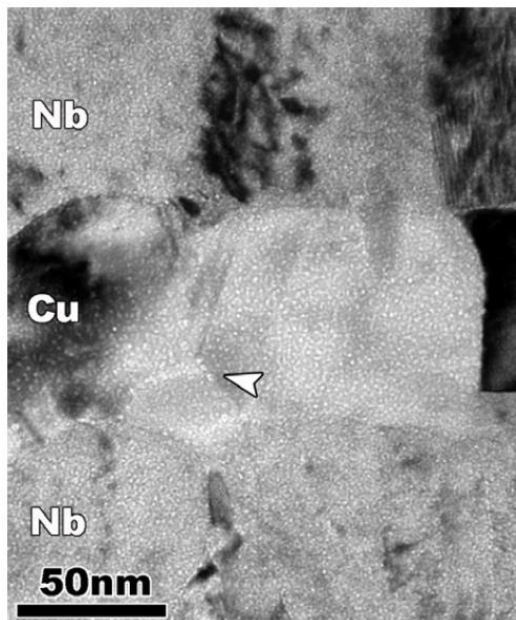


Figure 2.9 TEM image showing He bubble configuration in 70 nm Cu/Nb multilayer film after ~7 at.% He ion implantation at ~500 nm below [27]

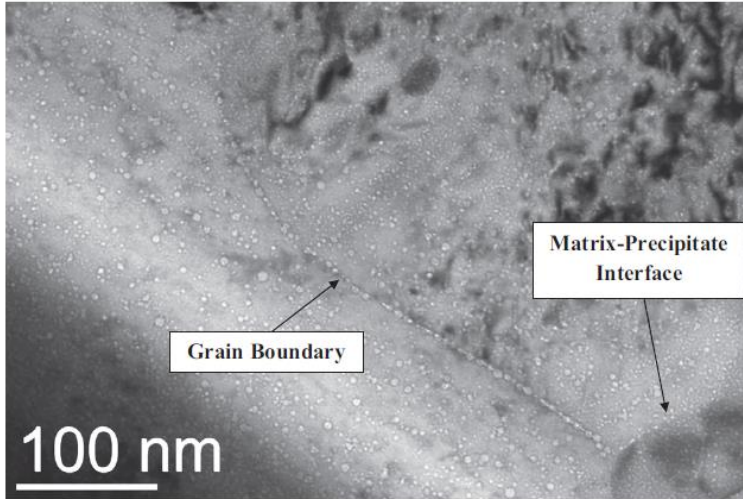


Figure 2.10 TEM micrograph in the under-focused condition (~500 nm) showing bubble alignment on grain boundaries and matrix–precipitate interface after irradiated at 300–330C to ~55 dpa and 18,000 appm He [4].

In recent studies, it has been found that helium voids and micro-bubbles are very strong obstacles to dislocation motion, and their hardening effect can be described by the Orowan hardening mechanism [27]–[29]. J.A. Knapp [28] performed an experiment where 1–5 at. % He was implanted in Ni at room temperature and at 200 °C. the helium ions produced a highly damaged layer extending to a depth of 700–800 nm in the Nickle substrate which contained a fine dispersion of He bubbles with diameters of 1.1 ± 0.2 nm. Helium implantation at 500 °C produced enlarged bubbles. Table 2.1 show that even ~1 nm diameter helium bubbles resist dislocations movement strongly and increase the hardness of the nickel by as much as 650% (Table 2.2).

Table 2.2 Implantation conditions and measured mechanical properties[28]

He concentration		Temperature	Young's Modulus	Yield Stress	Hardness	ΔH
(at. %)	(appm)	(°C)	(GPa)	(GPa)	(GPa)	(%)
unimplanted	0		192±9	0.15±0.01	1.1±0.1	0

1%	10000	25	234±13	1.29±0.13	4.0±0.3	264%
1%	10000	25	235±13	1.27±0.10	3.9±0.3	255%
1%	10000	200	204±8	1.14±0.08	3.5±0.2	218%
1%	10000	200	215±9	1.28±0.10	3.9±0.2	255%
1%	10000	500	212±11	0.82±0.08	2.5±0.2	127%
1%	10000	500	207±14	0.68±0.07	2.1±0.2	91%
3%	30000	25	233±13	1.95±0.13	5.8±0.4	427%
3%	30000	25	237±19	1.96±0.26	5.9±0.6	436%
3%	30000	200	225±10	1.88±0.14	5.6±0.3	409%
5%	50000	25	221±9	2.25±0.10	6.6±0.3	500%
5%	50000	25	220±11	1.98±0.15	5.9±0.4	436%
5%	50000	500	184±9	1.08±0.11	3.3±0.2	200%
5%	50000	500	206±13	1.09±0.15	3.4±0.3	209%
10%	100000	25	216±12	2.91±0.24	8.3±0.6	655%
10%	100000	25	227±12	2.89±0.24	8.3±0.6	655%

J.D. Hunn et al[22] showed that the accumulation of He cavities/bubbles significantly hardens the 316LN stainless steel alloy. They proposed that the helium bubbles may affect the hardness in two ways. In addition to presenting direct barriers to dislocation motion in the form of helium micro-bubbles, the implanted helium also acted to cause ion-induced atom displacement and, thus, small crystal defects which prevent the motion of dislocations. At approximately 1 at.% helium concentration, dislocation and loop pinning by helium filled cavities in the lattice became significant. A hardening saturation value of almost twice that observed for displacement damage alone was reached at ~20 at.% He [22].

When helium atoms are added to a Ni crystal, either by helium ion implantation or by neutron-induced α decay, helium micro-bubbles are formed simultaneously with dislocations and other crystal defects imparted by the ion-/neutron-atom collision process. Separating the effect of the helium microbubbles from that of the collision-induced crystal damage is a problem that is, as of yet, not well understood. Previous studies [22], [30], [31] performed on He⁺/Fe⁺ implanted Inconel 718 and stainless steel 316, recorded the increase in indentation hardness as a result of implanted

He and Fe (Figure 2.10). In order to have a better understanding of the effect of the helium atom inside the materials, the two samples were implanted with helium with concentration ranging from 0 to 10000 appm. The corresponding displacement damage ranged from 0 to about 2.7 dpa. Therefore, a second set of samples were irradiated with about 8 MeV Fe^{4+} ions in order to create the same amount of crystal damage in the same depth with helium atoms. This method can compare the effect of helium implantation and ion irradiation under a similar condition.

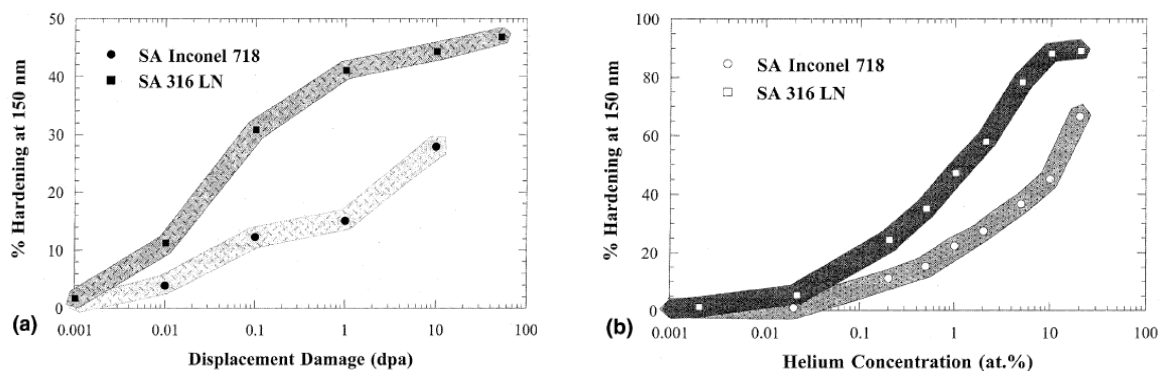


Figure 2.11 Comparison of percent hardening in SA Inconel 718 and SA 316LN stainless steel as a function of (a) displacement damage from 3500 keV Fe-irradiation and (b) helium concentration from 370 keV He-injection (360 keV for the 316LN).

Figure 2.11 compares the hardness of samples with similar dpa displacement damage caused by Fe ion implantation and helium implantation. For the same number of displacements the Fe implantation was initially more effective than helium implantation in hardening the alloy creating deformation inhibiting defects.

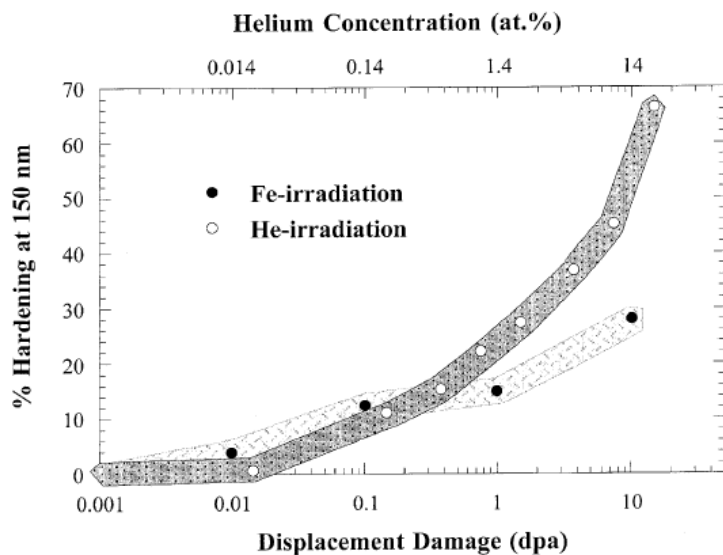


Figure 2.12 Percent hardening at 150 nm contact depth, relative to the unirradiated material, for SA Inconel as a function of displacement damage from 3500 keV Fe-ions and 370 keV He-ions. Upper axis shows the associated helium concentration for the He-irradiation (SA Inconel 718).

In summary, it should be noted that while the research described above clearly illustrates that accumulated helium increases the strength of nickel bearing alloys it does so via a mechanism involving the movement of nickel atoms. The effect of this process must therefore be a function of temperature and the rate of self-diffusion and helium-diffusion within the alloy. To date, little has been reported on the effect of temperature on the helium-induced hardening of nickel-bearing alloys. This subject will be dealt with in this thesis. As an introduction to this topic, the mechanisms by which solid-state atom diffusion occurs and the parameters by which it is described are reviewed below.

2.5 Solid-state atomic diffusion

2.5.1 Mechanisms of diffusion

Atomic diffusion is a basic requirement for helium bubble formation within a solid. Atom diffusion results from random jumps of atoms from one to another (meta-)stable lattice site within a crystal.

The energy required for this to occur is referred to as the thermal activation energy Q of the diffusion process and is shown schematically in Figure 2.12.

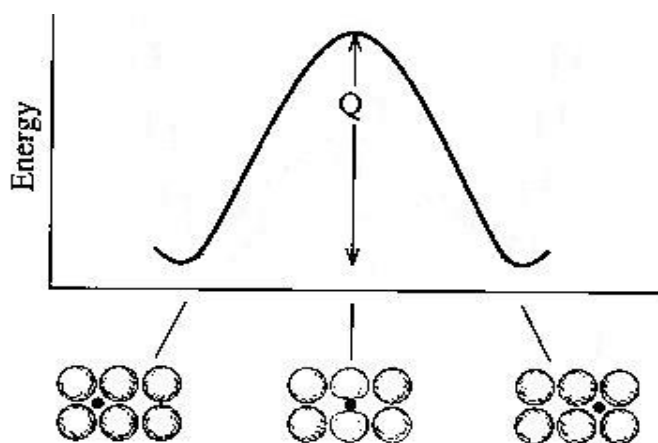


Figure 2.13 Schematic illustration of an interstitial atom, similar to helium in nickel, overcoming the energy barrier necessary to move from low energy, stable location to another location. The energy barrier is referred to as the activation energy Q .

A detailed review of the mechanisms by which He atoms can diffuse through crystalline solids has recently been published by Trinkaus et al.[32]. In helium diffusion, interstitial migration, vacancy mechanisms and dissociative diffusion mechanisms are the most important basic operative mechanisms. As shown in Figure 2.13 (a) a helium atom located in an interstitial position can migrate quickly through the lattice until it finds a sink such as a vacancy, grain boundary, dislocation or other surface. In this case the thermal activation energy for diffusion is quite low, $Q \approx 0.06$ eV[33]. As shown in Figure 2.13 (b), if the helium atom occupies a substitutional atom site within the crystal it can diffuse by a vacancy-diffusion mechanism, where the helium atom jumps from one to another vacancy. The activation energy of this mechanisms has been calculated by numerical simulation to be considerably higher ($Q \approx 0.67$ eV) [33]–[35]. As shown in figure 2.13 (c), the dissociation diffusion mechanism, where a helium atom diffuses interstitially from its thermal dissociation vacancy site until it is re-trapped by another vacancy, results in a calculated that is even higher ($Q \approx 2.36$ eV) [33]–[35].

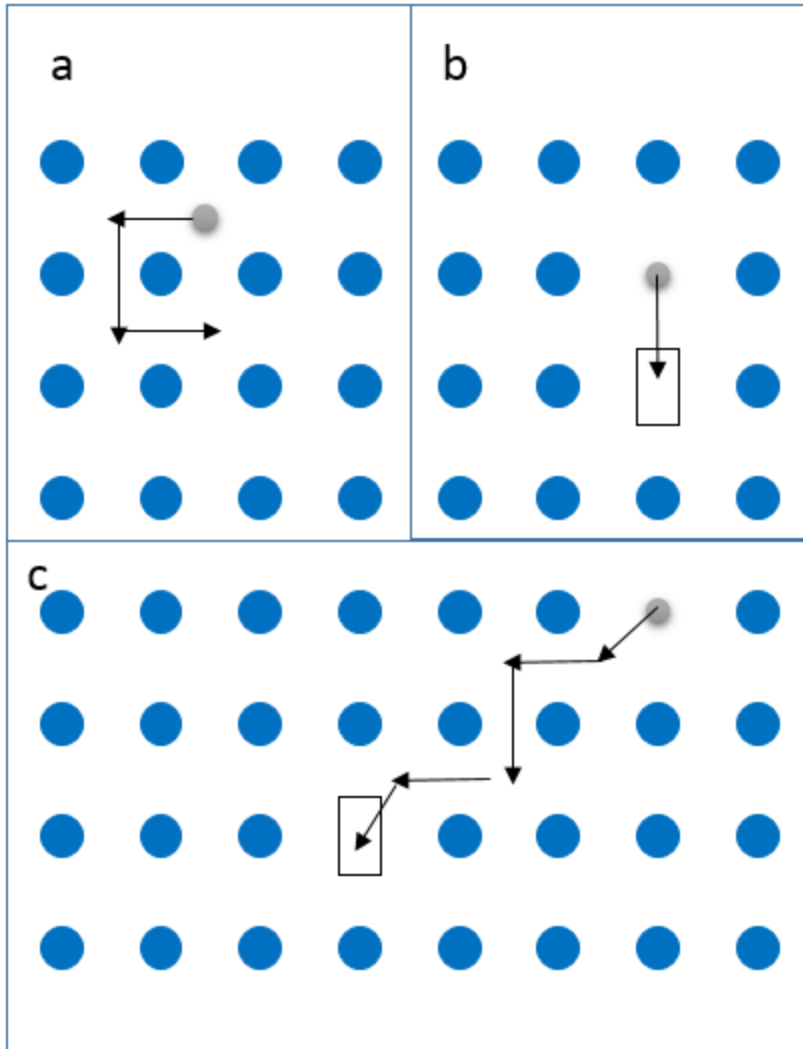


Figure 2.14 Schematic illustration of three mechanism for He diffusion without irradiation (a) interstitial migration, (b) vacancy mechanism, (c) dissociation mechanism

2.5.2 Role of diffusion in the deformation recovery process

The ability of atoms to move or diffuse increases with the increasing temperature and the probability P that an atom will move is related to the absolute temperature T by the following Arrhenius equation [36]:

$$P(T) = P_0 \exp\left(\frac{-Q}{RT}\right) \quad (2.1)$$

Where P_0 is a material dependent constant and R is the universal gas constant. Through diffusion, a highly worked-hardened metal will revert back to a lower hardness state, containing less crystal defects (i.e. dislocations, etc) when exposed to elevated temperature for an extended time. This process is referred to as thermal recovery and is characterized by the magnitude of Q , its apparent activation energy.

Many experiments have studied the rate of thermal recovery in a variety of work-hardened metal alloys [37]. One example of such a study of the recovery of hardness ΔH with time t and temperature of work-hardened single crystal zinc is shown in Figure 2.14. In this study, the ΔH data follow an Arrhenius relationship with t similar in form to Eq. 2 suggesting that the recovery process was in fact directly related to the process of solid state atomic diffusion.

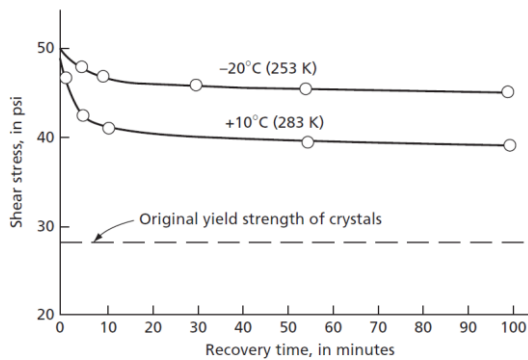


Figure 2.15 Recovery of the yield strength of single crystal zinc at 253 K and 283 K[37]

2.6 Strain rate sensitivity of indentation hardness

This chapter has already reviewed the effect that irradiation damage and accumulated helium have on increasing the hardness, which is analogous to increasing the yield stress, of metal alloys. This increase in hardness is due to the increase in crystal defect density, i.e. dislocation structures of various size and configuration and helium micro-bubbles. These defects will also affect the strain rate sensitivity of the indentation hardness and the nature by which they affect this strain rate sensitivity will depend upon the physical properties of the defects. When considering uniaxial deformation, the equivalent yield stress σ of most metals follows a power-law dependence upon both plastic strain ϵ and strain rate $\dot{\epsilon}$ as

$$\sigma(\varepsilon, \dot{\varepsilon}) = \varepsilon_0 \varepsilon^n \dot{\varepsilon}^m |_{T=const.} \quad (2.2)$$

where ε_0 , n , and m are material constants.

In the case of indentation hardness test performed with a geometrically self-similar pyramidal indenter, the average indentation strain rate is proportional to the rate of the loading rate \dot{P} over the indentation instantaneous load P (see Appendix A for a complete derivation of this expression). Indentation tests performed at various constant \dot{P}/P ratios yield different hardness (H) which are dependent upon the average indentation strain rate $\dot{\varepsilon}$. Since the indentation hardness (H) is directly related to yield stress σ and since, also, the indentation process, when performed with the common geometrically self-similar pyramidal indenter, is essentially a constant average strain process, H is also strain rate sensitive as

$$H(\dot{\varepsilon}) = H_0 \dot{\varepsilon}^m |_{T=const.} \quad (2.3)$$

Where H_0 is a material constant.

Recently, many studies have been conducted to assess the strain-rate sensitivity (m) and H for a wide range of metal systems [38]–[40].

The magnitude of the strain rate sensitivity parameter m (Eqs 5 and 6) reflects the physical characteristics of the microstructural obstacles that are impeding the plastic flow.

The strain rate sensitivity (m) parameter can be shown as[41]:

$$m = \frac{3\sqrt{3}kT}{V^*\sigma} \quad (2.4)$$

where k is the Boltzmann constant, T is the absolute temperature, and V^* is the activation volume for the plastic deformation, which is directly related to the operative deformation mechanism (see Appendix B for a complete derivation of this expression). Since this equation relates m to the parameter V^* , significantly changing V^* values indicate a change in the microstructural obstacles that limit the deformation rate of the test material.

Measuring the strain rate sensitivity of the indentation hardness therefore provides an effective way to assess the effect of ion implantation, and post-implantation annealing, on the size and strength of the ion-induced obstacles in the test material.

2.7 Summary

In this chapter, we have reviewed the key topics related to this thesis. The operation of the Canadian concept Gen. IV SCWR was introduced and the unique high temperature reactor core conditions were highlighted. The two candidate alloys, Inconel 800H and AISI 310, proposed for use in the highest temperature in-core components were introduced and the two principal irradiation induced phenomena; namely, irradiation-enhanced hardening and helium accumulation, were described. The role of temperature in affecting both of these phenomena by changing the rate at which atoms diffuse was highlighted. The effect that microstructural obstacles have on the strain rate sensitivity of the indentation hardness of a metal was introduced and its relationship to the apparent activation volume parameter V^* , which is characteristic of the obstacles controlling the deformation process, was described.

The next chapter describes experiments conducted on Fe^+ and He^+ implanted Inconel 800H and AISI 310 samples and an assessment of the stability of the resulting hardening with exposure to elevated temperature of 400C and 600C.

Chapter 3

3 Experimental procedure

This chapter describes the steps that were taken to prepare the samples and conduct the tests involved in this thesis. Section 3.1 describe the materials tested and the methods used to prepare samples for testing. Section 3.2 describes the He⁺ and Fe⁴⁺ implantations that were performed on the prepared samples. Section 3.3 describes the isothermal annealing procedure used to investigate the thermal stability of the ion implantation induced hardening of the samples. Finally, Section 3.4 describes the nanoindentation hardness tests performed on the implanted samples before and after thermal annealing.

3.1 Sample preparation

All experiments are performed on the two Fe-base alloys, AISI 310 and Inconel 800H which are candidate materials for the pressure tube liner and fuel cladding components of the Canadian concept Gen IV reactor [6], [7].

The AISI 310 and Inconel 800H material was acquired in the form of ½” thick bar stock from Rolled Alloys Inc[42], [43]. The chemical composition of both alloys is shown in the Table 3.1. 6 rectangular samples, 12.5×12.5 mm and 1 mm thick, were cut from the as-received bar stock using electric discharge machining.

One surface on each small sample was then ground smooth with wet silicon carbide (SiC) paper. This was accomplished by gluing the small samples to larger metal blocks that could be more easily gripped by hand. Grinding began with 180 grit SiC paper and proceeded through successively higher grit papers culminating with 4000 grit SiC paper. The ground samples were then mechanically polished on a felt cloth in an aqueous suspension of 0.05 μm silica abrasive. After polishing, the samples were thoroughly cleaned with distilled water and then alcohol.

Previous researchers have used similar mechanical polishing to prepare AISI 310 and Inconel 800H samples and found that it did not completely remove the plastically deformed material induced by polishing and the residual plastic deformation led to significant scatter in the measured nanoindentation hardness [21]. To remove this residual cold work the polished samples were

annealed at 1000°C for 15 minutes in an Argon atmosphere. The annealed samples were then lightly polished with an aqueous suspension of 0.05 μm Al_2O_3 abrasive to remove any surface oxidation resulting from the annealing process. Figure 3.1 displays the etched microstructure of the samples after annealing. The etching solution is 43% Glycerol, 28.5% HNO_3 and 28.5% HCL .

Table 3.1 Chemical composition, in weight percent, of AISI310 and Inconel 800H [42], [43]

	Cr	Ni	Mn	Si	Mo	C	Cu	P	S	Al+Ti	Fe
AISI 310	25	20.5	2	0.75	0.75	0.08	0.5	0.04	0.03	-	50.35
Inconel 800H	22.09	33	1.5	1	-	0.1	0.75	0.045	0.015	1	39.5

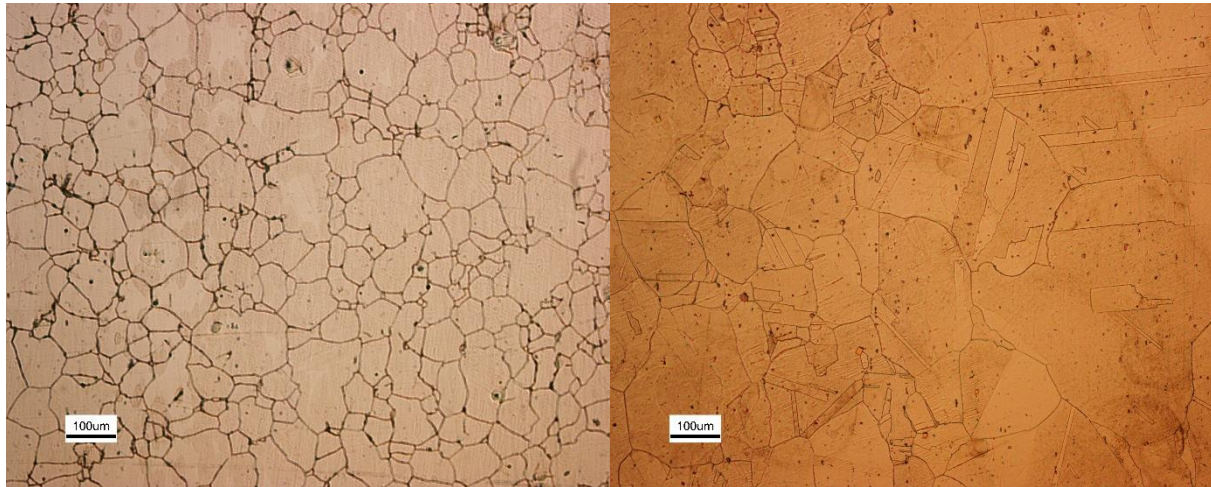


Figure 3.1 The microstructure of (a) AISI310 and (b) Inconel 800 H after annealing at 1000°C for 15 minutes.

Both alloys are primarily single phase and contain considerable twinning features. The average grain size for the AISI 310 alloy, is -between 10 and 100 μm diameter while, for the Inconel 800H alloy, is between 100 μm and 500 μm diameter.

3.2 Ion implantation

The polished, unetched, samples were exposed to various levels of He^+ and Fe^{4+} ion implantation using the Tandetron Ion Accelerator facility at the University of Western Ontario. The atom/ion scattering mechanisms are similar for both He^+ and Fe^{4+} implantation. Figure 3.2, negative ions He^- are extracted from an ion source and then injected into the accelerator. The injected negative ions are accelerated due to the applied electrostatic field (positive high voltage) on the terminal in the middle of accelerating tube. When the He^- passes through the Nitrogen Stripper gas at the high voltage terminal at the center, 2 electrons are stripped off to produce He^+ . If a higher energy is required 3 electrons can be stripped off to produce He^{2+} . The beam is now composed of positive ions. A focusing electrostatic quadrupole doublet is mounted at the end of the high-energy side of the accelerator, together with an analyzing magnet and proper X and Y steering systems for focusing of the positive beam onto the samples.

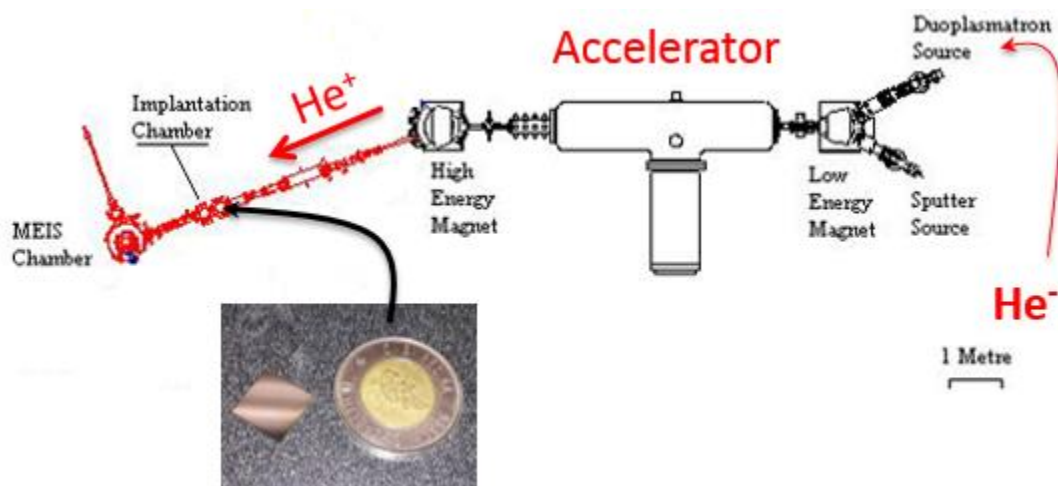


Figure 3.2 Schematic illustration of the Tandetron ion accelerator located at Western University Ontario.

Various energy ion implantations were performed to achieve a region, of approximately $2.0 \mu\text{m}$, beneath the surface of the sample where the amount of ion implantation and implantation-induced crystal damage were constant. This was determined by using the standard numerical simulation software Stopping Range of Ions in Materials (SRIM) which incorporates the Kinchin-Pease model to simulate the ion-substrate interactions to determine the average distance travelled, and

atom displacements caused, by an ion, of a specific charge, energy, and species[22], [44], [45]. helium ions of four energy levels (825, 950, 1075, and 1200 keV) were implanted at room temperature. The SRIM simulation indicated that this implantation process resulted in a uniform distribution of He within about a 2 μm depth beneath the sample surface (Figure 3.3 and 3.4). By controlling the length of time that the samples were exposed to the He^+ beam regions of the polished samples were implanted with 0, 100, 320, 1000, 3160, 10000 atomic parts per million (appm) of helium (Figure 3.4) and we define C_{He} (appm) as the concentration of helium.

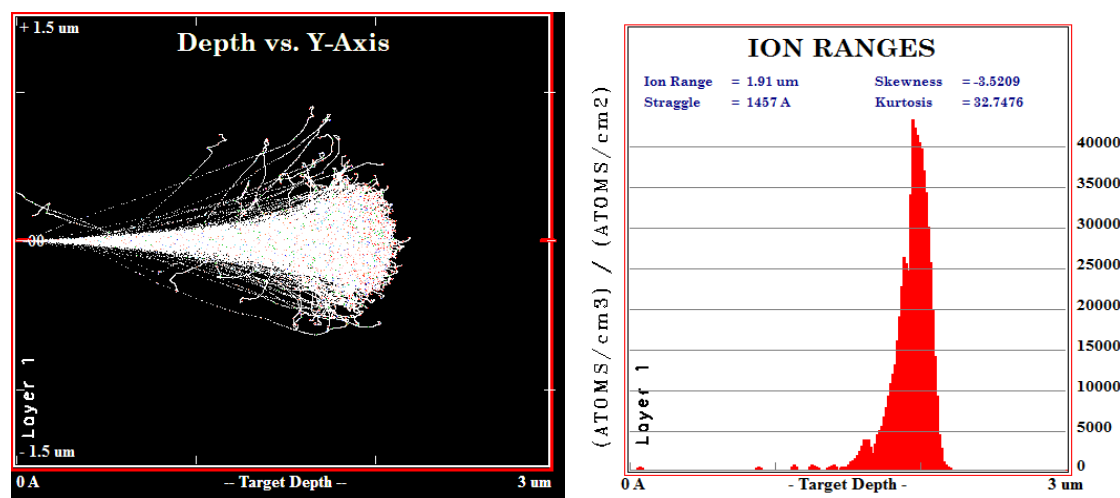
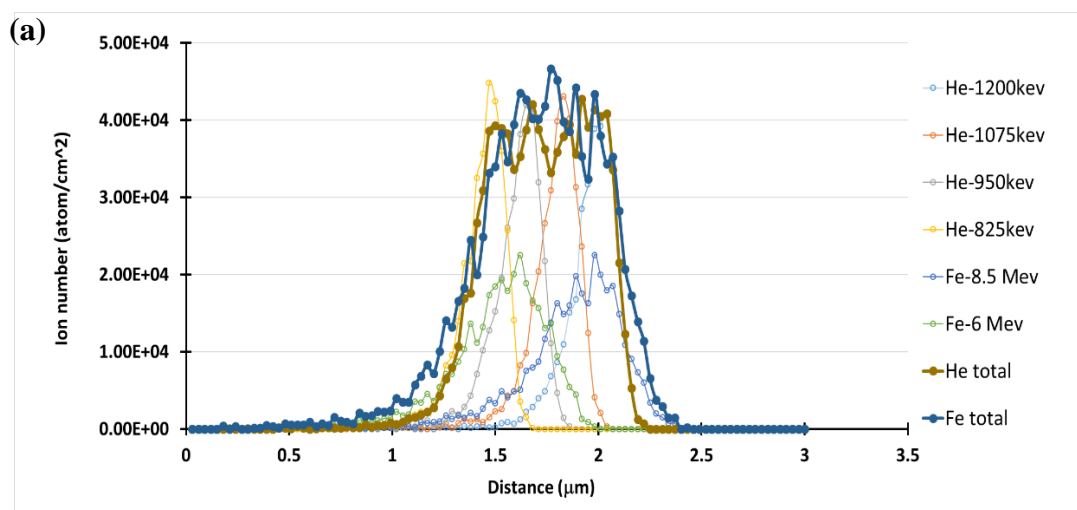


Figure 3.3 SRIM simulation of the penetration of 1200keV He^+ ions into AISI310 alloy (a) the simulated ion trajectories (b) the He ion range at around 2 μm depth



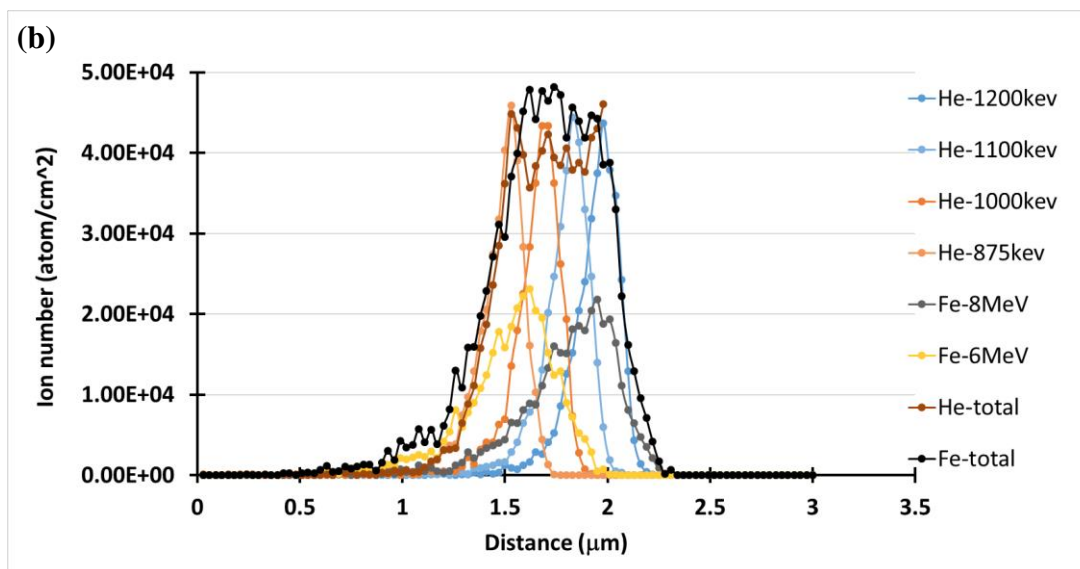


Figure 3.4 SRIM calculation of He⁺ and Fe⁴⁺ with multiple energies implanted into (a) Inconel 800H alloy (b) AISI 310 alloy

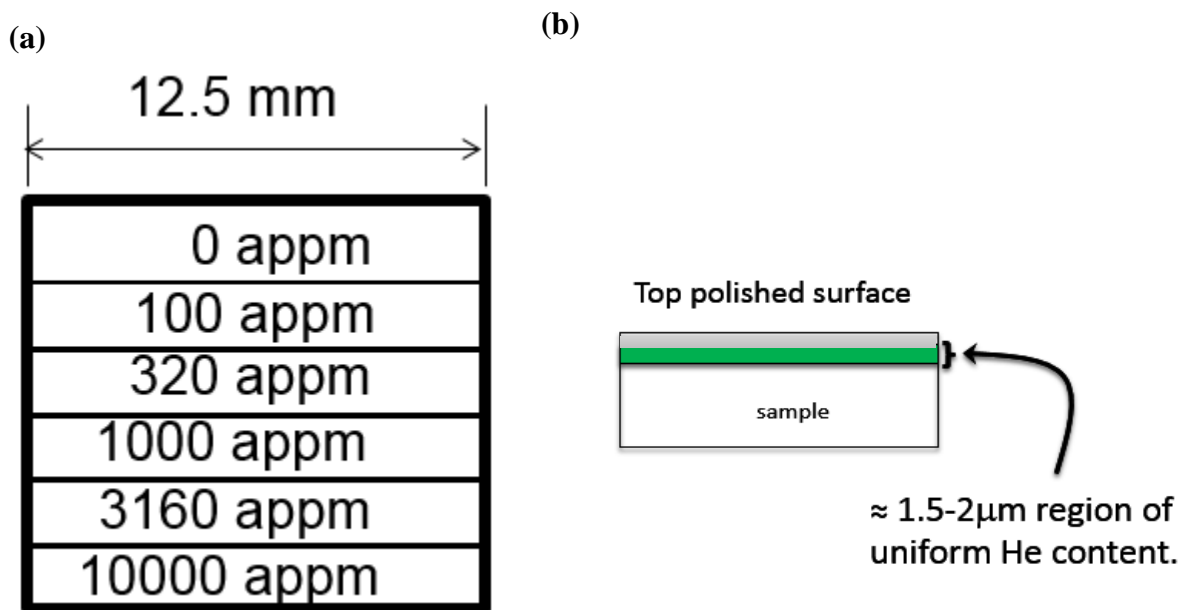


Figure 3.5 Figure 3.5 Schematic illustration of the regions of helium ion implantation : (a) top view (b) side view

As shown in Figure 3.5, all high energy ion irradiation results in atoms in the irradiated samples being displaced from their equilibrium locations. While the majority of these atoms quickly return to their equilibrium locations, some remain permanently displaced leaving behind a crystal defect in the form of a vacancy, a vacancy cluster, or a small dislocation loop generated by a collapse of a vacancy cluster [6], [21]. While the region 1,5 to 2 mm is the uniform helium content, all the region from the surface to the 2 mm depth was effective by helium implantation. The level of ion-induced crystal damage is usually expressed in units of displacements per atom ρ_{He} (dpa) which can be calculated with SRIM software as.

$$\rho_{(He)} = \frac{\text{Ion flux} * \text{displacement per ion}}{\# \text{ of atom per cm}^2} \quad (3.1)$$

The calculated ρ_{He} (dpa) resulting from He^+ implantations C_{He} (appm) is shown in Figure 3.6.

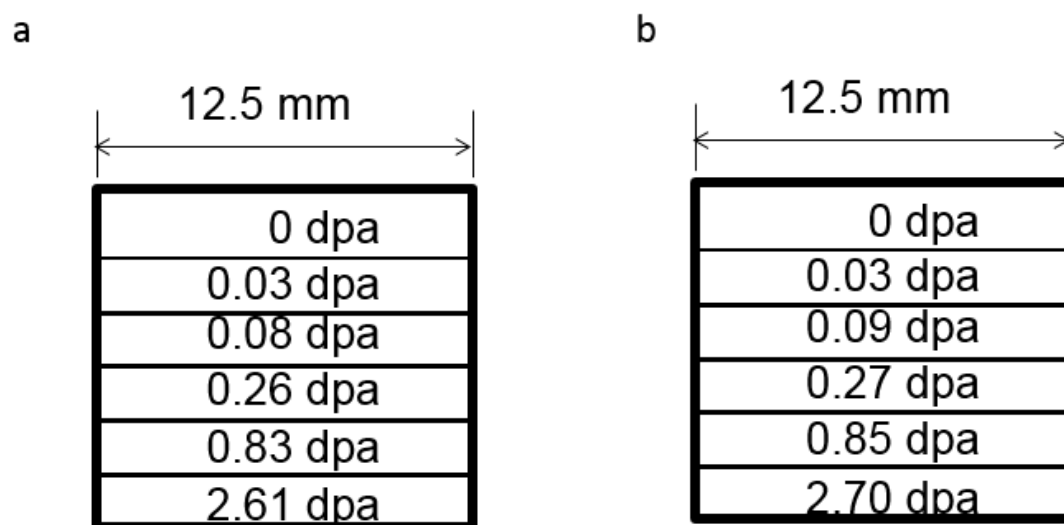


Figure 3.6 Schematic illustration of typical regions of ion exposure for samples used in the experiment (a) AISI 310 (b) Inconel 800H

3.3 Thermal annealing

In order to study the effect of temperature on the stability of the He^+ induced hardening within the AISI 310 and Inconel 800H materials, isothermal anneals were performed on He^+ implanted samples for various lengths of time at 400 and 600°C. The furnace system used for the annealing is shown in Figure 3.7 and consists of a moveable Vycor tube within an electrical resistance furnace. An atmosphere of 98% argon and 2% Hydrogen was maintained in the tube. The 2% hydrogen reacts with residual oxygen within the gas and thus prevent oxidation of the ion implanted samples. When the furnace temperature reached the annealing temperature (400 or 600°C), the Vycor tube was moved such that the test samples were placed in the central hot zone of the furnace and kept there for predetermined annealing times (1, 4, 10, and 40 min).

The overall experimental test matrix is shown in the Table 3.2.

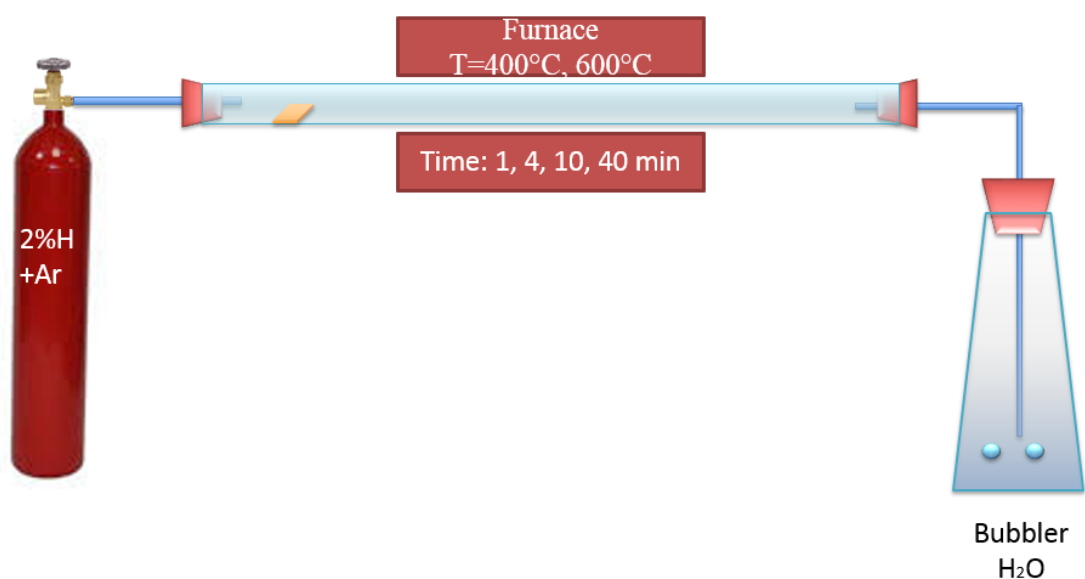


Figure 3.7 Schematic illustration of the annealing furnace

Table 3.2 The experiment procedure in this thesis

T(C)	t(min)	He content										
		0 appm						100 appm	320 appm	1000 appm	3160 appm	10000 appm
		0 dpa	0.02 dpa	0.08 dpa	0.2 dpa	0.8 dpa	2.7 dpa					
400	0	H(25), S(12*4), H(20)	H(20)	H(20)	H(20)	H(20)	H(20)	H(25), S(12*4)	H(25), S(12*4)	H(25), S(12*4)	H(25), S(12*4)	H(25), S(12*4)
	1	H(25), H(20)	H(20)	H(20)	H(20)	H(20)	H(20)	H(25)	H(25)	H(25)	H(25)	H(25)
	4	H(25), H(20)	H(20)	H(20)	H(20)	H(20)	H(20)	H(25)	H(25)	H(25)	H(25)	H(25)
	10	H(25), S(12*4), H(20)	H(20)	H(20)	H(20)	H(20)	H(20)	H(25), S(12*4)	H(25), S(12*4)	H(25), S(12*4)	H(25), S(12*4)	H(25), S(12*4)
	40	H(25), H(20)	H(20)	H(20)	H(20)	H(20)	H(20)	H(25)	H(25)	H(25)	H(25)	H(25)
600	0	H(25)						H(25)	H(25)	H(25)	H(25)	H(25)
	1	H(25)						H(25)	H(25)	H(25)	H(25)	H(25)
	4	H(25)						H(25)	H(25)	H(25)	H(25)	H(25)
	10	H(25)						H(25)	H(25)	H(25)	H(25)	H(25)
	40	H(25)						H(25)	H(25)	H(25)	H(25)	H(25)

H--Hardness test

S--strain rate test (0.05,0.25,0.5,1 sec⁻¹)

3.4 Nano indentation tests

The effect of Fe⁴⁺ and He⁺ implantation and thermal annealing on the mechanical properties of Inconel 800H and AISI 310 was determined by performing nano-indentation hardness tests. The tests were performed at the room temperature (25°C) using a NanoTest indentation machine (Micro Materials Ltd, Wrexham UK) with a diamond Berkovich indenter, shown in Figure 3.8.

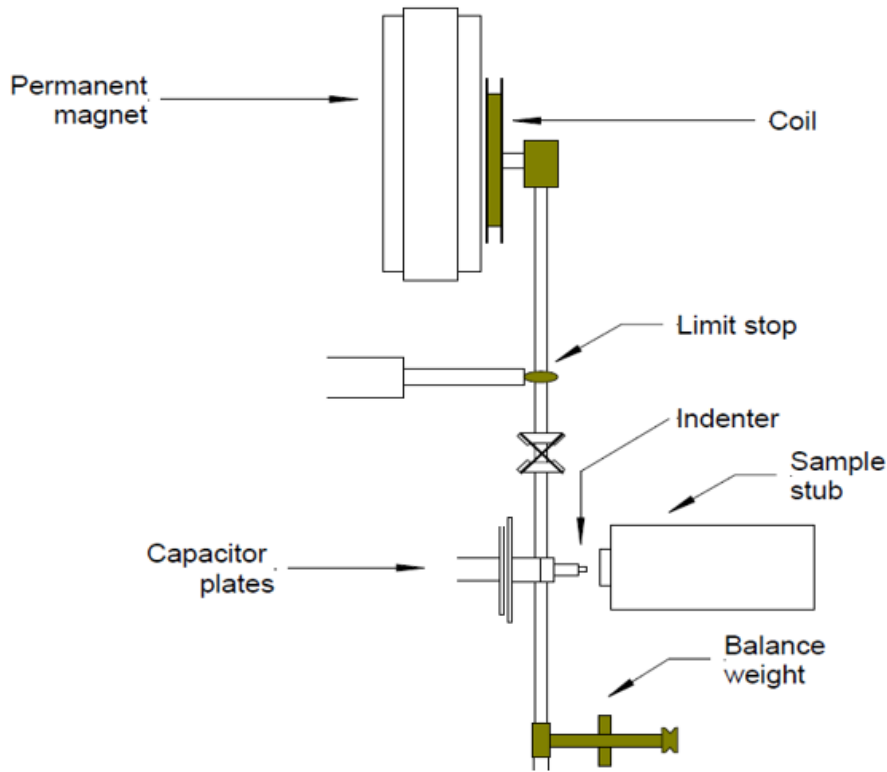


Figure 3.8 Schematic illustration of the NanoTest indentation hardness testing platform.

In this study, 20 to 25 indentations were performed under each test $\text{He}^+/\text{Fe}^{4+}$ implantation condition (Table 3.2). For each test, consisted of performing an indentation at a constant average indentation strain rate of $\dot{\epsilon}_{ind} = \frac{\dot{F}}{F} = 0.04 \text{ sec}^{-1}$. For each test a partial unloading was performed at indentation depths of $h_1=170\text{nm}$, $h_2=200\text{nm}$, and $h_3=230\text{nm}$ (Figure 3.9). Each indentation was about $50 \mu\text{m}$ apart (Figure 3.9). The indentation hardness was determined as

$$H = \frac{F}{A(h_c)} \quad (3.2)$$

Where F is the indentation force, h_c is the plastic indentation depth, obtained from the $F - h$ data by extrapolating the partial unloading curve to $F = 0$ and $A(h_c)$ is the indentation depth dependent projected contact area of the indentation. $A(h_c)$ is dependent upon the precise shape of the

pyramidal indenter and is obtained as a polynomial function of h_c by performing indentations on a standard sample of quartz.

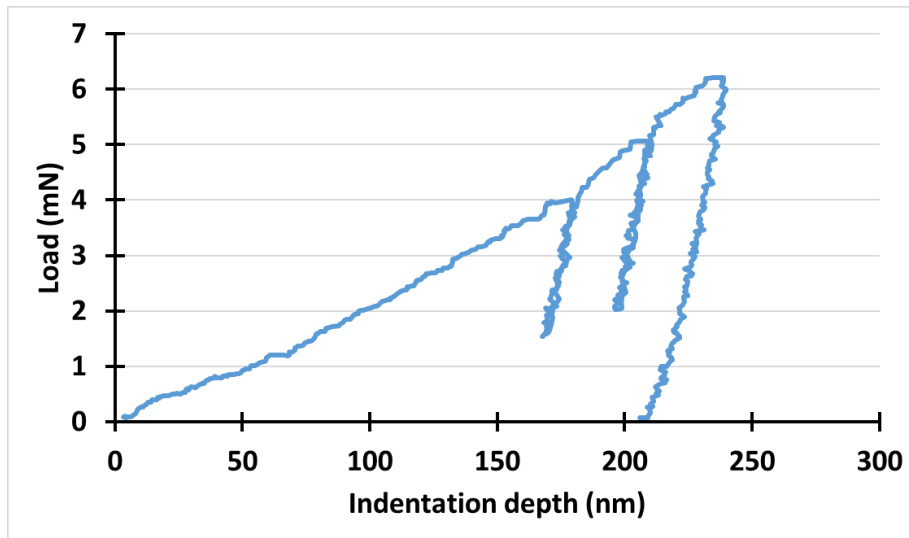


Figure 3.9 The indentation force versus depth

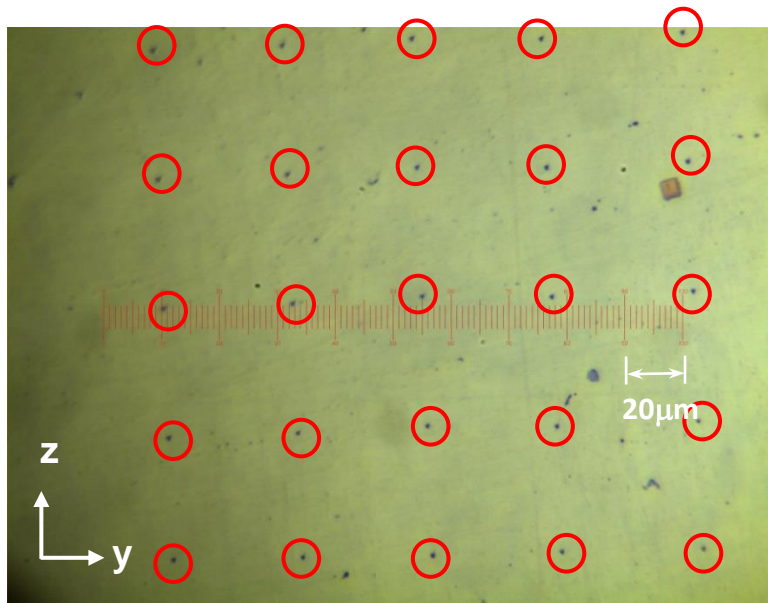


Figure 3.10 The indentation point on the surface of the sample

3.5 Strain rate sensitivity of the indentation hardness

Another way to analyse the effect of $\text{He}^+/\text{Fe}^{4+}$ implantation on the hardening of the test material is to compare the indentation hardness H obtained from indentation tests performed at different

values of average indentation strain rate $\dot{\epsilon}_{ind}$. Most alloys display a power-law dependence of H upon $\dot{\epsilon}_{ind}$. Changes in the power-law exponent m of this dependence indicate changes in the configuration, i.e. the apparent activation volume V^* , of the obstacles within the material's microstructure which result in the measured hardness. The relationship between H , m and V^* is given as [38]–[40]

$$V^* = \frac{3\sqrt{3}KT}{mH} \quad (3.3)$$

Where k is the Boltzmann constant and T is the absolute temperature. In this study we performed indentation hardness tests ($h = 200$ nm) at $\dot{\epsilon}_{ind} = 0.05, 0.25, 0.50, \text{ and } 1.0 \text{ sec}^{-1}$ on selected samples (Table 3.2) to determine if He^+ implantation resulted in changes to the parameters of m and V^* . About 15 indentations were performed, for each sample, at each strain rate (Figure 3.11).

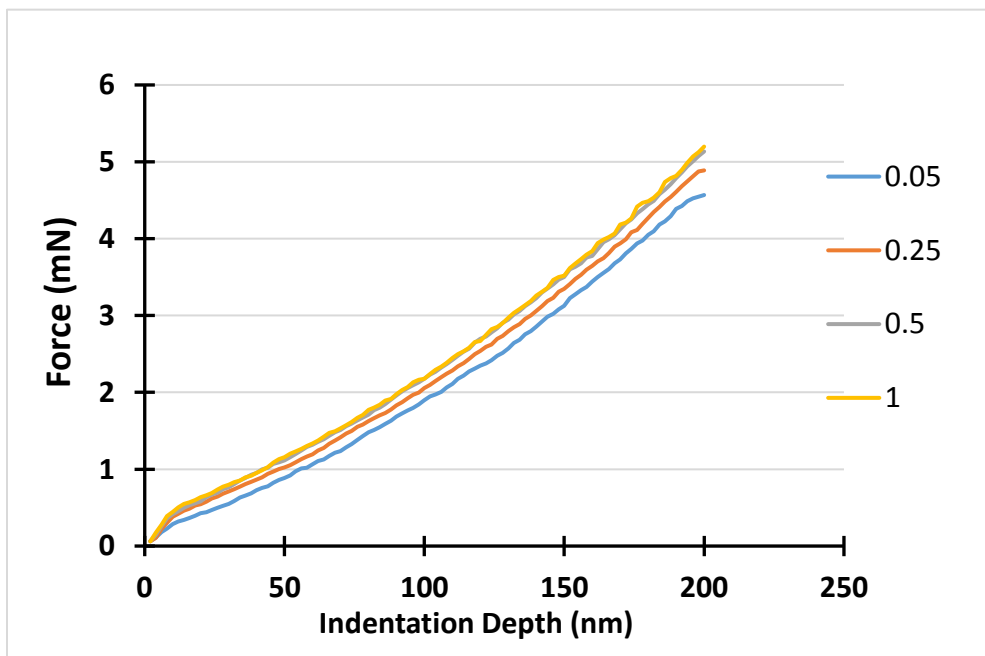


Figure 3.11 The indentation load versus indentation depth curves under $\dot{\epsilon} = 0.05, 0.25, 0.5, 1 \text{ s}^{-1}$ on Inconel 800H with no annealing and no helium implantation.

Chapter 4

4 Experimental Results

4.1 Indentation hardness of He⁺ and Fe⁴⁺ implanted samples

Figure 4.1 shows a plot of the indentation hardness of the AISI 310 and the Inconel 800H samples as a function of implanted helium level. The indentation hardness, measured at an indentation depth of about 200 nm, increases nonlinearly with increasing helium concentration, from 0 to 10000 appm. The indentation hardness of the 10000 appm helium implanted samples is increased by 34% and 27% relative to the unimplanted AISI 310 and Inconel 800H samples respectively.

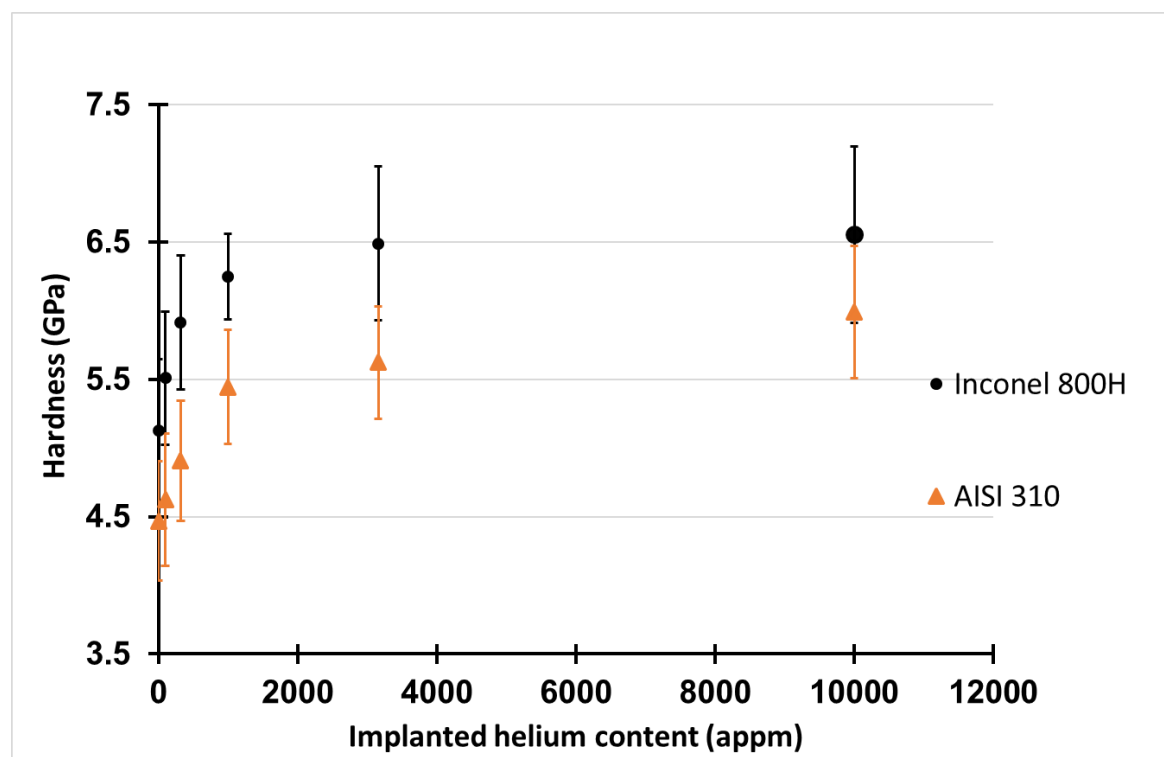


Figure 4.1 Indentation hardness versus helium concentration for the AISI 310 and the Inconel 800H alloys.

Figure 4.2 shows a plot of the indentation hardness as a function of Fe⁴⁺ implantation-induced irradiation damage for the AISI 310 and the Inconel 800H alloys. Similar to Figure 4.1, the indentation hardness increases nonlinearly with increasing irradiation damage from 0 to 2.7 dpa.

The hardness of the 2.7 dpa implanted samples was increased by 24% and 15% relative to the unimplanted AISI 310 and Inconel 800H samples respectively.

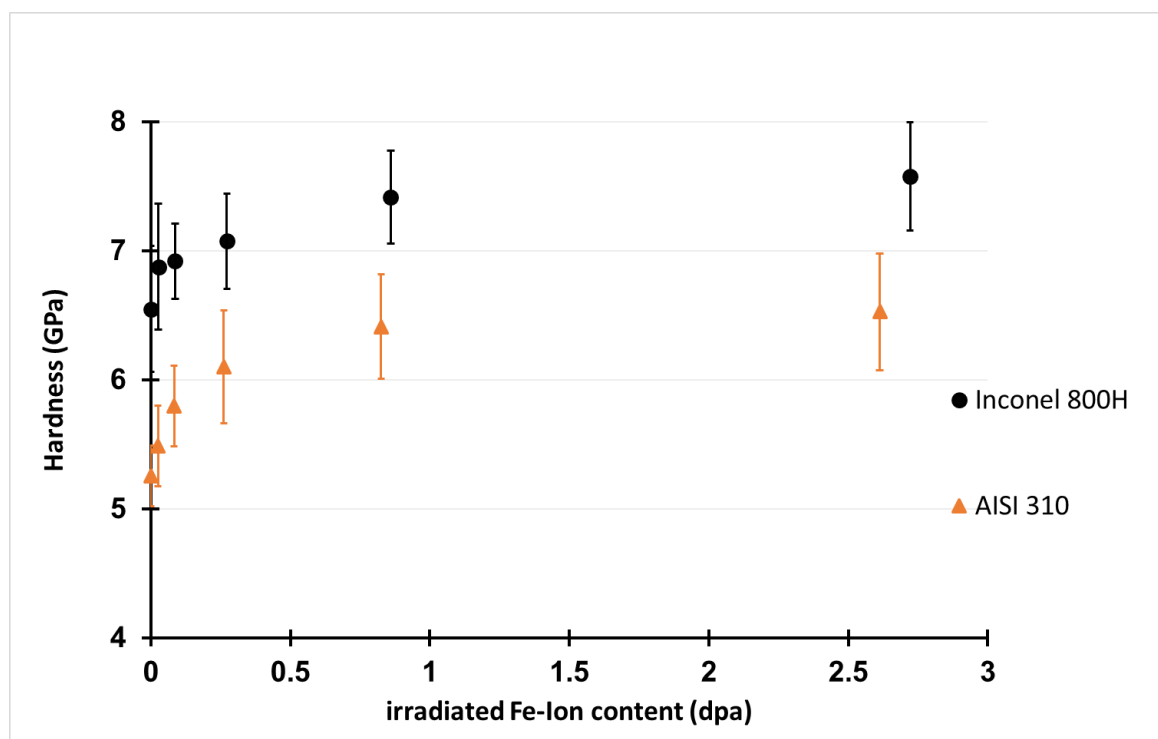


Figure 4.2 Indentation hardness versus Fe^{4+} induced irradiation damage for the AISI 310 and the Inconel 800H alloys.

4.2 Indentation hardness after annealing

Figures 4.3(a,b) display the indentation hardness, at 200 nm indentation depth, as a function of annealing time at 400°C of the He^+ implanted AISI 310 and Inconel 800H alloys while Figures 4.4(a,b) show similar plots for the alloys when annealed at 600°C.

Figures 4.5(a,b) display the indentation hardness, at 200 nm indentation depth, as a function of annealing time at 400°C of the AISI 310 and Inconel 800H alloys that were Fe^{4+} implanted to induced various levels of dpa crystal damage.

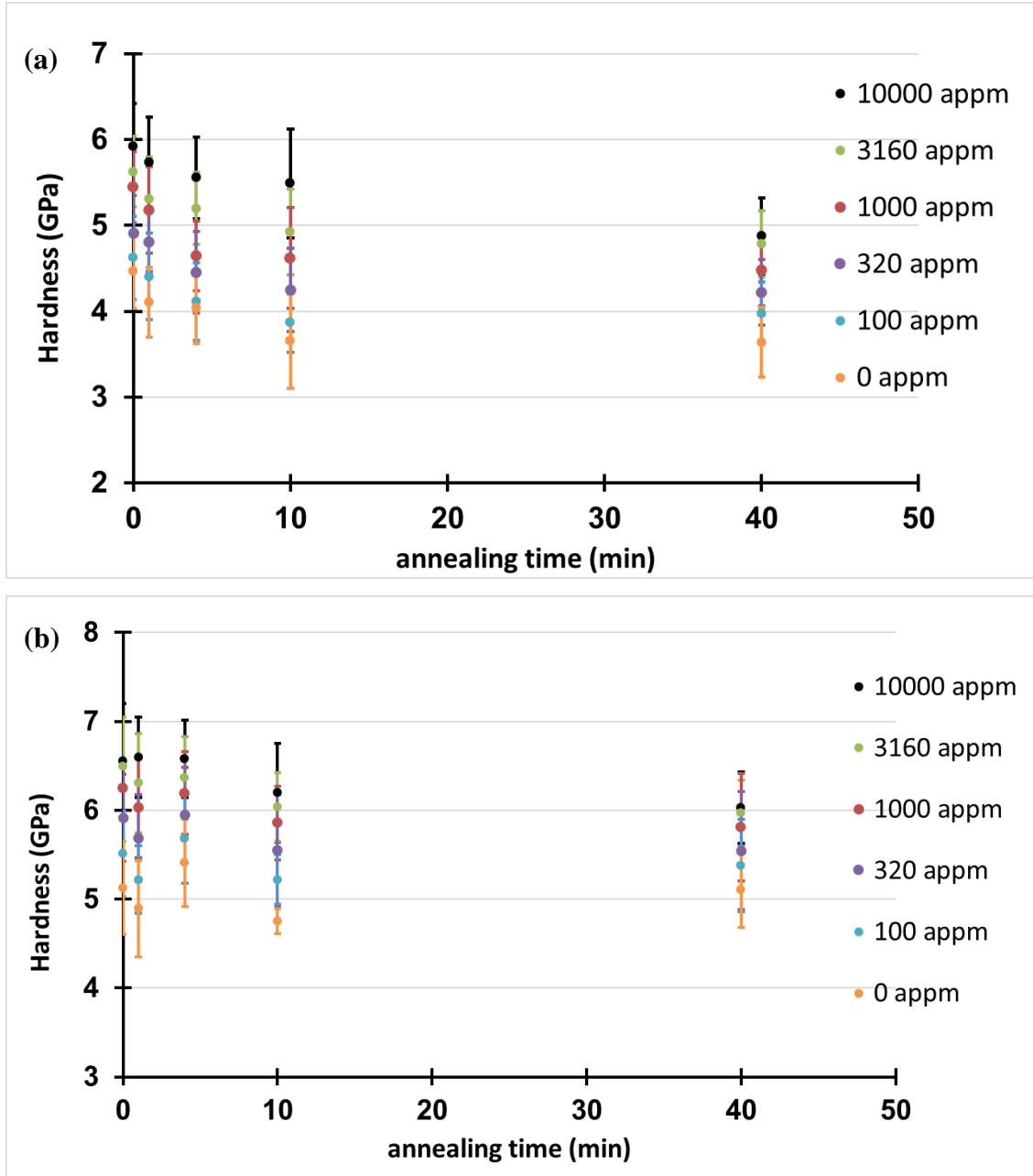


Figure 4.3 Indentation hardness as a function of annealing time (400°C) for (a) AISI 310 samples and (b) Inconel 800H samples with different appm levels of implanted helium.

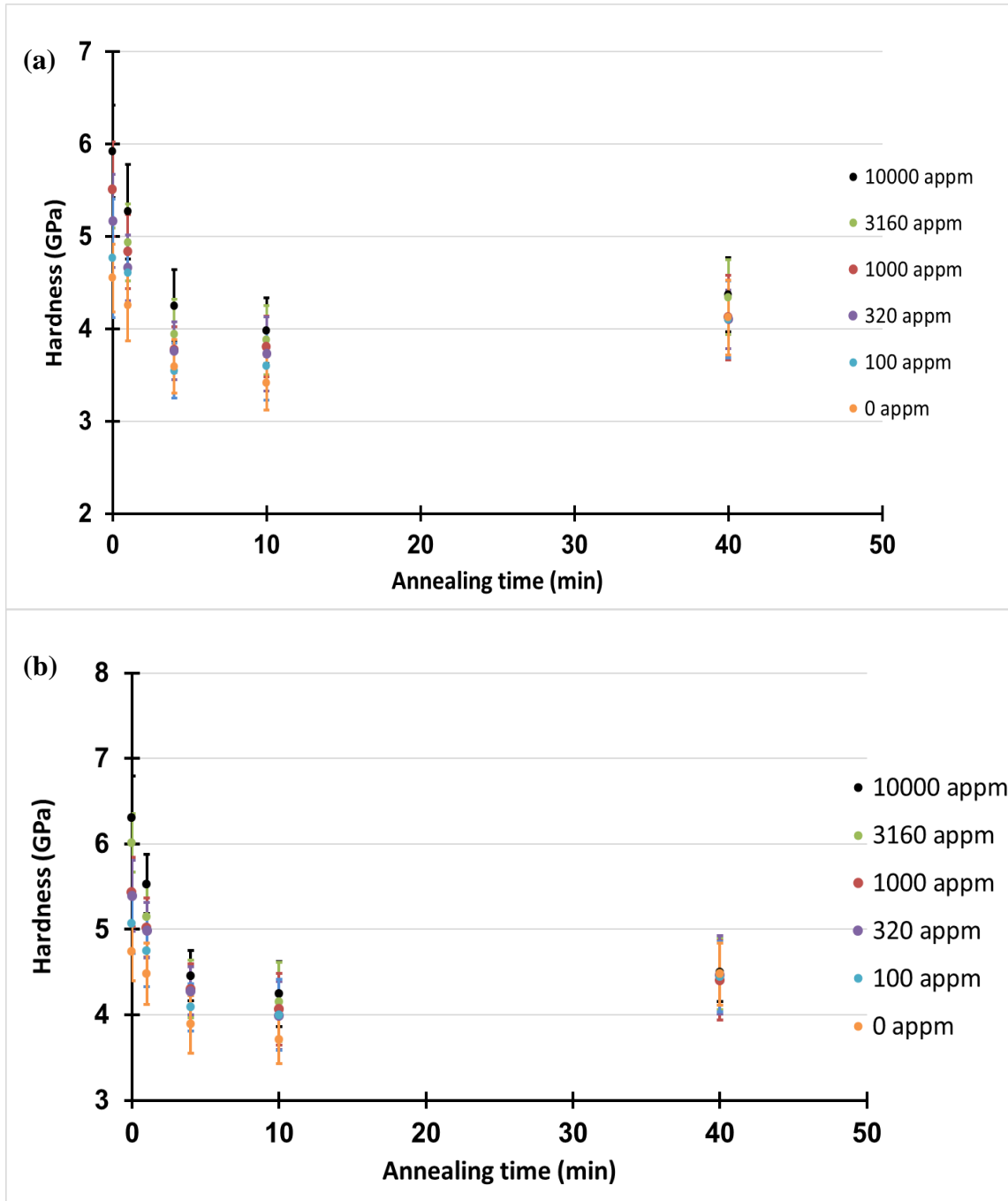


Figure 4.4 Indentation hardness as a function of annealing time (600°C) for (a) AISI 310 samples and (b) Inconel 800H samples with different appm levels of implanted helium.

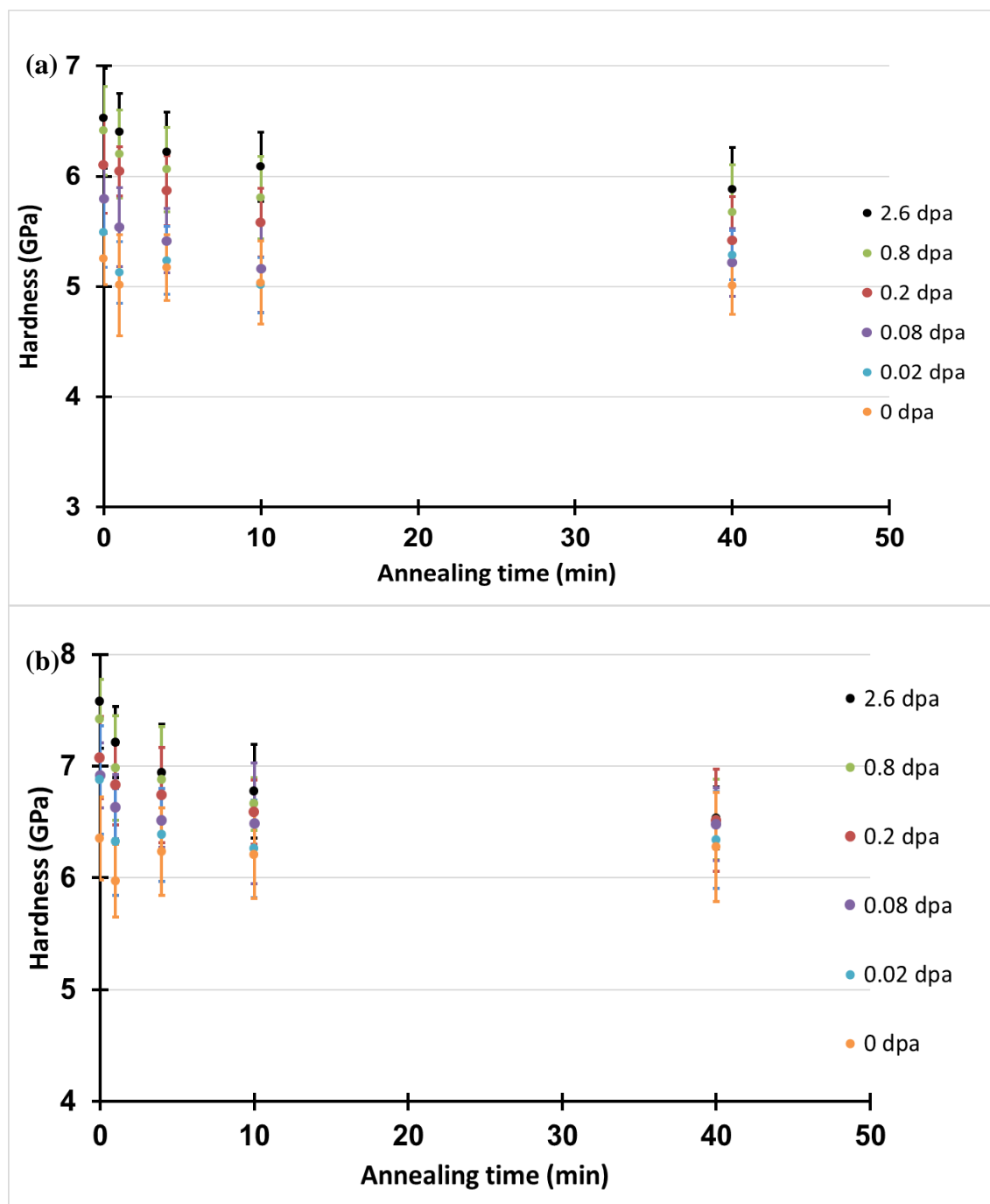


Figure 4.5 Indentation hardness as a function of annealing time (400°C) for (a) AISI 310 samples and (b) Inconel 800H samples with different dpa levels of Fe⁴⁺ implanted irradiation damage.

Both alloys tested show a slightly different dependence of indentation hardness upon annealing time when annealed at 600°C than at 400°C. While annealing at either temperature results in a

significant rapid initial decrease in hardness, the hardness continues to decrease, at a slower rate, with continued annealing time for the samples annealed at 400°C but actually increases slightly for the samples annealed at 600°C (Figures 4.4). This is attributed to the development of thin oxide layers with time on the surface of the samples that were annealed at the higher temperature.

Optical micrographs of the polished samples after annealing for various lengths of time at 600°C are shown in Figures 4.6 and 4.7. The figures indicate quite clearly the grain size and shape and the fact that, for both alloys, the grain morphology does not change appreciably with annealing time.

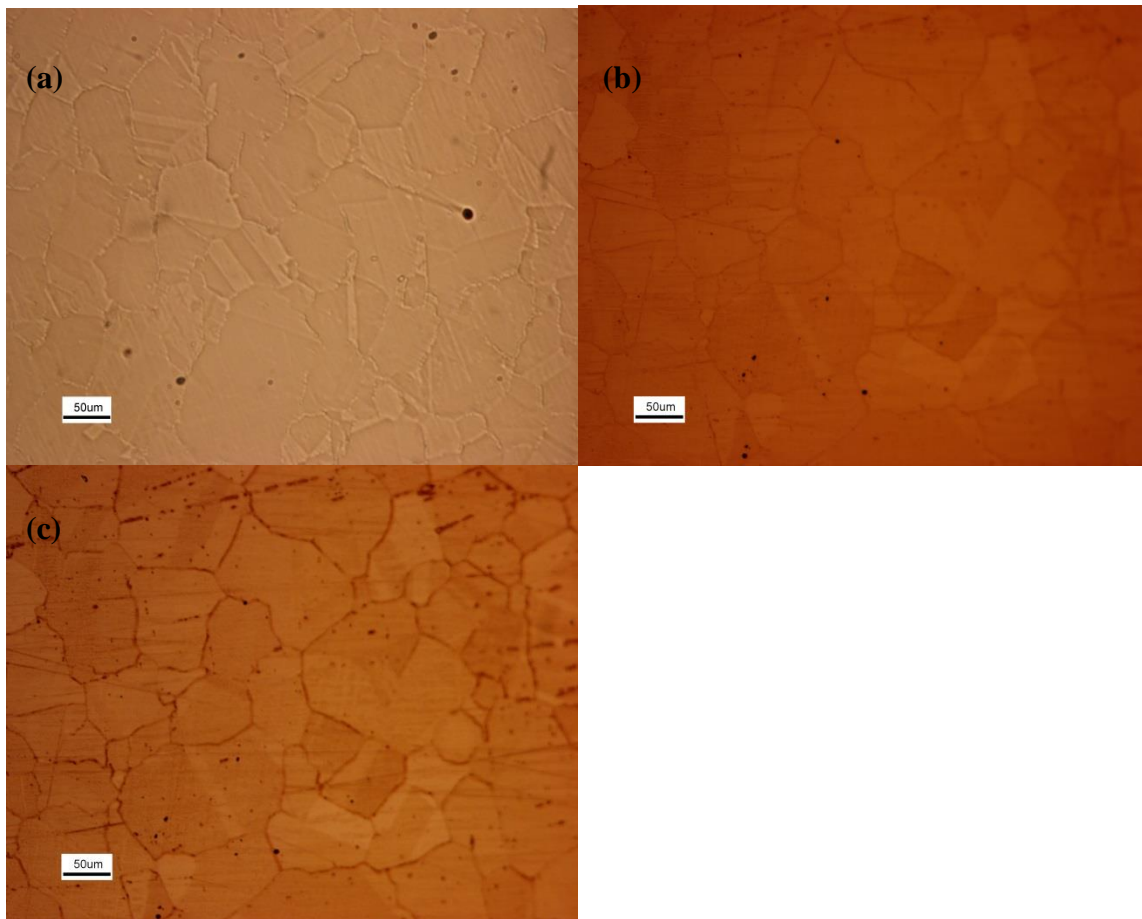


Figure 4.6 Microstructure of the AISI 310 alloy after annealing at 600C for: (a) 0 min, (b) 10 min, and (c) 40 min.

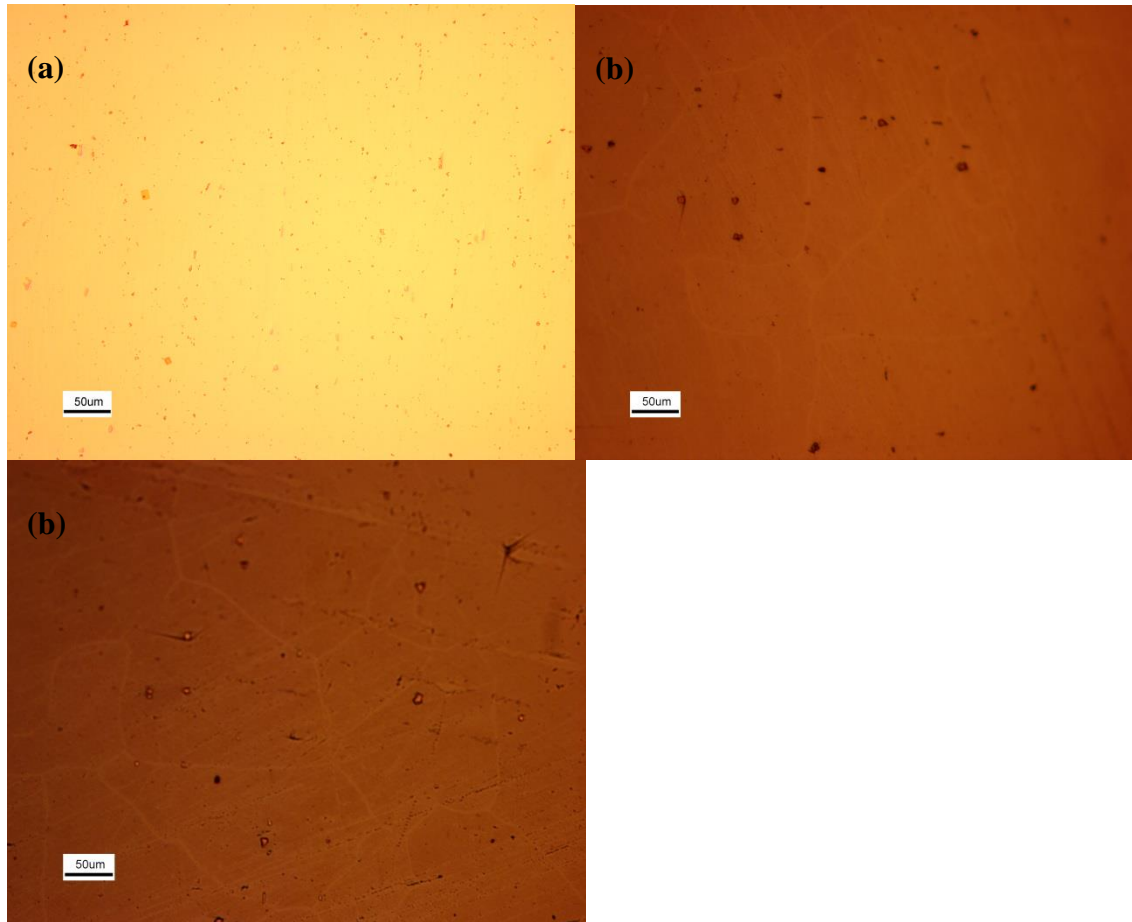


Figure 4.7 Microstructure of the Inconel 800H alloy after annealing at 600C for: (a) 0 min, (b) 10 min, and (c) 40 min.

4.3 The effect of helium atoms on strain rate sensitivity

Indentation hardness tests were performed under constant \dot{P}/P conditions corresponding to constant average indentation strain rates of 0.05, 0.25, 0.5, 1 s^{-1} . These tests were performed on both AISI 310 and Inconel 800H samples containing different levels of implanted helium; 0, 100, 320, 1000, 3160, 10000 appm. Figure 4.8 shows logarithmic curves of indentation hardness verses indentation strain rate for the nonannealed AISI 310 and Inconel 800H samples. For both samples the increase in indentation hardness, corresponding to an indentation depth of 200nm, increases with increasing indentation strain rate.

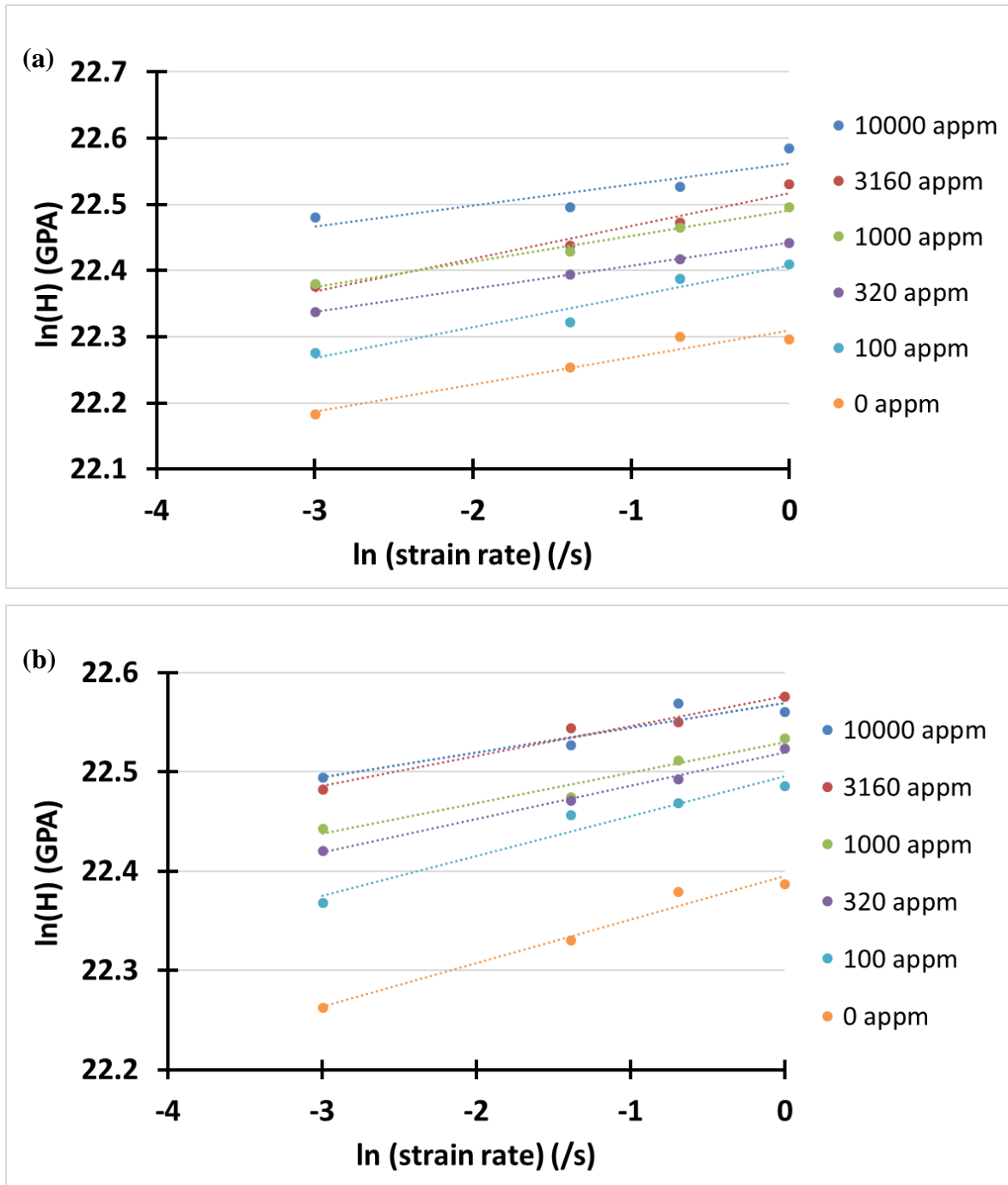


Figure 4.8 The indentation hardness versus indentation strain rate ($\dot{P}/P = 0.05, 0.25, 0.5, 1 \text{ s}^{-1}$) on (a) AISI 310 and (b) Inconel 800H with no annealing and with different helium implantation content.

Figure 4.9 shows logarithmic curves of indentation hardness versus indentation strain rate for the AISI 310 and Inconel 800H samples that were annealed for 10 minutes at 400°C. The slopes of the linear data trends in Figs. 4.8 and 4.9 represent the strain rate sensitivity, m , of the indentation hardness and are given in Tables 4.1 and 4.2

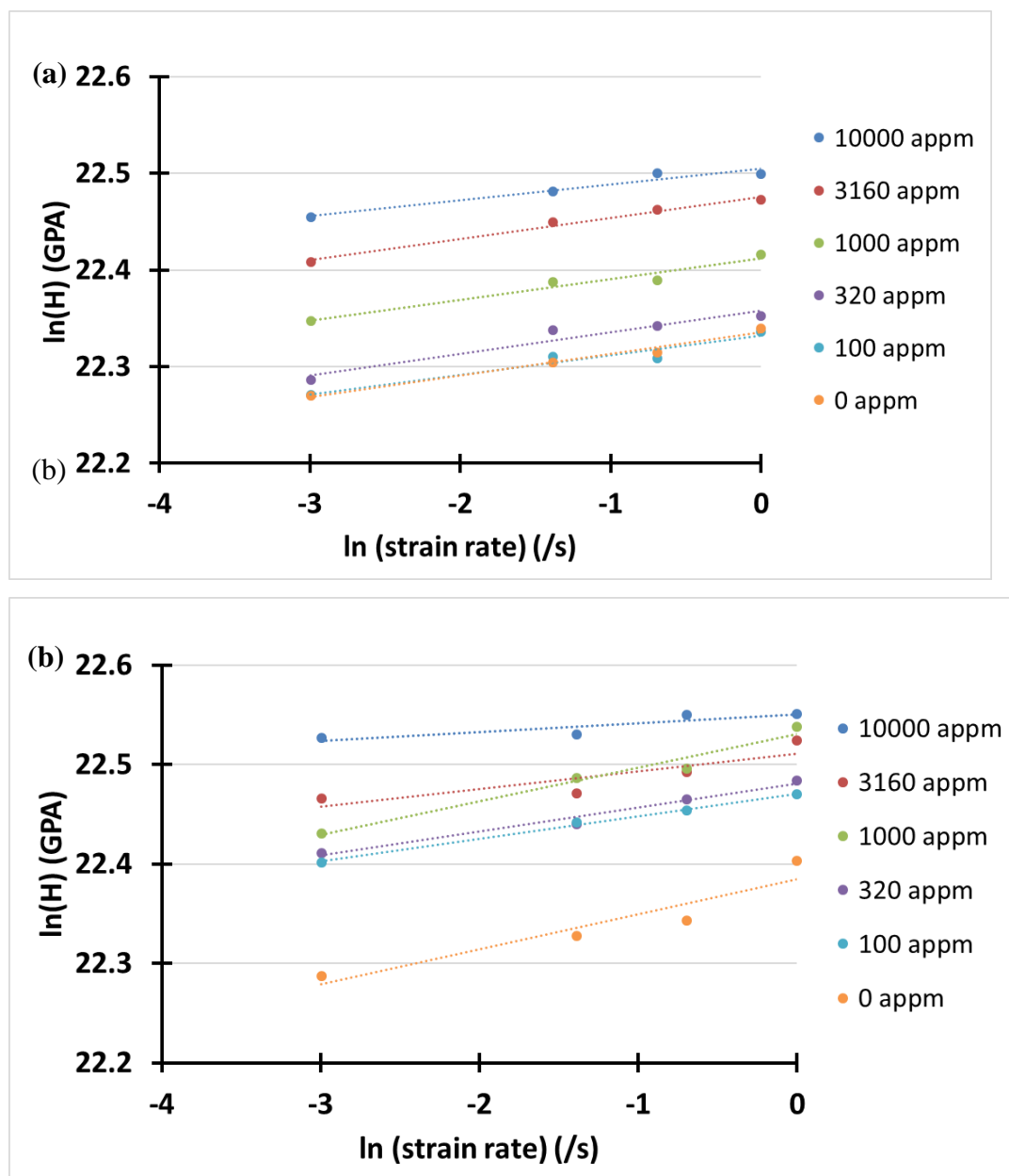


Figure 4.9 The indentation hardness versus indentation strain rate ($\dot{P}/P = 0.05, 0.25, 0.5, 1 \text{ s}^{-1}$) on (a) AISI 310 and (b) Inconel 800H with 10 min annealing at 400°C with different helium implantation content

Table 4.1 The strain rate sensitivity m of the indentation hardness of the AISI310 and Inconel 800H samples subjected to various implanted helium levels with no subsequent annealing

	$C_{He}(\text{appm})$	10000	3160	1000	320	100	0
AISI 310	m	0.0318	0.0496	0.0387	0.0347	0.0463	0.0411
	Δm	0.010	0.007	0.003	0.0003	0.008	0.007
Inconel 800H	m	0.0249	0.0304	0.0306	0.0335	0.04	0.0452
	Δm	0.007	0.004	0.004	0.002	0.006	0.007

Table 4.2 The strain rate sensitivity m of the indentation hardness of the AISI310 and Inconel 800H samples subjected to various implanted helium levels and subsequent 10 minute annealing at 400°C

	$C_{He}(\text{appm})$	10000	3160	1000	320	100	0
AISI 310	m	0.0163	0.0218	0.0215	0.0223	0.0202	0.0222
	Δm	0.003	0.002	0.003	0.004	0.004	0.002
Inconel 800H	m	0.0089	0.0179	0.0339	0.0243	0.0228	0.0354
	Δm	0.003	0.007	0.004	0.002	0.001	0.009

Chapter 5

5 Discussion

The data presented in Chapter 4 show clearly that the indentation hardness of the AISI 310 and the Inconel 800H alloys is dependent upon, among other things, the accumulated helium concentration, the amount of ion irradiation damage, and post irradiation annealing. In this chapter, we will analyse further effect of this two parameters in order to understand in more detail the stability of the obstacles to plastic deformation created within these alloys by the implantation of He^+ ions. We will focus our attention on characterizing the thermal stability of these obstacles by first assessing their effect on the rate at which the indentation hardness decreasing when the samples are heated at 400°C and 600°C. We will then further characterize the nature of the obstacles by assessing the effect of the implanted He^+ and Fe^{4+} ions on the strain rate sensitivity of the indentation hardness before- and after- exposure to elevated temperature. From these analyses, we will determine the thermal activation parameters that control the indentation hardness and which provide fundamental information on the nature of the dislocation glide limiting obstacles introduced to the alloys when they are implanted with He^+ and Fe^{4+} ions. This information is critical for understanding how the strength of the AISI 310 and the Inconel 800H alloys responds to high temperature neutron irradiation conditions characteristic of fuel cladding and the liner tube in-core components within the Canadian Concept Gen IV SCWR.

5.1 Effect of implanted He^+ and Fe^{4+} ions on the hardness

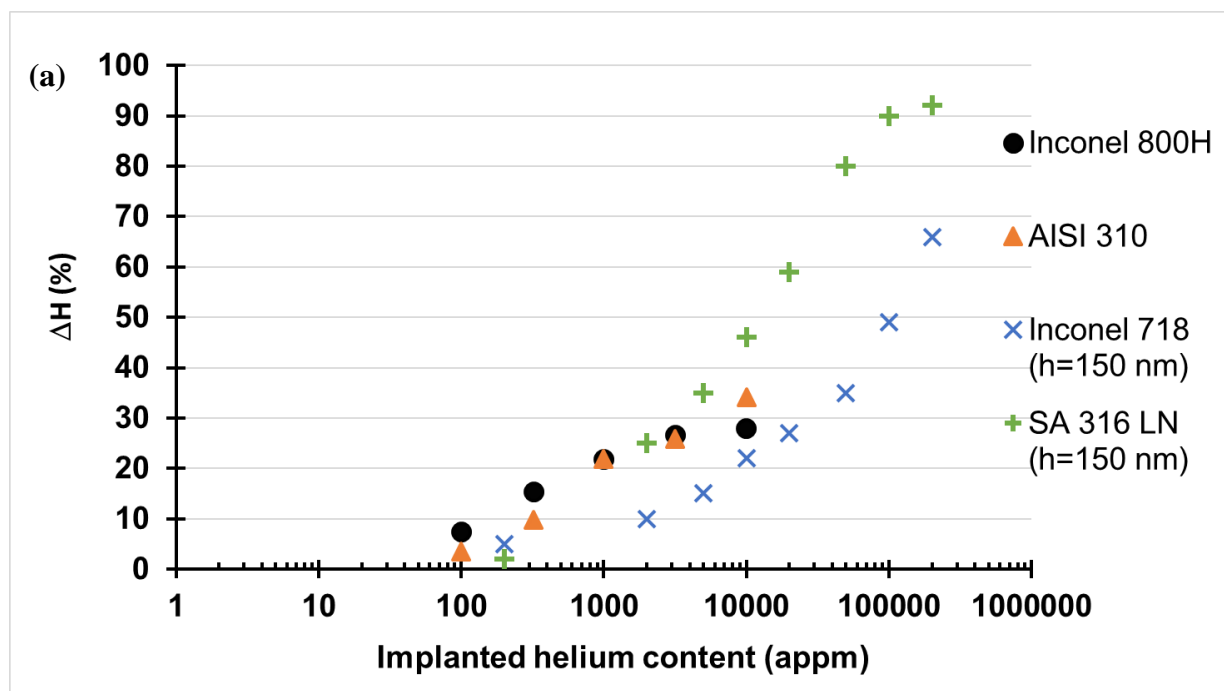
Figure 5.1 depicts the change in indentation hardness ΔH of the AISI 310 and the Inconel 800H alloys that results from He^+ and Fe^{4+} implantation. In these plots the change in hardness is calculated as

$$\Delta H|_{h=200nm} = (H_{\text{implanted}} - H_{\text{non-implanted}})|_{h=200nm} \quad (5.1)$$

Both He^+ and Fe^{4+} implantation increase the hardness of the alloys and our measured hardness

values are similar to those which has been previously reported for ion implantations performed on similar, but not exactly the same, alloys and ion implantation conditions (Figure 5.1). These graphs indicate clearly increasing hardness as a result of ion implantation, the exact dependence of the hardness as a function of the amount of implantation is rather complex, as indicated by the scatter in the data from various investigators, and is likely to be affected by several variables including:

- i) Compositional/microstructural differences in the test material from researcher to researcher,
- ii) Small differences in indentation depth (measured indentation hardness is strongly indentation depth dependent at depths less than 1 μm [46]).
- iii) Differences in ion implantation energy (particularly for the case of He^+ implantation).
This effect is described below.



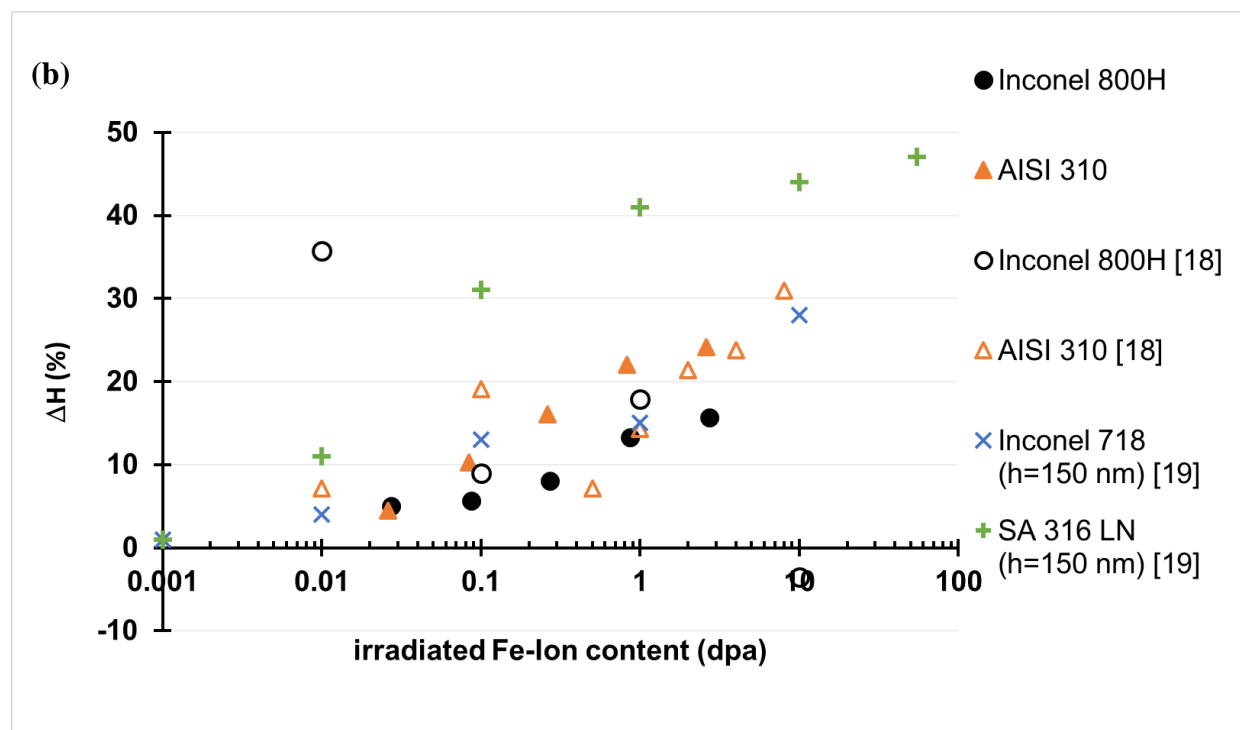


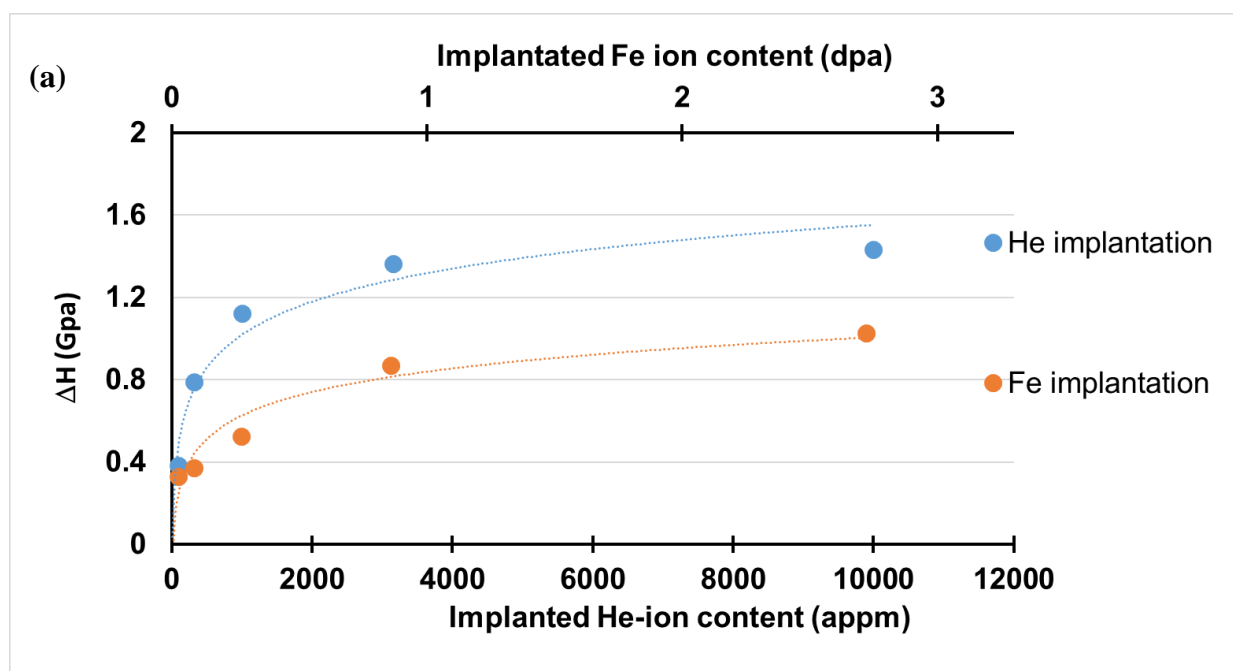
Figure 5.1 Comparison of percent hardening in Inconel 800H, AISI310, Inconel 718 and SA 316LN as a function of (a) helium concentration (b) Fe^{4+} ion irradiation

5.1.1 Effect of ion damage on the He^+ implanted samples

Helium ions are typically implanted with lower kinetic energy than heavier ions, such as Fe^{4+} . Despite this, the He^+ ion does still impart a certain amount of crystal damage (dpa) to the substrate material. Thus, to properly assess the effect of helium on ΔH we must separate its effect due to compositional changes, as indicated by the appm parameter, and due to crystal damage. The effect of implanting various appm levels of helium on the resulting dpa level of the Inconel 800H and the AISI 310 alloys was calculated using the SRIM software and is listed in Figure 3.6.

Figure 5.2 shows ΔH versus both appm helium and the resulting dpa for both alloys. Include in this figure are ΔH versus dpa from samples implanted with Fe^{4+} instead of He^+ . Both the Inconel 800H and the AISI 310 alloys have a chemical composition that is primarily iron; thus, Fe^{4+} implantation does not significantly change the composition of these alloys although it does impart significant, dpa, crystal damage. Comparison of the curves in Fig. 5.2 indicate that, for a given

implanted dpa level, the ΔH resulting from He^+ implantation is significantly higher than the ΔH resulting from Fe^{4+} implantation. This is attributed to the effect of the implanted He^+ on changing the chemical composition of the implanted alloys. As was stated in Chapter 2 (Section 2.3), previous researchers have studied this “compositional effect” and attribute it to the implanted helium forming small voids, or bubble, throughout the microstructure of the implanted material and these bubbles act as relatively stable obstacles which impede the movement of dislocations, and hence the initiation of plastic deformation. An important aspect of the research in this thesis is to quantify the thermal stability of these helium bubbles and rank it to the stability of the implantation-induced (dpa) crystal damage, and the computed activation energy of atomic self-diffusion. This is covered in the next section.



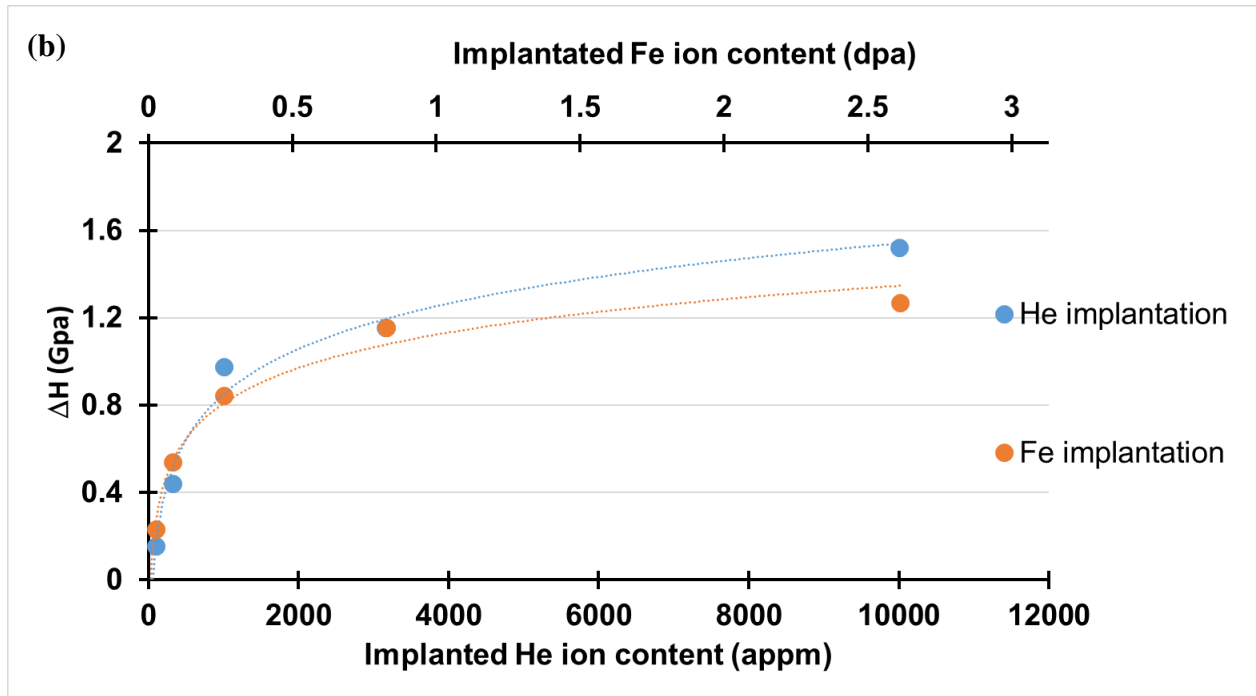


Figure 5.2 Comparison of percent hardening relative to unirradiated material for (a) Inconel 800H and the (b) AISI310 as a function of helium concentration and Fe ion irradiation

5.2 High temperature softening of ion implanted alloys

The data in Chapter 4 indicate clearly the general progressive softening of He^+ and Fe^{4+} implanted AISI310 and Inconel 800H alloys when exposed to heating at 400°C and 600°C for various lengths of time. Here, we analyse this softening process by comparing the change in hardness, ΔH , as a function of the annealing time at 400°C for samples that were implanted to equal dpa levels with either He^+ or Fe^{4+} ions (Figure 5.3 and 5.4). These figures illustrate that, for both implantation conditions, ΔH decreases with increasing annealing time. What follows is a comparison the rate of softening of the two alloys.

Figure 5.5 shows the rate, $d(\Delta H)/dt$, of the softening that occurs over the first 10 minutes exposure to 400°C. For Inconel 800H, the softening rate for the Fe^{4+} implanted sample is clearly greater than that for the He^+ implanted samples of similar dpa damage level. For both implantation conditions the magnitude of $d(\Delta H)/dt$ increased with increasing dpa damage level. This suggests, therefore, that implanted helium has the effect of decreasing the rate at which the ion-implantation crystal damage is removed by thermally activated atomic diffusion. However, for AISI 310, the soften rate, $d(\Delta H)/dt$, of the He^+ or Fe^{4+} implanted samples showed nearly identical dependence upon dpa implantation damage. The difference in softening characteristics between these two alloys is most probably associated with differences in their tendency for atomic diffusion. This is investigated in more detail next.

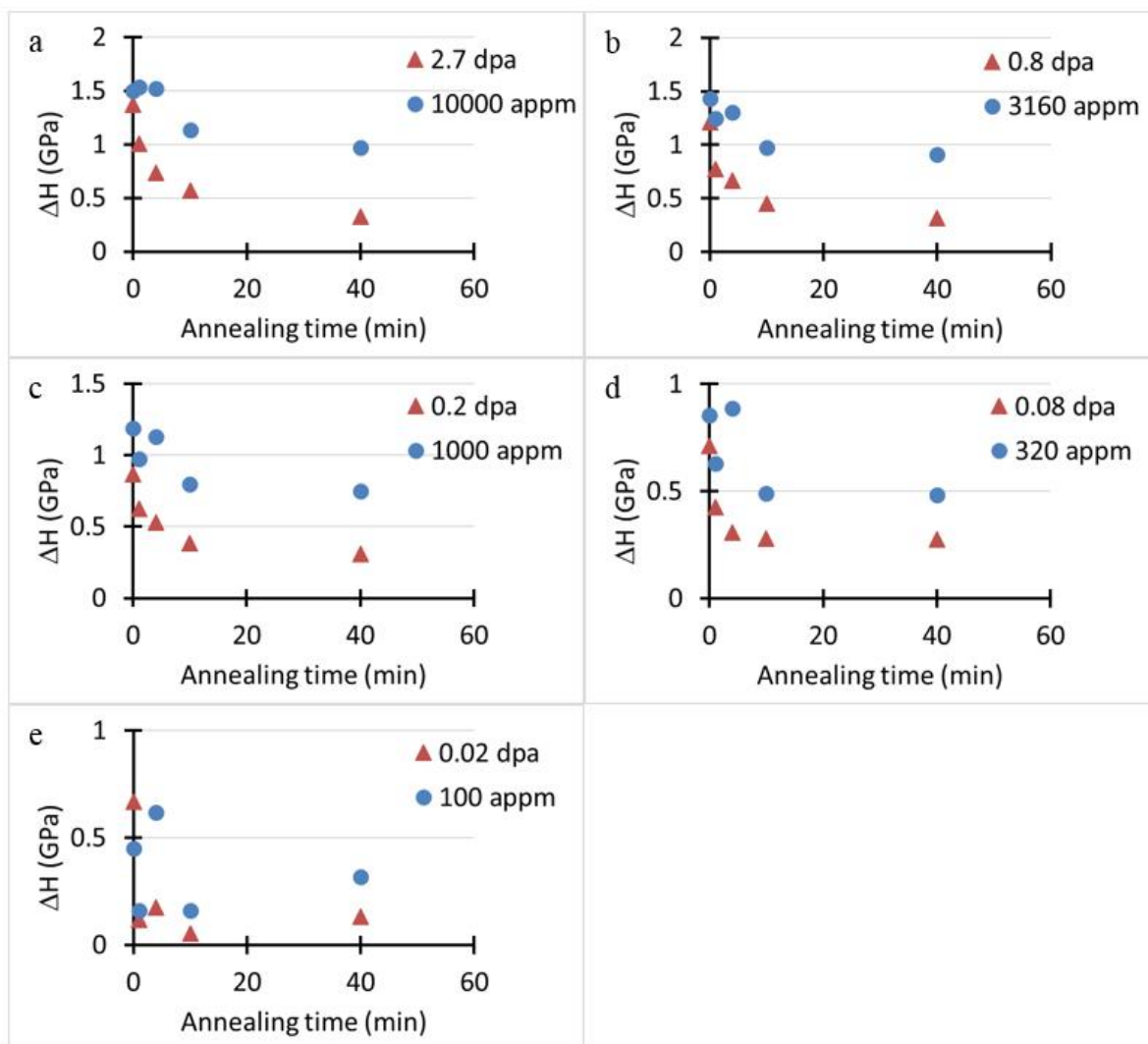


Figure 5.3 The change of hardness of Inconel 800H when exposed to different dpa levels of ion implantation damage. The dpa level of damage was achieved by Fe⁴⁺ implantation (red triangles) and He⁺ implantation (blue circles). The individual graphs show data for various dpa levels: (a) 2.7 dpa & 10000 appm (b) 0.8 dpa & 3160 appm (c) 0.2 dpa & 1000 appm (d) 0.08 dpa & 320 appm (e) 0.02 dpa & 100 appm

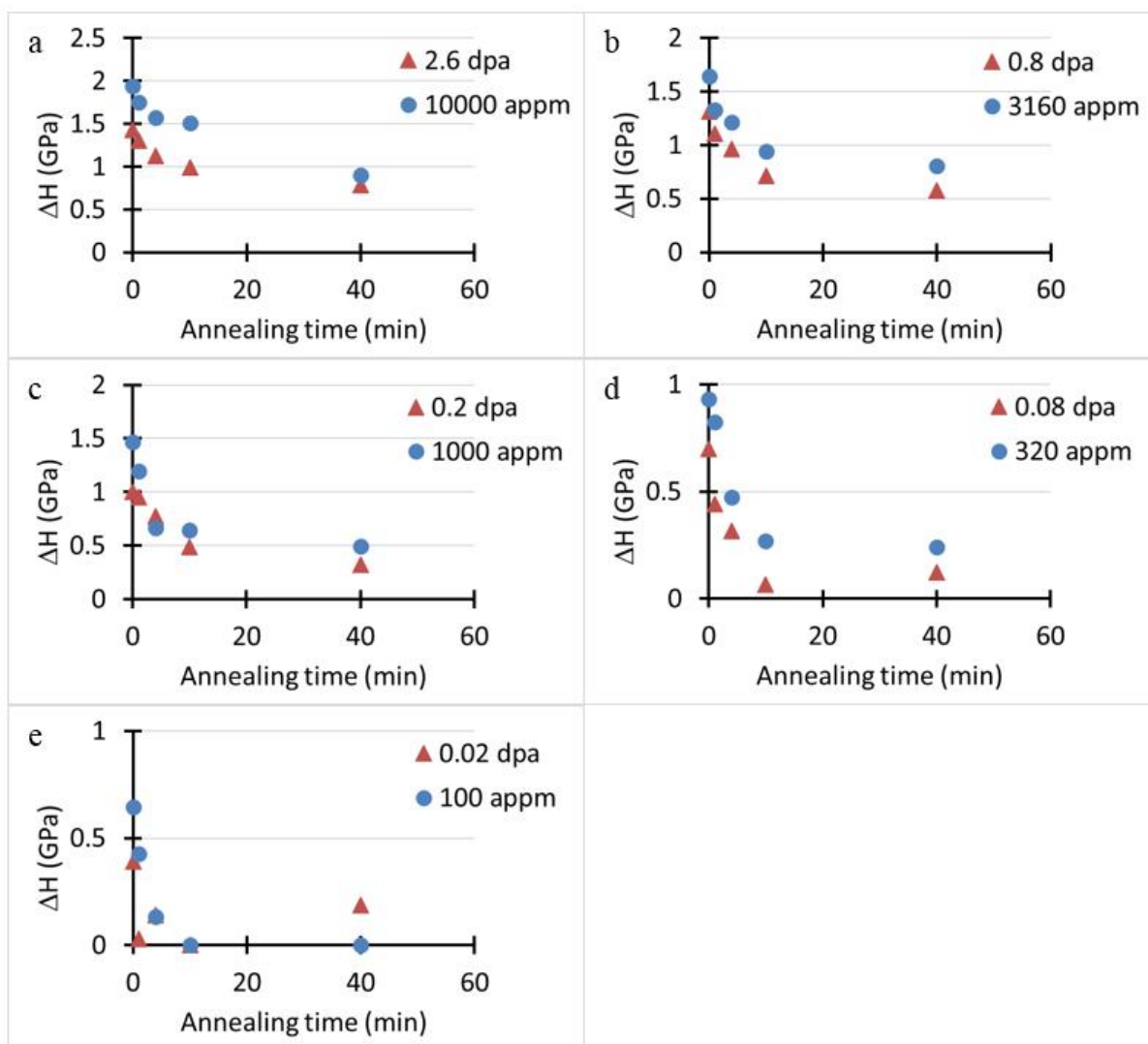


Figure 5.4 The change of hardness of AISI 310 when exposed to different dpa levels of ion implantation damage. The dpa level of damage was achieved by Fe⁴⁺ implantation (red triangles) and He⁺ implantation (blue circles). The individual graphs show data for various dpa levels: (a) 2.7 dpa & 10000 appm (b) 0.8 dpa & 3160 appm (c) 0.2 dpa & 1000 appm (d) 0.08 dpa & 320 appm (e) 0.02 dpa & 100 appm

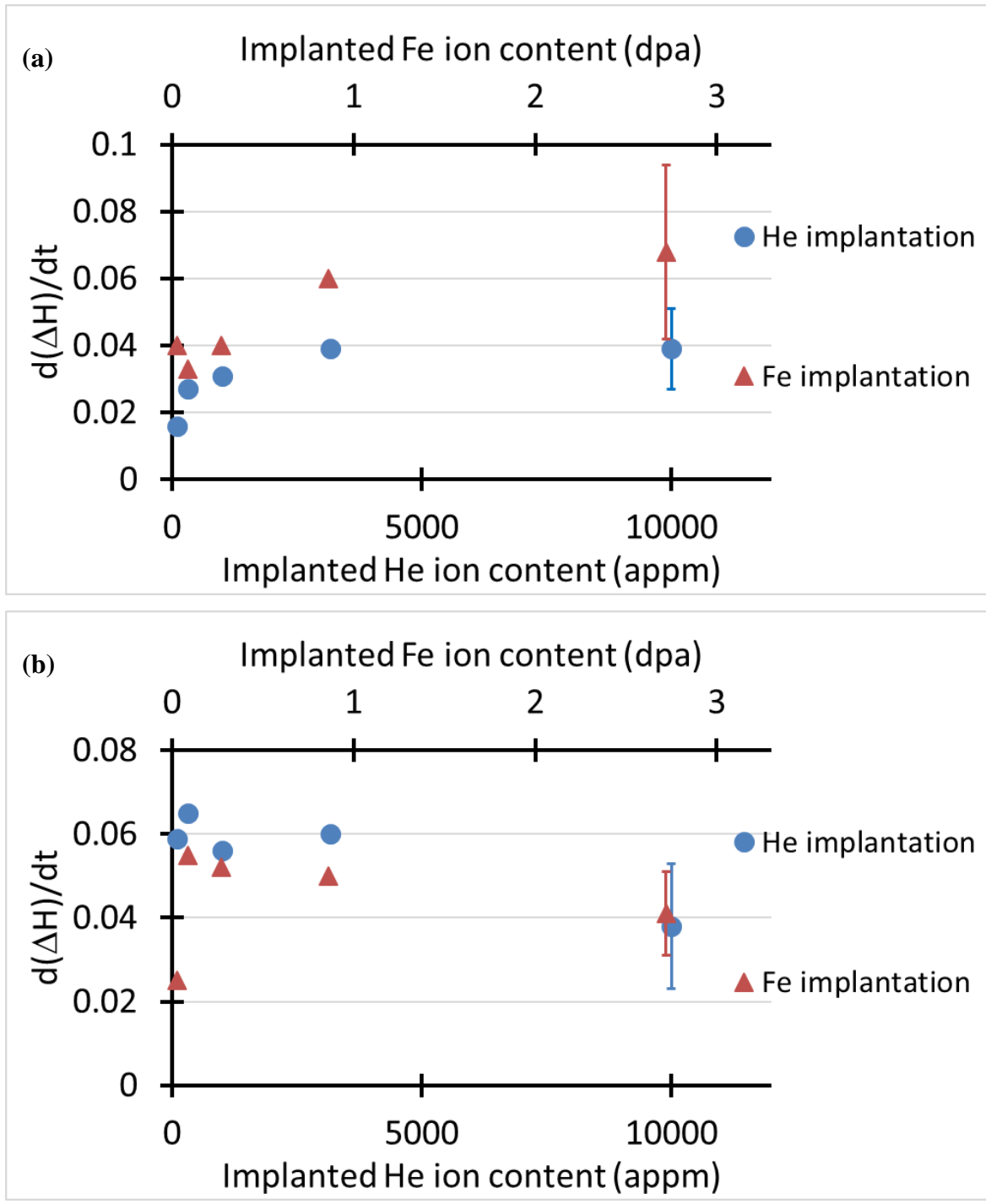


Figure 5.5 comparison of the rate, $d(\Delta H)/dt$, of the softening that occurs over the first 10 minutes exposure to 400°C of (a) Inconel 800H and (b) AISI 310

To further quantify the thermal softening process that is occurring in the He⁺ implanted Inconel 800H and AISI 310 samples we assess the rate of softening $d(\Delta H)/dt$ that occurs over the first 10 minutes of exposure to either 400°C or 600°C for samples from each alloy that were implanted with various levels of helium. Figure 5.6 shows a semi-logarithmic plot of $d(\Delta H)/dt$ versus $1/T$. From the slope of the data on this plot we were able to estimate an apparent activation energy, Q , associated with the rate of softening as is given by the following Arrhenius-type equation

$$d(\Delta H)/dt_{\Delta t=10min} = A * \exp[-(Q/kT)] \quad (1)$$

In this equation, A is a material constant, k is the Boltzmann constant (8.62×10^{-5} eV/K), and the activation energy Q is of units eV.

Table 5.1 shows the values of Q determined by calculating the slopes of the data trends shown in Figure 5.6. As shown in this table, the activation energy for the softening process is between 0.08 to 0.38 eV for the AISI 310 alloy and 0.33 to 0.44 eV for the Inconel 800H alloy

When Q is plotted against helium concentration level, Figure 5.7, we can see that, for both alloys, Q increases, in an approximately linear fashion, with increasing helium concentration. The following equations were obtained, by linear-regression curve fitting to the data in Figure 5.7, to describe this linear dependence

$$Q(C_{He})|_{AISI\ 310} = 2.81 \times 10^{-5} C_{He} + 0.11 \quad (eV) \quad (5.2)$$

$$Q(C_{He})|_{Inconel\ 800H} = 1.36 \times 10^{-5} C_{He} + 0.31 \quad (eV) \quad (5.3)$$

These equations for $Q(C_{He})$ reveal two primary differences between the thermal stability of the indentation hardness of these two alloys. Firstly, the constants, $Q_o|_{AISI\ 310} = 0.11$ eV and $Q_o|_{Inconel\ 800H} = 0.31$ eV, are of similar magnitude to previously reported values ($Q \approx 0.62$ eV) for the activation energy for surface self-diffusion of Ni at elevated temperature (800 – 1100°C) [47]. Therefore, we can conclude that the softening of our non-implanted Inconel 800H and AISI 310 alloys occurs by a mechanism that involves substantial atomic diffusion. Besides, referring back to Tables 3.1 we see that the primary chemical difference between these two alloys is the

nickel content: the AISI 310 alloy contains about 20 wt% Ni while the Inconel 800H alloy contains about 33 wt% Ni., it seems that there is more resistant for Ni atom diffusion as the Ni content in the alloy increases.

Secondly, the difference in the linear dependence of Q upon C_{He} ; namely, $3 \times 10^{-5} \text{ eV/appm}$ for AISI 310 compared to $1 \times 10^{-5} \text{ eV/appm}$ for Inconel 800H means that the effect of implanted helium atom on impeding the motion of dislocations is stronger for the AISI 310 alloy than it is for the Inconel 800H alloy.

Table 5.2 lists previous published values for the computed thermal activation energy Q_{He} for interstitial helium diffusion within pure nickel. One can see that the values for Q_{He} are of very similar magnitude as the values of Q obtained in this study. From this similarity we conclude that the relaxation of indentation hardness in these He-implanted AISI 310 and Inconel 800H samples occurs primarily by the diffusion of helium within the deformation zone around the indentations. In addition, Comparing the Q value for the two alloys with the trends of $d(\Delta H)/dt$ versus helium content (Figure 5.5), the softening rate for the Fe^{4+} implanted Inconel 800H (higher Ni content alloy) was significantly greater than the softening rate for its He^+ implanted counterpart while no difference was observed between the softening rates of the Fe^{4+} and the He^+ implanted AISI 310 (lower Ni content) alloy. The data presented above all support the conclusion that Ni atoms impedes the rate of diffusion of Helium through these alloys.

In summary, in this section we assessed the dependence of the thermal activation energy for the recovery of indentation hardness of the AISI 310 and Inconel 800H alloys and correlated with the chemical composition, i.e. the nickel content, of the alloys and the implanted helium concentration. From this analysis we proposed that the mechanism controlling the softening rate in these alloys was a diffusion process where the implanted helium significantly increased the required activation energy. What we present next is an assessment of the effect of implanted helium on the strain rate sensitivity of the indentation hardness of these two alloys. This assessment will provide more information of the effectiveness of the implanted helium as an obstacle to plastic deformation.

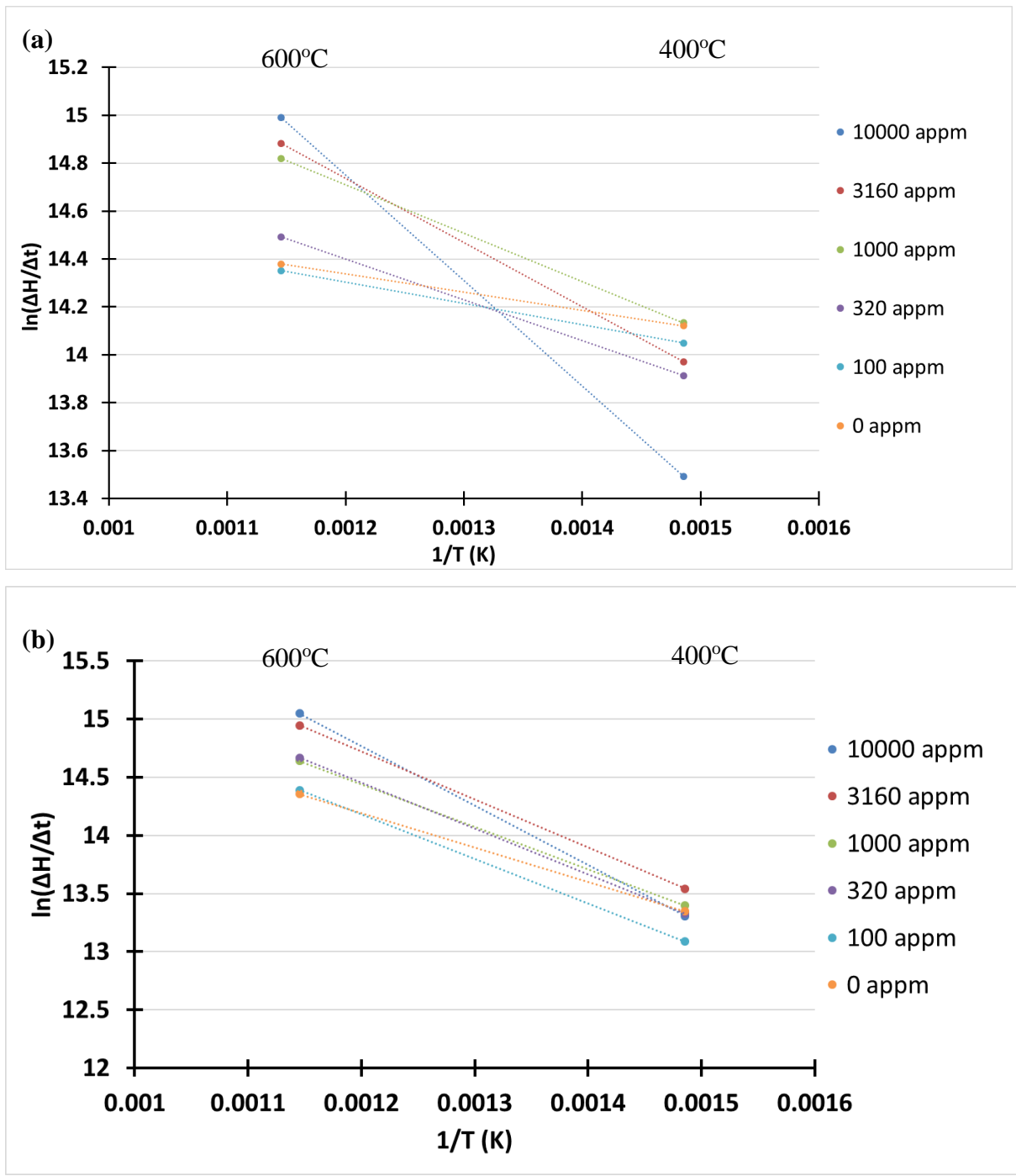


Figure 5.6 The change of indentation hardness with time, over a 10-minute period, at temperature of 400°C and 600°C for the (a) AISI 310 and the (b) Inconel 800H alloys

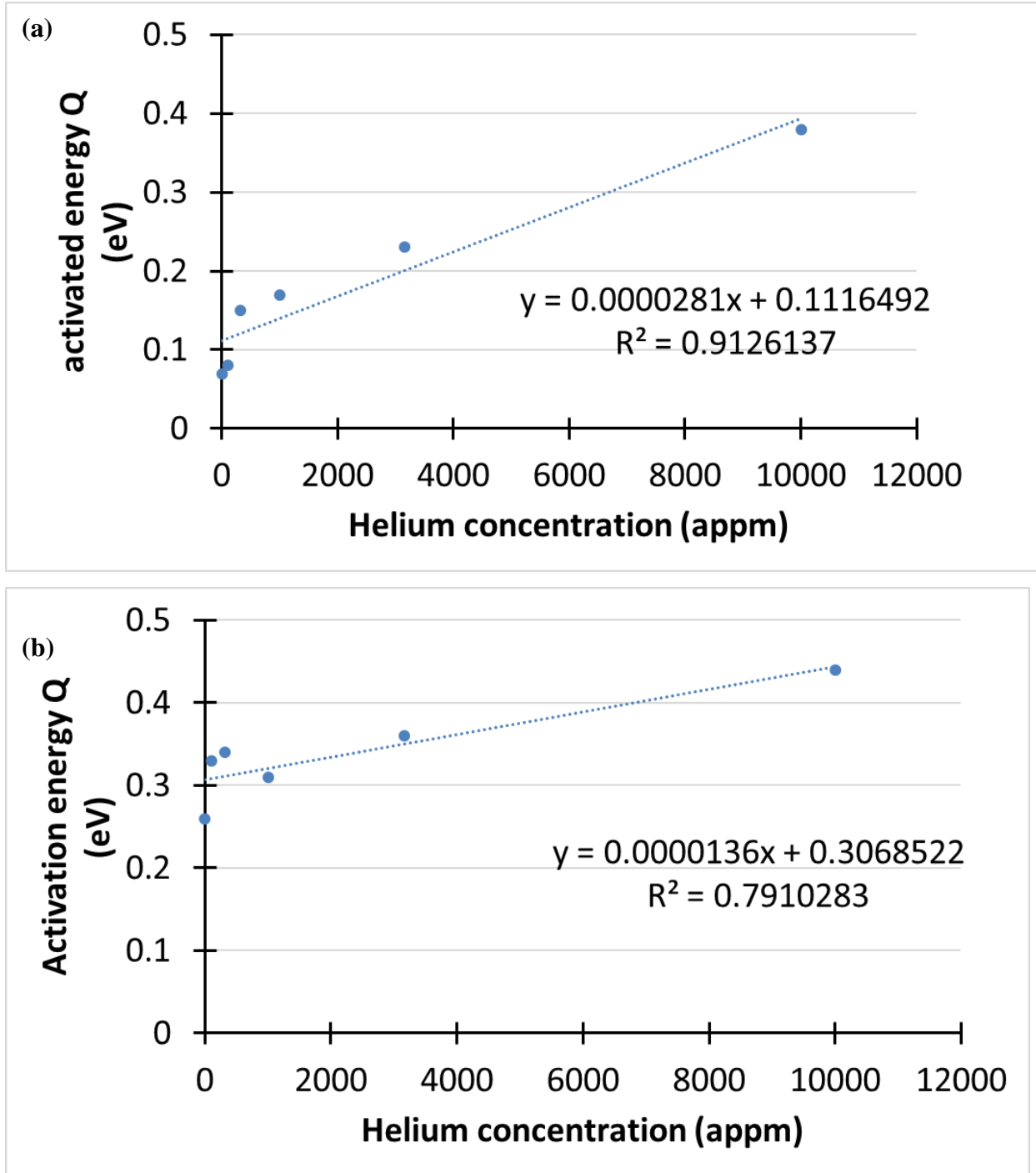


Figure 5.7 Activation energy Q describing the rate of softening as a function of the implanted helium concentration for the (a) AISI 310 and (b) Inconel 800H alloys

Table 5.1 Activation energy of the thermal recovery of indentation hardness in the AISI 310 and Inconel 800H alloys implanted with various levels of helium

C_{He} (appm)	10000	3160	1000	320	100	0
Q (eV)						
AISI 310	0.38	0.23	0.17	0.15	0.08	0.07
Inconel 800H	0.44	0.36	0.31	0.34	0.33	0.26

Table 5.2 Measured activation energies for the thermal recovery of indentation hardness (from Table 5.1) listed along with calculated activation energies for the interstitial diffusion of helium within crystalline nickel

Measured activation energy (eV)	Diffusion temperature	Reference	Proposed diffusion mechanism
0.14	80K	[48]	Helium interstitial diffusion
0.11	80-300K	[49]
0.35	100-300K	[50]
0.81	1100-1500K	[51]	Irradiation-enhanced helium diffusion
0.08 – 0.38	673-873K	This Study	Helium interstitial diffusion
0.33 – 0.44		- Hardness recovery.	

5.3 Strain rate sensitivity of the indentation hardness

In this study we performed nano-indentation hardness measurements, at indentation depths of about 200 nm, at four different average indentation strain rates, $\dot{\epsilon}_{indent} = 0.05, 0.25, 0.5$ and 1.0 sec^{-1} for the non implanted and the He^+ implanted samples of AISI 310 and Inconel 800H in two conditions: before- and after- annealing for 10 minutes at 400°C . The

magnitude of the strain rate sensitivity m , Equation (2.3), allows us to assess the apparent activation volume V^* which characterises the strength of the obstacles within the microstructure that are impeding the motion of dislocations and thus affecting the yield stress. Since the indentation hardness H is directly proportional to the equivalent yield stress, often referred to as the equivalent flow stress, of a metal as

$$H \approx 3\sigma \quad (5.4)$$

we can use our hardness data to assess the strain rate sensitivity parameter m by plotting H versus $\dot{\epsilon}_{indent}$ on a logarithmic scale, the slope of which is m . Then, the apparent activation volume V^* is expressed by rewriting Equation 2.4 as

$$V^* = \frac{3\sqrt{3}kT}{Hm} \quad (5.5)$$

Values of apparent activation volume are typically expressed in units of cubic Burgers vector (b^3), where b for nickel is ~ 0.249 nm and for γ iron is ~ 0.258 nm [52]. Tables 5.3 and 5.4 show values of m and V^* for the AISI 310 and Inconel 800H alloys implanted with different helium content before- and after-annealing at 400°C for 10 minutes.

Table 5.3 The m and V^* and of Inconel 800H

	C_{HE} (APPM)	10000	3160	1000	320	100	0
No annealing	m	0.0249	0.0304	0.0306	0.0335	0.04	0.0452
	V^* (b^3)	90.54	74.12	77.2	71.5	61.83	60.66
Annealing at 400°C 10 min	m	0.0129	0.0179	0.0323	0.0243	0.0228	0.0302
	V^* (b^3)	174.99	132.3	73.49	101.67	108.81	90.59

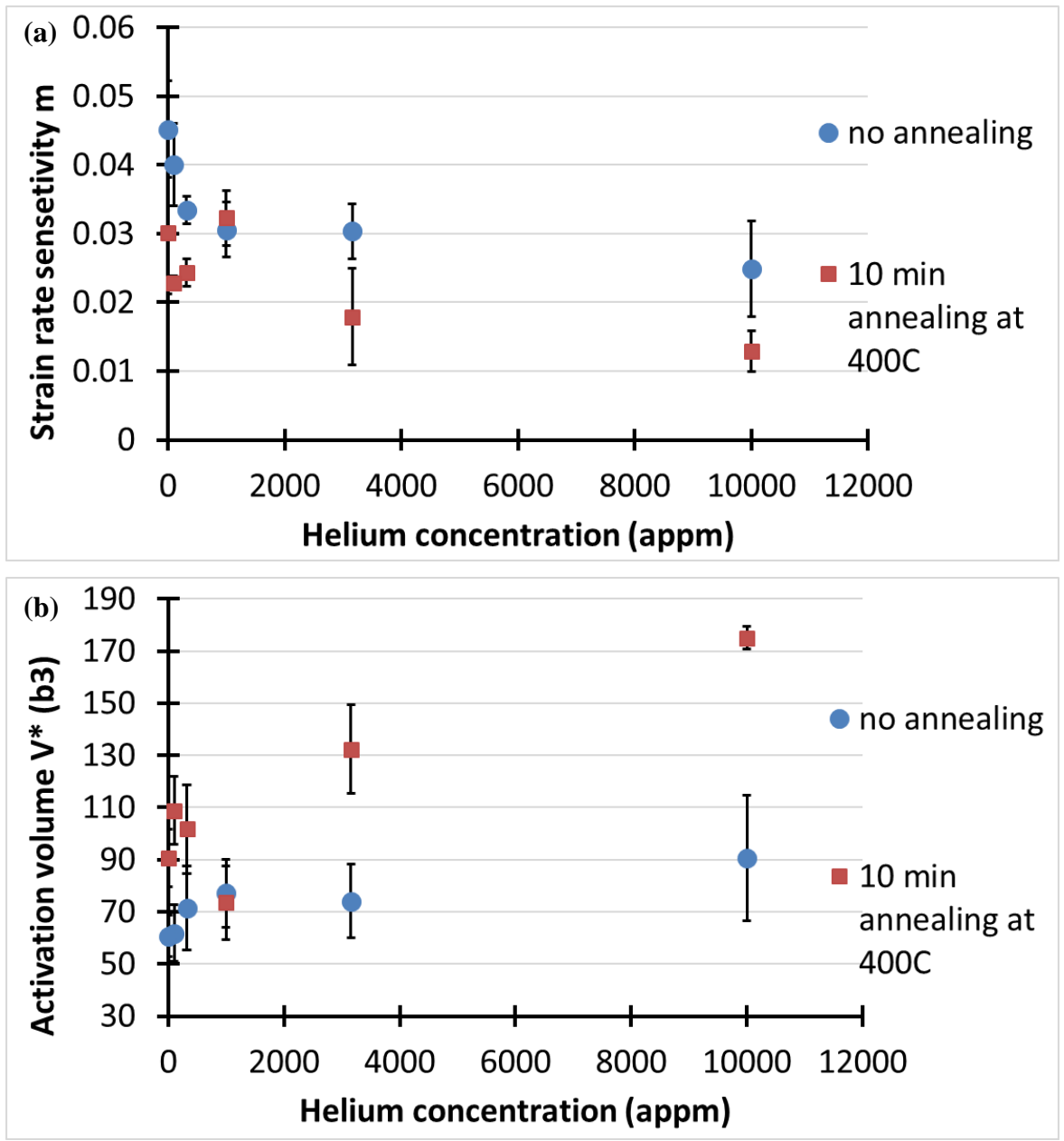
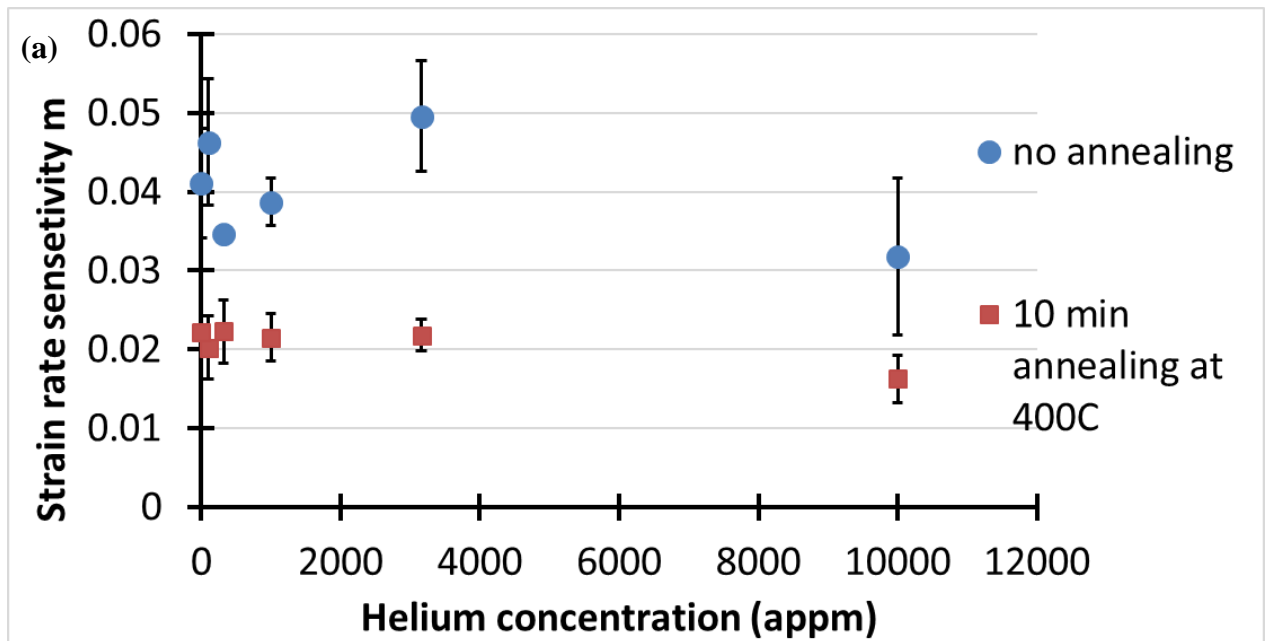


Figure 5.8 Comparison of the m and V^* of Inconel 800H before- and after- annealing at 400°C for 10 min

Table 5.4 the m and V^* of AISI 310

	C_{HE} (APPM)	10000	3160	1000	320	100	0
No annealing	m	0.0318	0.0496	0.0387	0.0347	0.0463	0.0411
	$V^*(b^3)$	72.01	49.34	64.05	74.7	58.75	72.5
Annealing at 400°C 10 min	m	0.0163	0.0218	0.0215	0.0223	0.0202	0.0222
	$V^*(b^3)$	145.98	113.09	122.17	124.49	140.66	127.89



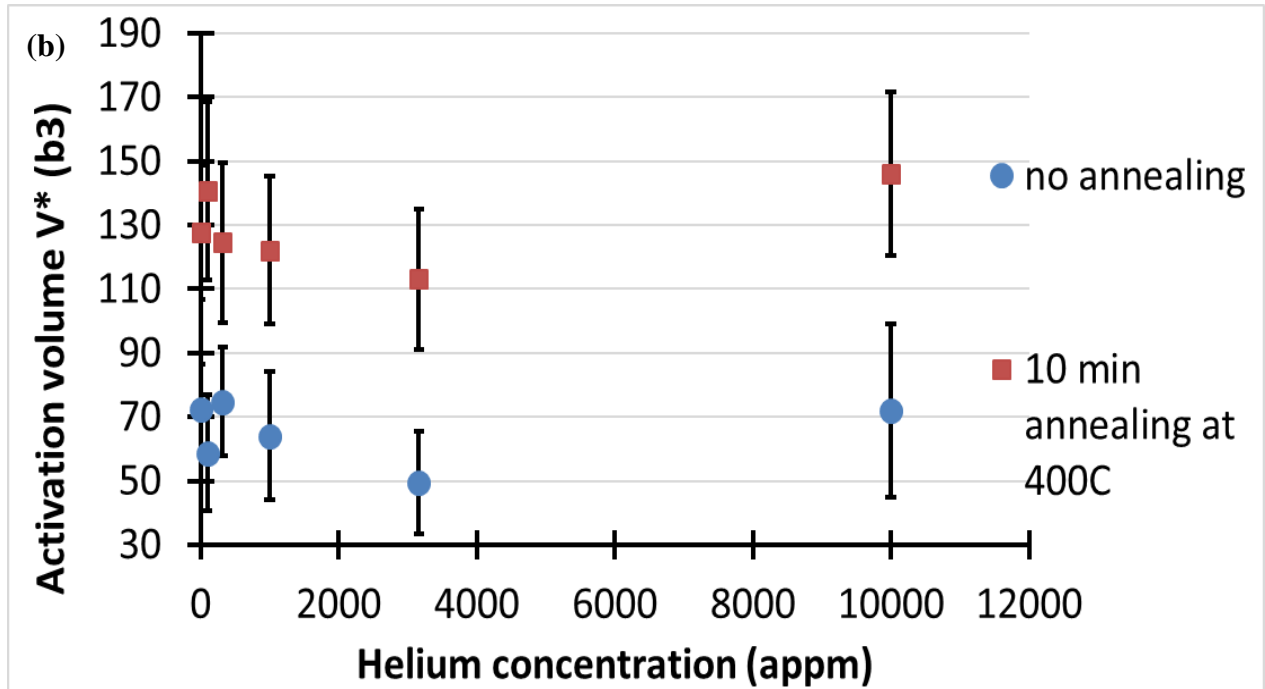


Figure 5.9 Comparison of the m and V^* of AISI 310 before- and after- annealing at 400°C for 10 min

For both AISI 310 and Inconel 800H, m decreases, and V^* increases, significantly after annealing (Figures 5.8 and 5.9). In both alloys, the 400°C heat treatment provides energy for helium diffusion. The helium atoms may diffuse to the grain boundary or form helium micro-bubbles within the alloy. In either case the regions where the helium accumulates acts as an obstacle to impede the motion of dislocations therefore causing V^* to increase with both increasing C_{He} and with annealing at 400°C.

In the non-implanted alloys the measure m value is between $m = 0.02$ and 0.05 . This is larger in magnitude than previously published values of m ($m \approx 0.006$) obtained from large-scale uniaxial tensile tests performed on coarse grain nickel material [52][53]. This difference probably arises from the fact that the strain rate sensitivity values in this study were obtained from nanoindentation hardness tests ($h \approx 200\text{nm}$). Previous research has reported that strain rate sensitivity parameters, such as m , show clear indentation depth dependence, and increase in magnitude, when $h \leq 1.0 \mu\text{m}$ [54].

It is instructive to compare our m and V^* values with those reported for similar nanoindentation tests performed on a bulk nickel alloy (Alloy 690) and nanocrystalline nickel samples (Table 5.5). Compared with these published results we find that the the m and V^* values obtained in our present research are quantitatively similar to these previously published values. It is interesting to note that m and V^* increased with decreasing grain size in a manner that is qualitatively similar to the increase that we observed with increasing implanted helium content. This is particularly evident for our higher Nickel content alloy Inconel 800H. This similarity in trends further supports our observation that the implanted helium acts as an effective obstacle to dislocation glide and that post-implantation annealing results in the diffusion of, and agglomeration of, the helium into higher strength obstacles either as grain boundary segregants or helium microvoids within the grains.

Table 5.5 Comparison of this work to the research before

material	m	V^*	Reference
800H	0.02-0.05	$60b^3-90b^3$	This work
800H-annealed	0.01-0.04	$90b^3-175b^3$	
AISI310	0.03-0.04	$50b^3-75b^3$	
AISI310-annealed	0.016-0.022	$113b^3-145b^3$	
Alloy 690	0.006	$54b^3-94b^3$	[52]
Nanocrystalline Ni	0.019	$14b^3$	[39]
Nanocrystalline Ni	0.033	$7b^3$	[55]

5.4 Testing issues and their effects

In this study, the samples typically display some amount of surface discolouration after exposure to elevated temperature (See figures in Section 4.2). The amount of discolouration increased with

annealing temperature and time. These observations show that the surface of the samples are becoming oxidized during the annealing treatments. The presence of an oxide layer on the samples affects the measured indentation hardness as shown by the italicized data in Figure 4.4: When the annealing temperature is 600°C, and the annealing time is 40 min, the measured indentation hardness is increased. We attribute this to the presence of an oxide layer.

Chapter 6

6 Conclusion, Contribution and Future Works

6.1 Conclusion and Contribution

Inconel 800H and AISI 310 are candidate materials for in-core components of the Canadian proposed Gen-IV Supercritical Water Cooled nuclear Reactor (SCWR) concept. These components will be exposed to severe conditions of high temperature and neutron irradiation above the levels for which experimental data currently exist. The elevated nickel content of these alloys results in considerable accumulation of helium during service as a result of alpha-decay nuclear transmutation processes. While accumulated helium is known to harden and embrittle metal alloys, the effect of exposure to high temperature on this phenomenon is still unstudied.

The objective of this study is to assess the extent to which irradiation- and helium-induced hardening will accumulate significantly in components made of these alloys when they are exposed to these high temperature conditions in the Canadian Gen. IV SCWR core.

The polished and unetched, Inconel 800H and AISI 310 samples, were exposed to various levels of He^+ and Fe^{4+} ion implantation, which were 0, 100, 320, 1000, 3160, 10000 appm and 0, 0.03, 0.08, 0.26, 0.83, 2.6 dpa. The He^+ implanted samples were then annealed at 400°C and 600°C, and Fe^{4+} implanted samples were annealed at only 400°C, for 1 to 40 minutes of duration to measure the effect of thermal recovery on the indentation hardness.

The effect of implanted helium on the operative mechanisms of plastic deformation was further studied by measuring indentation hardness at various indentation strain rates, between 0.05 and 1.0 sec^{-1} , before- and after- annealing at 400°C for 10 minute.

The indentation hardness results showed that , the hardness of He^+ implanted samples increased by 34% and 27%, and the hardness of Fe^{4+} implanted samples increased by 24% and 15% , compared to the unimplanted AISI 310 and Inconel 800H samples respectively. For the same

amount of displacement damages, the hardness change resulting from He^+ implantation is significantly higher than the hardness change resulting from Fe^{4+} implantation.

Both of the He^+ and Fe^{4+} implanted Inconel 800H and AISI 310 alloys, when exposed to heating at 400°C and 600°C for 40 minutes, the hardness decreased significantly at the beginning of the annealing process and ΔH decreased with increasing annealing time. Besides, for Inconel 800H, the softening rate, $d(\Delta H)/dt$, for the Fe^{4+} implanted sample is clearly greater than that for the He^+ implanted samples of similar dpa damage level. However, for AISI 310, the soften rate, $d(\Delta H)/dt$, of the He^+ or Fe^{4+} implanted samples showed nearly identical dependence upon dpa implantation damage. This suggests Ni can slow the helium diffusion.

Thermal activation energy characterizing the annealing process was measured for both alloys. The activation energy Q of the hardness recovery process is between 0.08 and 0.38 eV for the AISI 310 and between 0.33 and 0.44 eV for the Inconel 800H alloy. The magnitude of Q was similar to the computed thermal activation energy Q_{He} for interstitial helium diffusion within pure nickel. So we conclude that the relaxation of indentation hardness in these He-implanted AISI 310 and Inconel 800H samples occurs primarily by the diffusion of helium within the deformation zone around the indentations. This is one of the most important findings in this research and the calculated He diffusion energy can be contributed to the simulation and emulation of helium diffusion analysis.

For both alloys, Q increases, in an approximately linear fashion, with increasing helium concentration. Equations were developed to describe this relationship were shown in equation 5.2 and 5.3. we can conclude that (1) the softening of our non-implanted Inconel 800H and AISI 310 alloys occurs by a mechanism that involves substantial atomic diffusion and there is more resistant for Ni atom diffusion as the Ni content in the alloy increases. (2) the effect of implanted helium atom on impeding the motion of dislocations is stronger for the AISI 310 alloy than it is for the Inconel 800H alloy.

Last but not the least, another important finding is from the assessment of the effect of implanted helium on the strain rate sensitivity of the indentation hardness of these two alloys. It was observed that, for both AISI 310 and Inconel 800H, the strain rate sensitivity m decreases, and activation volume V^* increases, significantly after annealing. This suggests that the He defects

(voids or bubbles) within the metal become more stable with annealing, as they tend to form bigger bubbles in the grain boundaries. This finding suggests the nuclear industry pay attention to the importance of helium problems. Once helium goes into the material, it is hard to get rid of them.

These findings have important implications for assessing the suitability of the Inconel 800H and AISI 310 alloys for use as in-core components of a Gen-IV supercritical water cooled nuclear reactor.

6.2 Future Work

The findings of this thesis suggest some future work for further understanding the problem of helium accumulation and embrittlement within Ni-bearing metal components in nuclear reactors.

First, TEM analysis could be conducted on non-implanted and He-implanted samples which have been exposed to different post-implantation annealing time. This work may indicate how the size and quantity of He bubbles/cavities depends upon He-implantation levels and annealing time. Such research would provide additional information against which to assess the conclusions that have been reached in this thesis.

Although the coolant temperature of the Canadian concept GEN IV SCWR core is from 300 to 600°C, some parts of the core may reach 800°C. it is reasonable that post He-implantation thermal annealing be performed at 800°C, and even 1000°C, in vacuum to record the hardness change. In this way, we can further understand the characteristics of He defect diffusion.

Finally, He implantation at high temperature, rather than at 25°C, may result in a He distribution within the test material that is more representative of that found in in-core Ni-bearing components.

Reference

- [1] “CANDU.” [Online]. Available: <http://www.candu.com/en/home/aboutcandu/default.aspx>. [Accessed: 07-Mar-2017].
- [2] R. B. Duffey and L. K. H. Leung, “Advanced cycle efficiency: generating 40% more power from the nuclear fuel,” in *World Energy Congress (WEC)*, 2010, no. 2, pp. 12–16.
- [3] J. R. Lamarsh and A. J. Baratta, *Introduction to nuclear engineering*. Prentice hall, 2001.
- [4] C. D. Judge, N. Gauquelin, L. Walters, M. Wright, J. I. Cole, J. Madden, G. A. Botton, and M. Griffiths, “Intergranular fracture in irradiated Inconel X-750 containing very high concentrations of helium and hydrogen,” *Journal of Nuclear Materials*, vol. 457, no. February 2016, pp. 165–172, 2015.
- [5] C. D. Judge, “The Effects of Irradiation on Inconel X-750,” no. September, p. 226, 2015.
- [6] C. D. Judge, M. Griffiths, L. Walters, M. Wright, G. A. Bickel, O. T. Woo, M. Stewart, S. R. Douglas, and F. A. Garner, “Embrittlement of nickel alloys in a CANDU reactor environment,” *25th Int. Symposium on Radiation Effects in Materials*, vol. 1547, pp. 161–175, 2013.
- [7] M. Griffiths, “The Effect of Irradiation on Ni-containing Components in CANDU Reactor Cores: A Review,” *AECL Nuclear Review*, vol. 2, no. 1, pp. 1–16, 2013.
- [8] L. R. Greenwood and A. Garner, “Hydrogen generation arising from the $^{59}\text{Ni} (n, p)$ reaction and its impact on fission-fusion correlations,” *Journal of Nuclear Materials*, vol. 237, pp. 1530–1534, 1996.
- [9] D. F. Wang and S. Wang, “ARTICLE a preliminary cathena thermalhydraulic model of the canadian scwr for safety analysis,” pp. 9–16, 2014.
- [10] D. F. Torgerson, B. A. Shalaby, and S. Pang, “CANDU technology for Generation III+ and IV reactors,” *Nuclear Engineering and Design*, vol. 236, no. 14–16, pp. 1565–1572,

2006.

- [11] S. Baidur, “Materials challenges for the supercritical water cooled reactor (SCWR),” *Canadian Nuclear Society*, vol. 29, no. 1, pp. 32–38, 2008.
- [12] “supercritical water.” [Online]. Available: http://www1.lsbu.ac.uk/water/supercritical_water.html. [Accessed: 07-Mar-2017].
- [13] T. Abram and S. Ion, “Generation-IV nuclear power: A review of the state of the science,” *Energy Policy*, vol. 36, no. 12, pp. 4323–4330, 2008.
- [14] “Supercritical-Water-Cooled Reactor (SCWR).” [Online]. Available: https://www.gen-4.org/gif/jcms/c_40679/technology-system-scwr. [Accessed: 08-Mar-2017].
- [15] R. G. Sanchez, “Corrosion Performance of Candidate Materials for Canadian Gen IV Supercritical Water Cooled Reactor,” 2014.
- [16] C. K. Chow and H. F. Khartabil, “Conceptual Fuel Channel Designs for Candu – Scwr,” vol. 40, no. 2, 2007.
- [17] D. J. Edwards, F. A. Garner, S. M. Bruemmer, and P. Efsing, “Nano-cavities observed in a 316SS PWR flux thimble tube irradiated to 33 and 70 dpa,” *Journal of Nuclear Materials*, vol. 384, no. 3, pp. 249–255, 2009.
- [18] Z. Pan, S. S. Lawrence, P. Davies, M. Griffiths, and S. Sagat, “Effect of Irradiation on the Fracture Properties of Zr-2 . 5Nb Pressure Tubes at the End of Design Life,” vol. 2, no. 9, pp. 1–22, 2011.
- [19] B. Bose, “Bipasha Bose Assessment of the Kinetics of Local Plastic Deformation of Zr-2 . 5 % Nb CANDU Pressure Tube Material,” UWO, 2012.
- [20] C. Heintze, C. Recknagel, F. Bergner, M. Hernández-mayoral, and A. Kolitsch, “Nuclear Instruments and Methods in Physics Research B Ion-irradiation-induced damage of steels characterized by means of nanoindentation,” *Nuclear Inst. and Methods in Physics Research, B*, vol. 267, no. 8–9, pp. 1505–1508, 2009.

- [21] H. Rajakumar, "Thermal kinetics of ion irradiation hardening in selected alloys for the Canadian Gen . IV nuclear reactor concept," no. August, 2015.
- [22] J. D. Hunn, E. H. Lee, T. S. Byun, and L. K. Mansur, "Helium and hydrogen induced hardening in 316LN stainless steel," *Journal of Nuclear Materials*, vol. 282, no. 2–3, pp. 131–136, 2000.
- [23] E. V. Kornelsen and A. A. Van Gorkum, "Study of Bubble Nucleation in Tungsten Using Thermal Desorption Spectrometry: Clusters of 2 To 100 Helium Atoms.," *Journal of Nuclear Materials*, vol. 92, no. 1, pp. 79–88, 1980.
- [24] Q. Guo, P. Landau, P. Hosemann, Y. Wang, and J. R. Greer, "Helium implantation effects on the compressive response of Cu nanopillars," *Small*, vol. 9, no. 5, pp. 691–696, 2013.
- [25] M. J. Demkowicz, P. Bellon, and B. D. Wirth, "Atomic-scale design of radiation-tolerant nanocomposites," *MRS Bulletin*, vol. 35, no. 12, pp. 992–998, 2010.
- [26] N. Li, J. J. Carter, a. Misra, L. Shao, H. Wang, and X. Zhang, "The influence of interfaces on the formation of bubbles in He-ion-irradiated Cu/Mo nanolayers," *Philosophical Magazine Letters*, vol. 91, no. 1, pp. 18–28, 2011.
- [27] N. Li, M. Nastasi, and A. Misra, "Defect structures and hardening mechanisms in high dose helium ion implanted Cu and Cu/Nb multilayer thin films," *International Journal of Plasticity*, vol. 32–33, pp. 1–16, 2012.
- [28] J. A. Knapp, D. M. Follstaedt, and S. M. Myers, "Hardening by bubbles in He-implanted Ni," *Journal of Applied Physics*, vol. 103, no. 1, 2008.
- [29] R. O. Scattergood and D. J. Bacon, "The strengthening effect of voids," *Acta Metallurgica*, vol. 30, no. 8, pp. 1665–1677, 1982.
- [30] J. D. Hunn, E. H. Lee, T. S. Byun, and L. K. Mansur, "Ion-irradiation-induced hardening in Inconel 718," *Journal of Nuclear Materials*, vol. 296, no. 1–3, pp. 203–209, 2001.
- [31] E. H. Lee, J. D. Hunn, T. S. Byun, and L. K. Mansur, "Effects of helium on radiation-

- induced defect microstructure in austenitic stainless steel,” *Journal of Nuclear Materials*, vol. 280, no. 1, pp. 18–24, 2000.
- [32] H. Trinkaus and B. N. Singh, “Helium accumulation in metals during irradiation - Where do we stand?,” *Journal of Nuclear Materials*, vol. 323, no. 2–3, pp. 229–242, 2003.
- [33] C. C. Fu and F. Willaime, “Ab initio study of helium in α -Fe: Dissolution, migration, and clustering with vacancies,” *Physical Review B - Condensed Matter and Materials Physics*, vol. 72, no. 6, pp. 1–6, 2005.
- [34] M. J. Caturla, C. J. Ortiz, and C. C. Fu, “Helium and point defect accumulation: (ii) kinetic modelling,” *Comptes Rendus Physique*, vol. 9, no. 3–4, pp. 401–408, 2008.
- [35] C. J. Ortiz, M. J. Caturla, C. C. Fu, and F. Willaime, “He diffusion in irradiated α -Fe: An ab-initio-based rate theory model,” *Physical Review B - Condensed Matter and Materials Physics*, vol. 75, no. 10, pp. 1–4, 2007.
- [36] D. R. Askeland and P. P. Phulé, *The science and engineering of materials*. 2003.
- [37] R. Abbaschian and R. E. Reed-Hill, *Physical metallurgy principles*. Cengage Learning. 2008.
- [38] J. Chen, L. Lu, and K. Lu, “Hardness and strain rate sensitivity of nanocrystalline Cu,” *Scripta Materialia*, vol. 54, no. 11, pp. 1913–1918, 2006.
- [39] V. Maier, K. Durst, J. Mueller, B. Backes, H. Höppel, and M. Göken, “Nanoindentation strain-rate jump tests for determining the local strain-rate sensitivity in nanocrystalline Ni and ultrafine-grained Al,” *Journal of Materials Research*, vol. 26, no. 11, pp. 1421–1430, 2011.
- [40] H. Vehoff, D. Lemaire, K. Schöler, T. Waschkes, and B. Yang, “The effect of grain size on strain rate sensitivity and activation volume—from nano to ufg nickel,” *International journal of materials research*, vol. 98, no. no.4, pp. 259–268, 2007.
- [41] Q. Wei, “Strain rate effects in the ultrafine grain and nanocrystalline regimes-influence on

- some constitutive responses,” *Journal of Materials Science*, vol. 42, no. 5, pp. 1709–1727, 2007.
- [42] “Rolled Alloys Canada, 800H/AT,” *Rolled Alloys Canada*, 2015. [Online]. Available: <http://www.rolledalloys.ca/alloys/nickel-alloys/800h-at/en/>. [Accessed: 11-Mar-2017].
- [43] “Rolled Alloys Canada, 310,” *Rolled Alloys Canada*, 2015. [Online]. Available: <http://www.rolledalloys.ca/alloys/stainless-steels/310/en/>. [Accessed: 11-Mar-2017].
- [44] J. F. Ziegler, M. D. Ziegler, and J. P. Biersack, “SRIM - The stopping and range of ions in matter (2010),” *Nuclear Instruments and Methods in Physics Research, Section B: Beam Interactions with Materials and Atoms*, vol. 268, no. 11–12, pp. 1818–1823, 2010.
- [45] R. E. Stoller, M. B. Toloczko, G. S. Was, A. G. Certain, S. Dwaraknath, and F. A. Garner, “On the use of SRIM for computing radiation damage exposure,” *Nuclear Instruments and Methods in Physics Research, Section B: Beam Interactions with Materials and Atoms*, vol. 310, pp. 75–80, 2013.
- [46] W. D. Nix and H. J. Gao, “Indentation size effects in crystalline materials: A law for strain gradient plasticity,” *Journal of the Mechanics and Physics of Solids*, vol. 46, no. 3, pp. 411–425, 1998.
- [47] J. M. BLAKELY and H. Mykura, “Surface self diffusion measurements on nickel by the mass transfer method,” *Acta Metallurgica*, vol. 9, no. 1, pp. 23–31, 1961.
- [48] V. Philipps and K. Sonnenberg, “Interstitial diffusion of He in nickel,” *Journal of Nuclear Materials*, vol. 114, no. 1, pp. 95–97, 1983.
- [49] D. B. Poker and J. M. Williams, “Low-temperature release of ion-implanted helium from nickel Low-temperature release of ion-implanted helium from nickel,” vol. 851, 1982.
- [50] G. J. Thomas, W. A. Swansiger, and M. I. Baskes, “Low-temperature helium release in nickel,” *Journal of Applied Physics*, vol. 50, no. 11, pp. 6942–6947, 1979.
- [51] V. Philipps, K. Sonnenberg, and J. M. Williams, “Diffusion of helium in nickel,” *Journal*

- of Nuclear Materials*, vol. 107, no. 2–3, pp. 271–279, 1982.
- [52] Y. Zhao, I. C. Choi, Y. J. Kim, and J. Il Jang, “On the nanomechanical characteristics of thermally-treated alloy 690: Grain boundaries versus grain interior,” *Journal of Alloys and Compounds*, vol. 582, pp. 141–145, 2014.
- [53] F. Dalla Torre, H. Van Swygenhoven, and M. Victoria, “Nanocrystalline electrodeposited Ni: Microstructure and tensile properties,” *Acta Materialia*, vol. 50, no. 15, pp. 3957–3970, 2002.
- [54] M. Haghshenas, “Micro-mechanical assesment of the local plastic strain invoked during a splined mandrel flow forming operation,” 2013.
- [55] C. D. Gu, J. S. Lian, Q. Jiang, and W. T. Zheng, “Experimental and modelling investigations on strain rate sensitivity of an electrodeposited 20 nm grain sized Ni,” *J. Phys. D: Appl. Phys. J. Phys. D: Appl. Phys*, vol. 40, no. 40, pp. 7440–7446, 2007.

Appendix A

From the definition of indentation stress:

$$\sigma_{ind} = \frac{P}{A_{ind}} = \frac{P}{Ch^2} \quad (1)$$

where C is constant, so

$$P = \sigma_{ind}h^2 \quad (2)$$

$$\frac{\partial P}{\partial h} = 2h\sigma_{ind} \quad (3)$$

Besides,

$$\dot{P} = \frac{\partial P}{\partial t} = \frac{\partial P}{\partial h} \frac{\partial h}{\partial t} = \frac{\partial P}{\partial h} \dot{h} \quad (4)$$

By substituting (3) into (4)

$$\dot{P} = 2h\dot{h}\sigma_{ind} \quad (5)$$

By substituting (1) into (5)

$$\dot{P} = 2\frac{P}{h}\dot{h} \quad (6)$$

So

$$\frac{\dot{P}}{P} = 2\frac{\dot{h}}{h} = 2\dot{\epsilon} \quad (7)$$

Then

$$\dot{\epsilon} = \frac{1}{2}\frac{\dot{P}}{P} \quad (8)$$

Appendix B

The shear strain rate, $\dot{\gamma}$, can be given by an Arrhenius-type equation as

$$\dot{\gamma} = \dot{\gamma}_0 \exp\left(-\frac{\Delta G(\tau)}{kT}\right) \quad (1)$$

where the pre-exponential factor $\dot{\gamma}_0$ includes the number of possible activation sites, the average shear strain per successful thermal fluctuation, and the frequency of the vibration of the elemental unit involved in the thermal activation. ΔG is the activation energy and is usually a strong function of the shear stress component τ .

From equation (1), we can get

$$V^* = kT \left(\frac{\partial \ln \dot{\gamma}}{\partial \tau} \right) \quad (2)$$

Equation (4) can be re-written as

$$V^* = \frac{kT}{\tau} \frac{\partial \ln \dot{\gamma}}{\partial \ln \tau} \quad (3)$$

The strain rate sensitivity can be defined as

$$m = \frac{\partial \ln \tau}{\partial \ln \dot{\gamma}} \quad (4)$$

So

$$V^* = \frac{kT}{\tau m} \quad (5)$$

Here we see the relationship between the m and the V^* of plastic deformation.

According to the von Mises yield theory, the yield shear stress is $\tau = \sigma_y / \sqrt{3}$ (σ_y is the uniaxial yield stress).

So

$$m = \frac{\sqrt{3}kT}{\sigma_y V^*} \quad (6)$$

Since the indentation hardness H is directly proportional to the equivalent yield stress, often referred to as the equivalent flow stress, of a metal as

$$H \approx 3\sigma_y \quad (7)$$

So

$$m = \frac{3\sqrt{3}kT}{H V^*} \quad (8)$$

Curriculum Vitae

Name: Feifei Nie

Post-secondary Education and Degrees: University of Science and Technology Beijing, Beijing, China
2010-2014 B.A.

The University of Western Ontario
London, Ontario, Canada
2015-2017 M.A.

Honours and Awards: Western Graduate Research Scholarship (WGRS)
2015-2016

Related Work Experience Research Assistant
The University of Western Ontario
2015-2016